BLOCK COPOLYMER DERIVED FUNCTIONAL NANOMATERIALS WITH THREE DIMENSIONAL POROUS STRUCTURES FOR PHOTONICS AND WATER APPLICATION

A Dissertation

Presented to the Faculty of the Graduate School

of Cornell University

In Partial Fulfillment of the Requirements for the Degree of

Doctor of Philosophy

by

Qi Zhang

May 2018

BLOCK COPOLYMER DERIVED FUNCTIONAL NANOMATERIALS WITH THREE DIMENSIONAL POROUS STRUCTURES FOR PHOTONICS AND WATER APPLICATION

Qi Zhang, Ph. D.

Cornell University, 2018

Block copolymer (BCP) self-assembly provides a convenient approach to access nanostructures at the tens of nanometer scale. Porous scaffolds from block copolymer self-assembled morphologies have a plethora of applications in areas including energy, filtration, and photonic devices. Selectively etching methods to remove one block are typically used to achieve porous structures derived from BCP equilibrium morphologies. BCP directed additive co-assembly, facilitated by thermal or solvent-vapor annealing processes and followed by BCP removal, is also routinely employed to achieve porous structures composed of non-BCP materials.

In the first part of this thesis, fabrication and characterization of three dimensional (3D) gyroidal mesoporous thin films are discussed made from BCP-resin/carbon composites. Spin-coated films made from triblock terpolymer plus pre-carbon precursors were subjected to solvent vapor annealing (SVA) to reach the desired gyroidal equilibrium morphology. In situ grazing incidence small angle x-ray scattering (GISAXS) was employed to elucidate structure evolution at different swelling stages during SVA and to identify appropriate conditions to quench films into the gyroid structure at room temperature. After crosslinking of carbon precursors and thermal decomposition of the BCP, a carbon scaffold with gyroid morphology was formed. Such 3D gyroidal thin films have multiple advantages over conventional templates. They have high

temperature resistance up to 900 °C under non-oxidizing conditions, which makes them compatible with deposition processes such as chemical vapor deposition. 3D pore size and hydrophilicity are tunable, facilitating the deposition of different types of materials into the nano-scale pores. Finally, a transfer technique for such gyroidal mesoporous thin films was developed to eliminate restrictions of film formation to specific substrates. These gyroidal carbon mesoporous thin film templates largely expand the materials selection pool for gyroidal structures.

BCPs not only provide 3D scaffolds from equilibrium morphologies, but also can form 3D hierarchical superstructures with graded meso- to macro-scale pores from non-equilibrium processes. Resulting membranes have uniform surface mesopores supported by a graded macroporous sublayer. The process to generate such asymmetric ultrafiltration membranes is termed self-assembly plus non-solvent induced phase separation, or simply SNIPS. SNIPS membrane performance is largely controlled by details of the meso- and macro-porous structures. In the second part of this thesis, BCP derived SNIPS membrane ultrafiltration performance with respect to flux and solute diffusion rates is studied in relation to surface mesoporous and sublayer macroporous structures. These structures are systematically tuned identifying several key factors in the membrane casting process. To explore SNIPS membrane pore surface functionality, a new BCP membranes was designed and synthesized with thiol functional groups exposed on pore walls and membrane surfaces. A series of experiments were conducted to illustrate the accessibility of these functional groups after membrane fabrication. Conjugation reactions between maleimide functionalized dye and thiol membrane demonstrated that the thiol functional groups were active as covalent binding sites when simply soaking the membranes into target molecule solutions. We expect these functional membranes to enable biosensing and multi-level responsive smart materials applications.

BIOGRAPHICAL SKETCH

Qi was born in Xi'an, China in 1991. Inspired by her parents, who are both engineers, Qi showed great enthusiasm in science and technology at her early ages. She was admitted to Tsinghua University in 2009, initially pursuing a bachelor degree in Biology. A very multidisciplinary environment within the university allowed her to explore more possibilities regarding the field she wanted to dig deeper into. After several constructive conversations with the professor who was in charge of her class, Dr. Yigong Shi, she decided to switch to Materials Science and Engineering at her second year of college.

Qi really appreciated the various opportunities presented to her during college, academically and recreationally. She enjoyed the time and efforts spent together with her classmates for studying, preparing dancing shows, and all the outing events. She also participated in an exchange program in Toronto University for one semester, which was a great opportunity for her to learn and experience a very different culture.

Last year of college, Qi spent most of time in the Advanced Ceramic Laboratory, under the guidance of Dr. Changan Wang, where she felt the excitement of unveiling and developing new materials. After several insightful discussions with Dr. Rong Yu, who was in charge of her class, Qi finally made her mind that she would like to pursue graduate study.

In 2013 Fall, Qi joined Wiesner group in Cornell University, Department of Materials Science and Engineering. Her doctoral research was on nanostructured membrane materials and thin film systems for water and potential photonic applications, along with several collaborations with other company and institutes. This thesis summarizes the major focuses of her work in Wiesner lab.

Dedicated to my parents and friends for their unceasing love and support.

ACKNOLEDGEMENTS

This work benefits from many people's help, discussions, and collaborations. First and foremost, I would like to thank my advisor, Professor Uli Wiesner for his guidance and influence of not only research, but also his diligent working attitude, sincere enthusiasm and visions of progresses in scientific field. I also really appreciate the freedom he gave me to explore, it helped me grow into a confident, independent researcher. I would also like to thank my committee members Prof. Michael O. Thompson, and Prof. Christopher. K. Ober, for their helpful discussions and very constructive inputs into this work, and also for allowing me to use the equipment and the lab which made this work possible.

I greatly appreciate all members of the Wiesner group for their insights and helpful advice in the lab, as well as all the funs we had. In particular I would like to thank Dr. Yibei Gu for her guidance when I first joined the group, I benefit a lot from the lab techniques and work methodology which I learned from her. I also would like to thank Dr. Kwan Wee Tan, Dr. Jörg G. Werner and Dr. Hiroaki Sai for teaching me various synthesis and characterization skills. A special thanks to soon-to-be Dr. Yuk Mun Li and Dr. Teresa Kao, for all the smooth collaborations, and most importantly the friendships and all the laughter in the small office during these four years. I have been fortunate to guide graduate student Fei Yu, and mentor my undergraduate Samuel Closter, I wish both of you a bright future.

I would also like to acknowledge all my collaborators. Special thanks to Jennifer Poole, Jeremy Walker and the FLIR team for presenting the smart responsive suit project to us and coordinating all the collaborations and conferences over the four years. Thank you Dr. Detlef Smilgies, for getting me started from zero on the beamline and all the helpful inputs in the GISAXS work. A big thank you to Prof. Paul Nealey, and his graduate student Moshe Dolejsi and Chun Zhou for

the opportunity to visit their lab at University of Chicago and learn solvent vapor annealing. Thank you Dima Bolmatov, for the opportunity to visit BNL, learn inelastic scattering, and the fun at beautiful Long Island. I also like to thank Peter Beaucage, Ethan Susca, David Lynch, Hyo Seon Suh, Alex Chaney for the excellent collaborations.

I am thankful to Phil Carubia, Don Werner, Phil Infante, Anthony Condo, Tom Pennell, Christopher Alpha, Tom Derrien, and Mark Pfeifer for their training and helpful advice on instruments and characterizations.

Last but not the least, my deepest gratitude to my parents, Lihong Huang and Yimin Zhang, for their unconditional love throughout my whole life. And a big thanks to Dr. Tongchuan Gao, for all his support, advice and laughter throughout this journey. A special thanks to Netease Music, Spotify, my books and kindle for brining countless great music and novels that make me enjoy my life.

TABLE OF CONTENTS

BIOGRAPHICAL SKETCH v
ACKNOLEDGEMENTS vii
CHAPTER 1 1
INTRODUCTION 1
REFERENCES 8
CHAPTER 2 11
PATHWAYS TO MESOPOROUS RESIN/CARBON THIN FILMS WITH ALTERNATING GYROID MORPHOLOGY* 11
Abstract 11
Introduction 13
Results and discussion 15
Conclusion 35
Methods 36
Acknowledgments 41
REFERENCES 42
APPENDIX A 48
CHPATER 3 55
TUNING SUBSTRUCTURE AND PROPERTIES OF SUPPORTED ASYMMETRIC TRIBLOCK TERPOLYMER MEMBRANES* 55
Abstract 55
Introduction 56
Methods 58
Results and discussion 61
Conclusion 73
Acknowledgments 73
REFERENCES 75
APPENDIX B 78
CHAPTER 4 85
EFFECT OF HUMIDITY ON SURFACE STRUCTURE AND PERMEATION OF TRIBLOCK TERPOLYMER DRIVED SNIPS MEMBRANES* 85
Abstract 85

Introduction 87
Methods 89
Results and discussion 95
Conclusion 108
Acknowledgments 109
REFERENCES 111
APPENDIX C 115
CHAPTER 5 116
DYNAMICALLY RESPONSIVE MULTIFUNCTIONAL ASYMMETRIC TRIBLOCK TERPOLYMER MEMBRANES WITH INTRINSIC BINDING SITES FOR COVALENT MOLECULE ATTACHMENT* 116
Abstract 116
Introduction 117
Methods 119
Results and Discussion 122
Conclusions 134
REFERENCES 137
APPENDIX D 140
CHAPTER 6 144
CONCLUSION 144
REFERENCES 144

CHAPTER 1

INTRODUCTION

In the past decade, the field of functional materials has seen growing interest in the design, synthesis and large-scale fabrication of nanomaterials with three dimensional (3D) co-continuous structures.[1–3] Such 3D architectures provide advantages over 2D or 1D materials such as high packing efficiency in planar structures, superior mechanical properties, and co-continuity-affected physical properties, which makes them favorable candidates for various applications including water filtration, sensing, energy conversion and storage, and optical/photonic crystal devices.[4–8]

Here focus will be on a particular type of 3D structures ordered periodically in all three dimensions. Their topological features enable interactions with e.g. light and stress, in a way that is governed by their 3D periodicity yielding functionalities that are unique to the structure.[9–11] Such materials whose properties are influenced by their structural design are termed as metamaterials. Functional photonics constitutes a large fraction of metamaterials. In a recent perspective by Braun[1], functional photonics is defined as "*structures or devices which enable energy transduction between photons and electrons, significantly narrow thermal emission, enhance photocatalysis, enable chemical sensing, or enable manipulation of light over small dimensions*". In order to achieve such functionalities, gaining precise control over photon-structure interactions is crucial. Therefore, 3D structures used for photonic devices normally require a high degree of perfection, long range periodicity, and low defect rates in terms of their topological features.

Another type of 3D materials is rather aperiodic yet has structural features on two or more length scales.[12] Such materials are classified as hierarchical, multi-scale structures. Hierarchical 3D structures usually benefit from features on multiple scales and provide superior collective functionalities in the bulk as compared to materials with structural features limited to a single length scale.[12] A great example of hierarchical materials is human bone, where features on all levels of hierarchy are believed to contribute to their exceptional mechanical properties.[13]

Various fabrication methods including direct laser writing, reactive ion etching, hydrothermal synthesis and colloidal/block copolymer self-assembly have been developed to access periodic and hierarchical structures, based on factors such as material type and structural length scales.[14–20] Among these approaches, block copolymer (BCP) self-assembly provides a convenient platform for 3D nanostructure formation for both periodic as well as hierarchical types of structures as detailed in the following paragraphs.

Block copolymers are macromolecules with blocks polymerized from different monomers covalently jointed together. At equilibrium, BCPs arrange their chains spontaneously in minimum free energy configurations and produce ordered structures at the tens of nanometers scale, a process referred to as BCP self-assembly. By tuning block compositions, self-assembly varies over a large range of morphologies including several network structures like the “gyroid” or the “O70” structures in which each block periodically occupies 3D space.

In particular gyroid structures (Figure 1.1), used e.g. as model structures for metamaterials and photonic crystals, have been extensively studied due to their complex symmetries which endow them with unusual properties such as cloaking and negative refractive index.[9] Interest in these structures is documented by a growing number of simulation and experimental work.[21–24]

However, to a large extend the versatility in materials choice is still mostly limited to BCPs and materials directed or templated by BCPs.[25–28] Since BCPs are usually incompatible with approaches requiring high temperatures such as chemical vapor deposition (CVD), some materials of particular interest, including semiconductor materials like silicon, have been rarely explored experimentally with gyroid morphology of characteristic feature size below 100 nm.

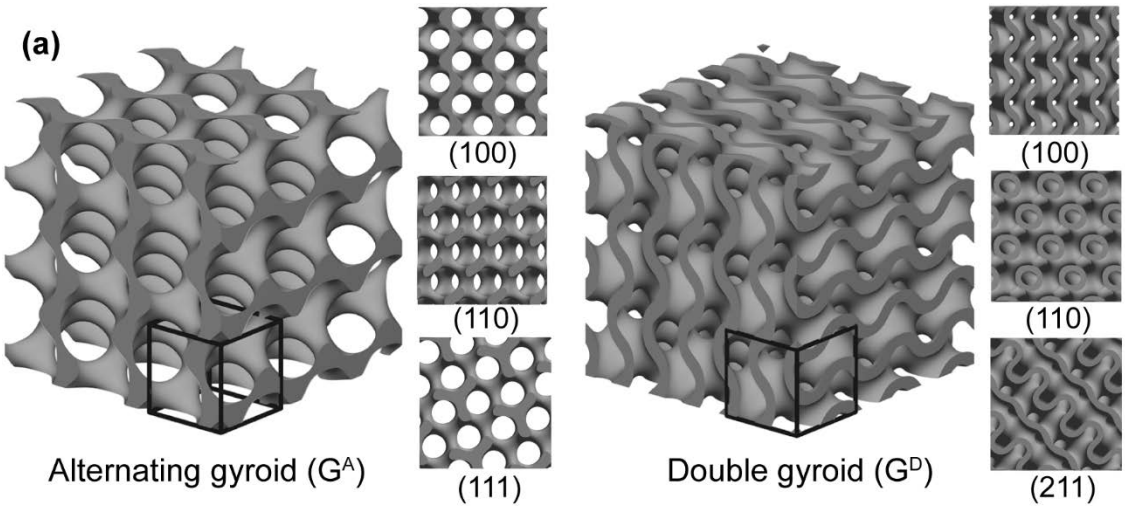

Figure 1.1 Illustration of alternating gyroid and double gyroid structures. Reproduced with permission.[29] Copyright 2017, American Chemical Society.

To expand the materials selection pool for gyroid structures, in Chapter 2 of this thesis resin/carbon based gyroid thin films are reported as potential templates. Single (alternating) gyroidal and double gyroidal mesoporous thin-film structures are achieved via solvent vapor annealing (SVA) assisted co-assembly of triblock terpolymer poly(isoprene-*block*-styrene-*block*-ethylene oxide) (PI-*b*-PS-*b*-PEO, ISO) and resorcinol/phenol formaldehyde resols. *In situ* grazing-incidence small-angle X-ray scattering (GISAXS) is used to elucidate and navigate

formation pathways during SVA. Resulting network structures are resistant to high temperatures and have tunable hydrophilicity and pore sizes, distinct advantages when functioning as 3D templates. Finally, a transfer technique of gyroid thin films between substrates is demonstrated circumventing the need to re-optimize film formation protocols for different substrates which are either not compatible with a desired template fabrication process (e.g. flexible polymeric substrates) or beneficial for further materials deposition. The reported method is also compatible for large scale fabrication.

Although BCP structures have been primarily studied by careful solvent/thermal treatment to achieve equilibrium phase behavior, hierarchical structures achieved by a combination of equilibrium and non-equilibrium approaches are also well documented in the literature.[30–32] Self-Assembly plus Nonsolvent Induced Phase Separation (SNIPS), a method pioneered by Peinemann *et al.*[33] and further developed by several research groups[34–36], yields a BCP membrane of graded porous structures ranging from nanometer to micrometer scales, presenting a great example for hierarchical structure formation generated by a simple fabrication method using BCPs. During SNIPS process, a polymer solution is first cast on a solid substrate with certain gate height. The solvent is then allowed to only partially evaporate for a time period which induces BCP self-assembly in the surface layer of casted solution and generates a solvent gradient along the film normal. Finally, the casted film is plunged into a coagulation bath precipitating out the final membrane and converting the solvent gradient into a pore size gradient. Resulting BCP membranes usually have a well-ordered, isoporous skin layer on the surface with graded pore substructure underneath (Figure 1.2). Such graded pore structures are ideal as ultrafiltration (UF) membranes due to their high selectivity from narrow pore size distributions in the skin layer and high flux from high pore densities.

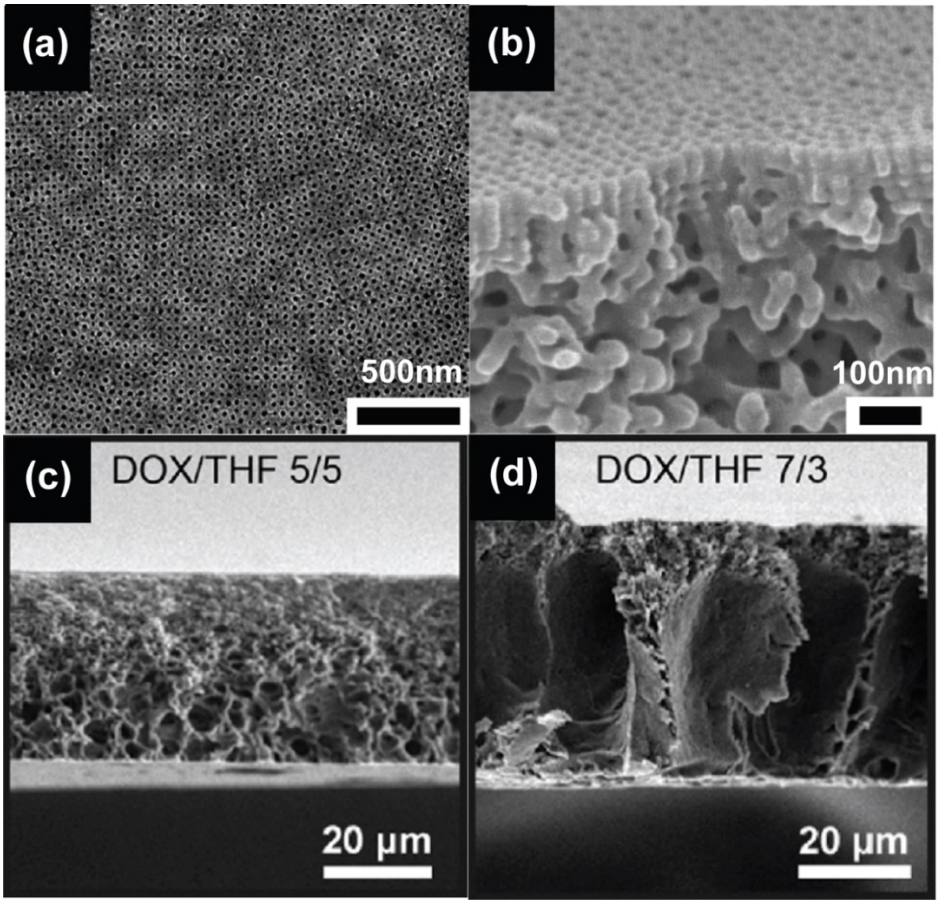

Figure 1.2 SEM images of SNIPS membrane. (a) Top surface SEM shows high density, uniform nanopores packed in a square lattice. (b) Cross sectional SEM micrograph shows open pores spanning the top separation layer. Cross sectional SEM of whole membranes show asymmetric, microporous sublayer with (c) spongelike and (d) fingerlike morphologies. Reproduced with permission.[34,37] Copyright 2014 American Chemical Society, 2016 Elsevier.

To date, SNIPS membranes based on polystyrene-*b*-poly(4-vinyl pyridine) (SV) diblock copolymers and polyisoprene-*b*-polystyrene-*b*-poly(4-vinyl pyridine) ISV triblock terpolymers, have been extensively studied and optimized with regard to their surface formation mechanisms and skin layer tunability.[38–40] In contrast, their graded substructure formation and associated performance variations are less well understood. Chapter 3 therefore describes processing

dependent SNIPS membrane substructure formation using triblock terpolymer ISV. Membrane casting parameters are systematically varied to tune the cross-sectional morphologies while simultaneously preserving top surface isoporous structure. Controlled transformations between sponge-like cross-sectional morphologies and more open and permeable fingerlike substructures are obtained and result in distinct differences in hydraulic permeability. This work provides a guideline to adjust membrane performance by affecting their substructure, and demonstrates SNIPS membranes with tunable flux but unaffected selectivity.

To further enhance control over SNIPS membrane structure and explore structure-performance correlations for ultrafiltration applications, in Chapter 4 relative humidity (RH) is investigated as a casting condition that impacts ISV membrane surface structure in terms of order and uniformity. Membranes cast at an optimized RH of 40-45% are characterized by a high density of square packed pores with narrow pore size distribution, while lower or higher RH results in deterioration of membrane pore order and uniformity. For quantitative description of membrane surface pore order and uniformity, a model solute, methyl orange with molar mass of 327 g/mol, is used to challenge the membranes and the diffusivity rate is correlated with surface structure control. Membranes cast at 40% RH reveal higher diffusivity than when cast at 75% RH consistent with better surface pore uniformity at 40% RH. The rate of permeation is further controlled via pH dependent pore closure as well as through ISV terpolymer molecular architecture (i.e. molar mass) and results are rationalized via applications of theoretical models.

Finally, besides structural investigations, variation in pore surface block chemistry is explored to extend SNIPS membrane' functionality. To that end, Chapter 5 reports the synthesis of a new triblock terpolymer poly(styrene)-*block*-poly(4-vinylpyridine)-*block*-poly(propylene sulfide) (SVPS), where sulfhydryl functional groups are introduced via a short poly(propylene

sulfide) (PPS) end block. These functional groups serve as covalent binding sites via thiol-ene click chemistry for facile attachment of foreign functional molecules after fabrication of isoporous ultrafiltration membranes using the SNIPS. The use of analytic redox reactions and quantification experiments prove that the functional groups are accessible and exposed on the membrane pore walls. A conjugation reaction with a maleimide functionalized dye is used as an example for a facile post-membrane fabrication functionalization reaction. At the same time this membrane exhibits pore closure in response to pH changes due to the presence of P4VP block on the pore wall surface, demonstrating the potential as a chemical gate as well as multifunctionality. As the concepts of pore-block end-functionalized membranes is not limited to sulfhydryl groups but can be extended to other functional groups such as amines and carboxylic groups, the choice of incorporated receptors/target molecules is expected to expand rapidly. Together with the forgoing examples this study establishes block copolymer derived SNIPS membranes as a powerful new materials platform with tremendous scientific as well as technological promise in areas ranging from biopharmaceutical separations, virus filtrations, catalysis and drug delivery.

REFERENCES

1. Braun, P. V. Materials Chemistry in 3D Templates for Functional Photonics. *Chem. Mater.* **26,** 277–286 (2014).

2. Shehzad, K., Xu, Y., Gao, C. & Duan, X. Three-dimensional macro-structures of two-dimensional nanomaterials. *Chem. Soc. Rev.* **45,** 5541–5588 (2016).

3. Hattori, A. N., Fujiwara, Y., Fujiwara, K. & Tanaka, H. 3D-Architected and Integrated Metal Oxide Nanostructures and Beyond Produced by Three-Dimensional Nanotemplate Pulsed Laser Deposition. *e-J. Surf. Sci. Nanotech.* **13,** 279–283 (2015).

4. Lee, J.-H., Singer, J. P. & Thomas, E. L. Micro-/Nanostructured Mechanical Metamaterials. *Adv. Mater.* **24,** 4782–4810 (2012).

5. Salvatore, S. *et al.* Tunable 3D Extended Self-Assembled Gold Metamaterials with Enhanced Light Transmission. *Adv. Mater.* **25,** 2713–2716 (2013).

6. Dolan, J. A. *et al.* Optical Properties of Gyroid Structured Materials: From Photonic Crystals to Metamaterials. *Advanced Optical Materials* **3,** 12–32 (2015).

7. Werner, J. G., Johnson, S. S., Vijay, V. & Wiesner, U. Carbon–Sulfur Composites from Cylindrical and Gyroidal Mesoporous Carbons with Tunable Properties in Lithium–Sulfur Batteries. *Chem. Mater.* **27,** 3349–3357 (2015).

8. Cowman, C. D. *et al.* Multicomponent Nanomaterials with Complex Networked Architectures from Orthogonal Degradation and Binary Metal Backfilling in ABC Triblock Terpolymers. *J. Am. Chem. Soc.* **137,** 6026–6033 (2015).

9. Hur, K. *et al.* Three-Dimensionally Isotropic Negative Refractive Index Materials from Block Copolymer Self-Assembled Chiral Gyroid Networks. *Angew. Chem. Int. Ed.* **50,** 11985–11989 (2011).

10. Bauer, J., Schroer, A., Schwaiger, R. & Kraft, O. Approaching theoretical strength in glassy carbon nanolattices. *Nature Materials* **15,** 438 (2016).

11. Valev, V. K., Baumberg, J. J., Sibilia, C. & Verbiest, T. Chirality and Chiroptical Effects in Plasmonic Nanostructures: Fundamentals, Recent Progress, and Outlook. *Advanced Materials* **25,** 2517–2534 (2013).

12. Wang, D.-W., Li, F., Liu, M., Lu, G. Q. & Cheng, H.-M. 3D Aperiodic Hierarchical Porous Graphitic Carbon Material for High-Rate Electrochemical Capacitive Energy Storage. *Angewandte Chemie International Edition* **47,** 373–376 (2008).

13. Fratzl, P. & Weinkamer, R. Nature's hierarchical materials. *Progress in Materials Science* **52,** 1263–1334 (2007).

14. Selimis, A., Mironov, V. & Farsari, M. Direct laser writing: Principles and materials for scaffold 3D printing. *Microelectronic Engineering* **132,** 83–89 (2015).

15. Miyake, M., Chen, Y.-C., Braun, P. V. & Wiltzius, P. Fabrication of Three-Dimensional Photonic Crystals Using Multibeam Interference Lithography and Electrodeposition. *Adv. Mater.* **21,** 3012–3015 (2009).

16. Kim, G., Son, J., Park, S. & Kim, W. Hybrid Process for Fabricating 3D Hierarchical Scaffolds Combining Rapid Prototyping and Electrospinning. *Macromol. Rapid Commun.* **29,** 1577–1581 (2008).

17. van den Broek, J. M. *et al.* Inverse-Woodpile Photonic Band Gap Crystals with a Cubic Diamond-like Structure Made from Single-Crystalline Silicon. *Adv. Funct. Mater.* **22,** 25–31 (2012).

18. Synthesis of 3D Hierarchical Fe3O4/Graphene Composites with High Lithium Storage Capacity and for Controlled Drug Delivery - The Journal of Physical Chemistry C (ACS Publications). Available at: http://pubs.acs.org/doi/abs/10.1021/jp204502n. (Accessed: 1st January 2018)

19. Shimmin, R. G., Vajtai, R., Siegel, R. W. & Braun, P. V. Room-Temperature Assembly of Germanium Photonic Crystals through Colloidal Crystal Templating. *Chem. Mater.* **19,** 2102–2107 (2007).

20. Werner, J. G., Hoheisel, T. N. & Wiesner, U. Synthesis and Characterization of Gyroidal Mesoporous Carbons and Carbon Monoliths with Tunable Ultralarge Pore Size. *ACS Nano* **8,** 731–743 (2014).

21. Dehmel, R. *et al.* Optical Imaging of Large Gyroid Grains in Block Copolymer Templates by Confined Crystallization. *Macromolecules* **50,** 6255–6262 (2017).

22. Jung, G. S., Yeo, J., Tian, Z., Qin, Z. & Buehler, M. J. Unusually low and density-insensitive thermal conductivity of three-dimensional gyroid graphene. *Nanoscale* **9,** 13477–13484 (2017).

23. Wilts, B. D. *et al.* Butterfly gyroid nanostructures as a time-frozen glimpse of intracellular membrane development. *Science Advances* **3,** e1603119 (2017).

24. Peng, S. *et al.* Three-Dimensional Single Gyroid Photonic Crystals with a Mid-Infrared Bandgap. *ACS Photonics* **3,** 1131–1137 (2016).

25. Susca, E. M. *et al.* Self-Assembled Gyroidal Mesoporous Polymer-Derived High Temperature Ceramic Monoliths. *Chem. Mater.* **28,** 2131–2137 (2016).

26. Robbins, S. W. *et al.* Block copolymer self-assembly–directed synthesis of mesoporous gyroidal superconductors. *Science Advances* **2,** e1501119 (2016).

27. Crossland, E. J. W. *et al.* A Bicontinuous Double Gyroid Hybrid Solar Cell. *Nano Lett.* **9,** 2807–2812 (2009).

28. Kim, E. *et al.* Gyroid-Structured 3D ZnO Networks Made by Atomic Layer Deposition. *Adv. Funct. Mater.* **24,** 863–872 (2014).

29. Zhang, Q. *et al.* Pathways to Mesoporous Resin/Carbon Thin Films with Alternating Gyroid Morphology. *ACS Nano* (2017). doi:10.1021/acsnano.7b06436

30. Dorin, R. M., Sai, H. & Wiesner, U. Hierarchically Porous Materials from Block Copolymers. *Chem. Mater.* **26,** 339–347 (2014).

31. Sai, H. *et al.* Hierarchical Porous Polymer Scaffolds from Block Copolymers. *Science* **341,** 530–534 (2013).

32. Yu, H. *et al.* Asymmetric block copolymer membranes with ultrahigh porosity and hierarchical pore structure by plain solvent evaporation. *Chem. Commun.* **52,** 12064–12067 (2016).

33. Peinemann, K.-V., Abetz, V. & Simon, P. F. W. Asymmetric superstructure formed in a block copolymer via phase separation. *Nature Materials* **6,** 992 (2007).

34. Phillip, W. A. *et al.* Tuning Structure and Properties of Graded Triblock Terpolymer-Based Mesoporous and Hybrid Films. *Nano Lett.* **11,** 2892–2900 (2011).

35. Dorin, R. M. *et al.* Solution Small-Angle X-ray Scattering as a Screening and Predictive Tool in the Fabrication of Asymmetric Block Copolymer Membranes. *ACS Macro Lett.* **1,** 614–617 (2012).

36. Sankhala, K., Koll, J., Radjabian, M., Handge, U. A. & Abetz, V. A Pathway to Fabricate Hollow Fiber Membranes with Isoporous Inner Surface. *Adv. Mater. Interfaces* **4,** n/a-n/a (2017).

37. Zhang, Q., Li, Y. M., Gu, Y., Dorin, R. M. & Wiesner, U. Tuning substructure and properties of supported asymmetric triblock terpolymer membranes. *Polymer* **107,** 398–405 (2016).

38. Gu, Y., Dorin, R. M., Tan, K. W., Smilgies, D.-M. & Wiesner, U. In Situ Study of Evaporation-Induced Surface Structure Evolution in Asymmetric Triblock Terpolymer Membranes. *Macromolecules* **49,** 4195–4201 (2016).

39. Rangou, S. *et al.* Self-organized isoporous membranes with tailored pore sizes. *Journal of Membrane Science* **451,** 266–275 (2014).

40. Sutisna, B. *et al.* Design of block copolymer membranes using segregation strength trend lines. *Molecular Systems Design & Engineering* **1,** 278–289 (2016).

CHAPTER 2

PATHWAYS TO MESOPOROUS RESIN/CARBON THIN FILMS WITH ALTERNATING GYROID MORPHOLOGY*

Abstract

Three-dimensional (3D) mesoporous thin films with sub-100 nm periodic lattices are of increasing interest as templates for a number of nanotechnology applications, yet are hard to achieve with conventional top-down fabrication methods. Block copolymer self-assembly derived mesoscale structures provide a toolbox for such 3D template formation. In this work, single (alternating) gyroidal and double gyroidal mesoporous thin-film structures are achieved *via* solvent vapor annealing assisted co-assembly of poly(isoprene-*block*-styrene-*block*-ethylene oxide) (PI-*b*-PS-*b*-PEO, ISO) and resorcinol/phenol formaldehyde resols. In particular, the alternating gyroid thin-film morphology is highly desirable for potential template backfilling processes as a result of the large pore volume fraction. *In situ* grazing-incidence small-angle X-ray scattering during solvent annealing is employed as a tool to elucidate and navigate the pathway complexity of the structure formation processes. The resulting network structures are resistant to high temperatures provided an inert atmosphere. The thin films have tunable hydrophilicity from pyrolysis at different temperatures, while pore sizes can be tailored by varying ISO molar mass. A transfer technique between substrates is demonstrated for alternating gyroidal mesoporous thin films, circumventing the need to re-optimize film formation protocols for different substrates. Increased conductivity after pyrolysis at high temperatures demonstrates that these gyroidal mesoporous resin/carbon thin films have potential as functional 3D templates for a number of nanomaterials applications.

[*] Reprinted (adapted) with permission from Q. Zhang, F. Matsuoka, H. S. Suh, P. A. Beaucage, S. Xiong, D. M. Smilgies, K. W. Tan, J. G. Werner, P. F. Nealey, U. Wiesner, Pathways to Mesoporous Resin/Carbon Thin Films with Alternating Gyroid Morphology, ACS Nano DOI: 10.1021/acsnano.7b06436. Copyright 2017 American Chemistry Society.

Introduction

Materials with three-dimensional (3D) network structures have demonstrated potential for energy,[1,2,3] photonics[4,5] and mechanics[6,7] related applications. The 3D periodic topological features on nano- and micro-meter scales endow materials with properties such as negative refractive index[5,8-10] and high strength-to-density ratio.[6] However, direct fabrication of 3D nanostructures made of inorganic materials may be challenging due to limitations in finding suitable direct synthesis methods. Therefore, 3D porous templates are often employed.[4]

Colloidal crystal self-assembly is one of the most popular 3D templating approaches typically generating an inverse opal (IO) structure with face-centered cubic (FCC) symmetry.[11-13] The templates are often made of either polymeric or silica spheres. Various direct laser writing methods are also strong candidates for 3D structure/template fabrication, and offer more flexibility in terms of accessible morphologies.[14,15] Both of these approaches have several drawbacks, however. First, direct laser writing methods render periodic lattices on length scales typically above 200 nm, while accessing length scales below 100 nm remains very challenging. The second limitation is the lack of versatility in materials choice. The majority of IO structures is derived from polymeric colloids. Similarly, direct laser writing methods as well as 3D printing approaches are often based on photopolymeric materials. Porous polymer templates are suitable for back-filling under mild processing conditions, including atomic layer deposition (ALD) and electrodeposition, but are usually incompatible with approaches requiring high temperatures such as chemical vapor deposition (CVD).[16]

Block copolymer (BCP) self-assembly (SA) enables access to structures below 100 nm. Among the various mesoscale morphologies formed, 3D interconnected networks such as gyroidal structures are of particular interest (see models in Figure 2.1a). By etching or otherwise

removing one of the blocks, the resulting porous polymeric gyroidal templates can subsequently be back-filled with other materials.[17] For example, electro-[18-21] and electroless deposition[22,23] methods have widely been used to deposit metals into these mesoporous polymeric templates. However, incompatibilities exist between these materials and processes that require high temperatures, strong acids, or organic solvent environments. Such conditions imposed by back-filling processes largely narrow down the choice of materials that can be grown into the templates thereby limiting their possible applications. In order to overcome these limitations, resorcinol or phenol formaldehyde resols based carbon networks have been studied in bulk and in thin films.[24-30] To the best of our knowledge, however, mesoporous resin/carbon thin films with periodic single (alternating) gyroidal (Q^{214}) structure, which as a result of the large pore volume fraction are particularly interesting as 3D porous templates (*e.g.* compare Figure 2.1a and b), have not been reported to date. This may be due to the complexity of the associated structure formation pathways resulting from such multicomponent systems and factors (*e.g.* surface energy) predominant in thin films. Pathways may include order-order and/or order-disorder transitions, but have not been elucidated in such composite thin films to date. Moreover, in all of the previous examples self-assembly of gyroidal structures was optimized for specific substrates. It is well known, however, that BCP self-assembly in thin films is strongly influenced by substrate BCP interactions.[31] Results are therefore not transferable from one substrate to another requiring time-consuming re-optimization of film formation protocols between different substrates. A common approach to overcome such substrate restrictions involves film transfer techniques using a polymeric protective layer.[32-35] To the best of our knowledge, however, such transfer techniques have never been applied to the very open gyroidal porous structures, in particular with alternating gyroid structure.

Here we report both single (alternating) gyroid (Q^{214}) and double gyroid (Q^{230}) mesoporous thin film 3D structures from solvent vapor annealing (SVA) induced poly(isoprene-*block*-styrene-*block*-ethylene oxide) (PI-*b*-PS-*b*-PEO, ISO) triblock terpolymer directed self-assembly of resorcinol/phenol formaldehyde resols as evidenced by scanning electron microscopy (SEM) and grazing-incidence small-angle X-ray scattering (GISAXS). In particular, for resin/carbon thin films with desired large area single/alternating gyroid (Q^{214}) morphology, we show how *in situ* GISAXS can be employed to elucidate and navigate the pathway complexity of the associated structure formation processes during vapor annealing. With subsequent crosslinking and pyrolysis steps, either 3D gyroidal mesoporous resin-based (GMR; when heated to 450 °C) or carbon-based (GMC; when heated to 600 °C and above) thin films are obtained. Film pore size is tailored by using terpolymers with different molar mass. The pore surface hydrophilicity is tuned by pyrolysis temperature, an ability that may become crucial for backfilling of such intricate 3D structures with different materials. Increasing pyrolysis temperatures also leads to increasingly conducting functional carbon thin films. Finally, we demonstrate that these alternating gyroidal mesoporous thin films can be transferred to arbitrary flat substrates, removing the need for lengthy re-optimization of thin film structure formation protocols for every new substrate.

Results and discussion

$G^{A}MR$ and $G^{D}MR$ thin films

Three poly(isoprene-*block*-styrene-*block*-ethylene oxide) (PI-*b*-PS-*b*-PEO, ISO) triblock terpolymers were synthesized to serve as structure directing agents (Table 1). Resorcinol-/phenol-formaldehyde resols served as carbon precursors hydrogen bonded to PEO thereby selectively

swelling this block. By adjusting block copolymer (BCP) composition and resols loading amounts, two types of network structures with either single/alternating gyroid or double gyroid structure (space groups Q^{214} and Q^{230}, respectively) were achieved as detailed in Table 1. The composition selections for single and double gyroid structures were based on previous work on bulk ISO-resols composites, which in turn were based on a published ISO morphology map.[24,36] Models of these network structures are shown in Figure 2.1a for illustration purposes.

Table 2.1 ISO terpolymer compositions and resols loading details

Polymer	M_n **(kg/mol)**	f_{PI} **(vol%)**	f_{PS} **(vol%)**	f_{PEO} **(vol%)**	**PDI**	**PEO+resols (wt%)**	**Resols/ISO[a]**	**Resols type**
ISO77-G^AMR	77	30.6	60.8	8.6	1.04	25%	0.26	resorcinol-formaldehyde
ISO69-G^AMR	69	33.1	62.0	4.9	1.04	25%	0.32	resorcinol-formaldehyde
ISO28-G^DMR	28	10.5	34.1	55.4	1.11	76%	0.94	pheno-formaldehyde

a. Weight ratio

The different processing steps of gyroidal mesoporous resin (GMR) thin films with either alternating gyroid (G^AMR) or double gyroid (G^DMR) ordering are illustrated in Figure 2.1b. In step 1, a solution mixture of ISO BCP and resorcinol/phenol-formaldehyde resols was spin-coated onto a Si wafer piece resulting in a thin film with thickness of around 400 nm. In step 2, as-spun films were solvent annealed in THF vapor (Q^{214}) or chloroform vapor (Q^{230}) under various conditions (*vide infra*) until the desired structure was achieved. In step 3, the resulting BCP-resols hybrid thin films were brought to 115 °C to thermally crosslink the resols thereby further locking in the desired film structure. In step 4, a heat treatment at 450 °C under inert atmosphere further condensed the crosslinked resols into the final polymeric resin material while simultaneously decomposing the structure directing ISO terpolymer resulting in the desired G^AMR or G^DMR thin

films. In order to help identify films at different processing stages, BCP-resols hybrid thin films during or after solvent vapor annealing (SVA), but before the thermal crosslinking step, will be referred to as either BCP-resols hybrid or G^A/G^D-hybrid, respectively (see Figure 2.1b), depending on whether the structure has already been converted to a gyroid or not. In the case of the alternating gyroid morphology, structure evolution under SVA was studied and optimized utilizing a combination of *in situ* reflectometry and *in situ* GISAXS measurements of film thickness and structure, respectively. The resulting data are summarized in graphs as shown in Figure 2.1c where film thickness as a function of time is correlated to film structure. In general, THF vapor pressure was first raised to a high level to ensure a highly swollen film. The film was then deswollen by gradually decreasing solvent vapor pressure over a period of 60 minutes while in situ GISAXS measurements simultaneously captured structural details as a result of these changes, revealing both order-to-order as well as order-to-disorder transitions as described in detail in the subsequent section.

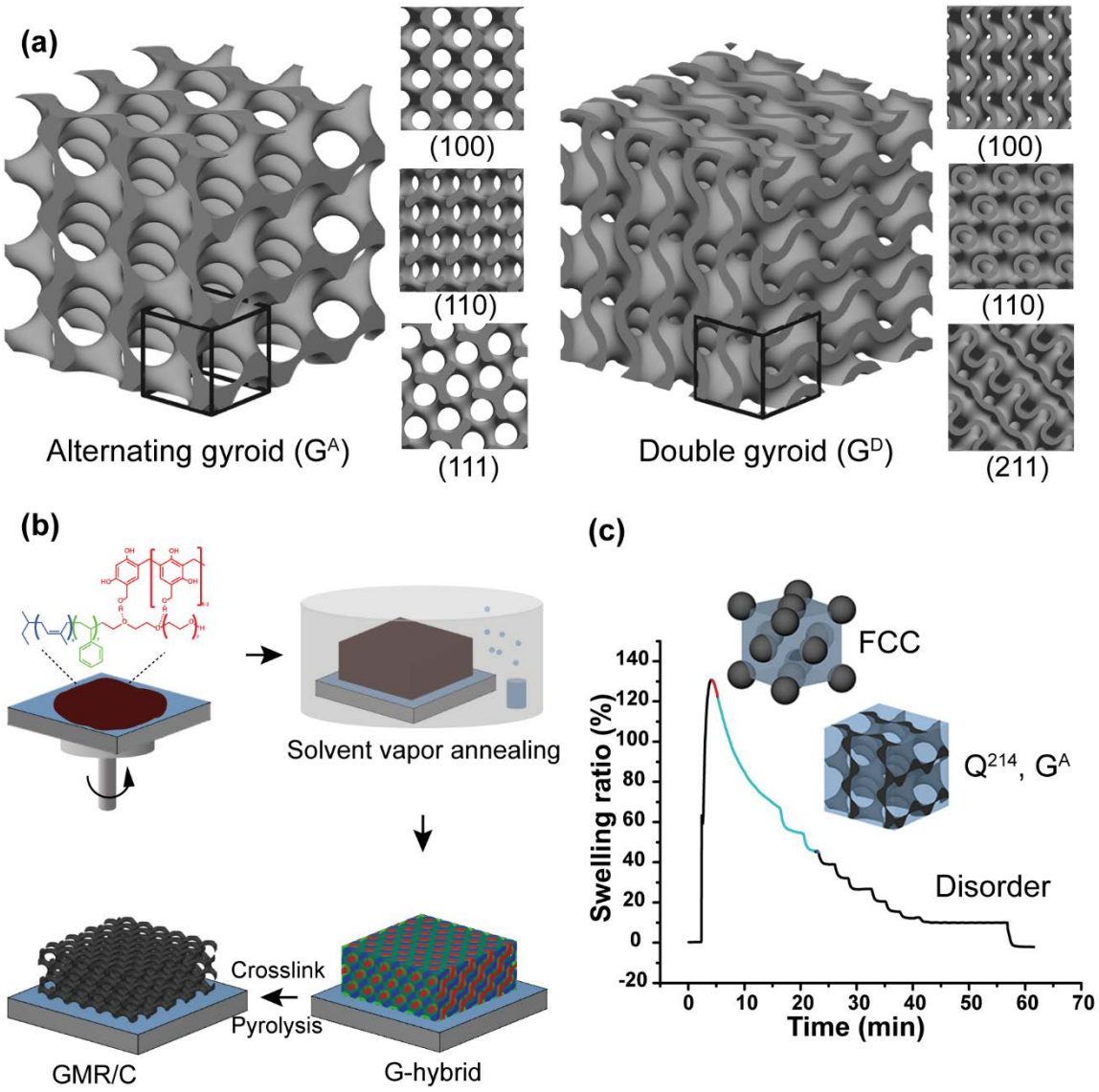

Figure 2.1 Illustrations of (a) G^A and G^D structures (unit cell in black) together with their respective characteristic surface patterns observed for specific crystal planes, (b) GMR/C thin film fabrication steps, and (c) structure evolution for BCP-resols hybrid thin films during solvent vapor annealing.

Scanning electron microscopy (SEM) images of the two types of final GMR thin film structures (G^AMR, G^DMR) are shown in Figure 2.2. Figure 2.2a-c depict the ISO77-G^AMR thin film top surface structure at two different magnifications (a,b) as well as a film cross-sectional structure (c). The highly ordered pattern observed in the top surface SEM in (a) clearly resembles

the (110) plane of the G^A model shown in Figure 2.1a (see Figure S2.3 for a more detailed analysis). A lower magnification top surface SEM image in Figure 2.2b reveals the film's grain structure demonstrating its polycrystalline nature. Within each grain, the surface orientation stays along the [110] direction. The cross-sectional image in Figure 2.2c confirms that the mesoporous structure is highly ordered in 3D. More cross-sectional images are shown in Figure S2.4. Interestingly, these cross-sectional images suggest that the pores are directly accessible at both substrate and air interfaces without the presence of dense capping layers.

Figure 2.2d-f shows similar SEM images for an ISO28-G^DMR thin film. The top surface SEM in Figure 2.2d shows the (211) plane with the characteristic double wavy pattern of the G^D morphology (compare with model shown in Figure 2.1a). A lower magnification SEM image in Figure 2.2e reveals several grains of the polycrystalline film morphology including a grain with (211) surface plane on the right and (110) surface plane on the upper left. The cross-sectional image in Figure 2.2f demonstrates that the bicontinuous double gyroid structure is maintained throughout the entire film thickness. Films with final G^D morphology were solvent annealed in a different setup from G^A films (see Methods section). Their final structure may be a collective result of both SVA and thermal crosslinking, as described in an earlier study.[28]

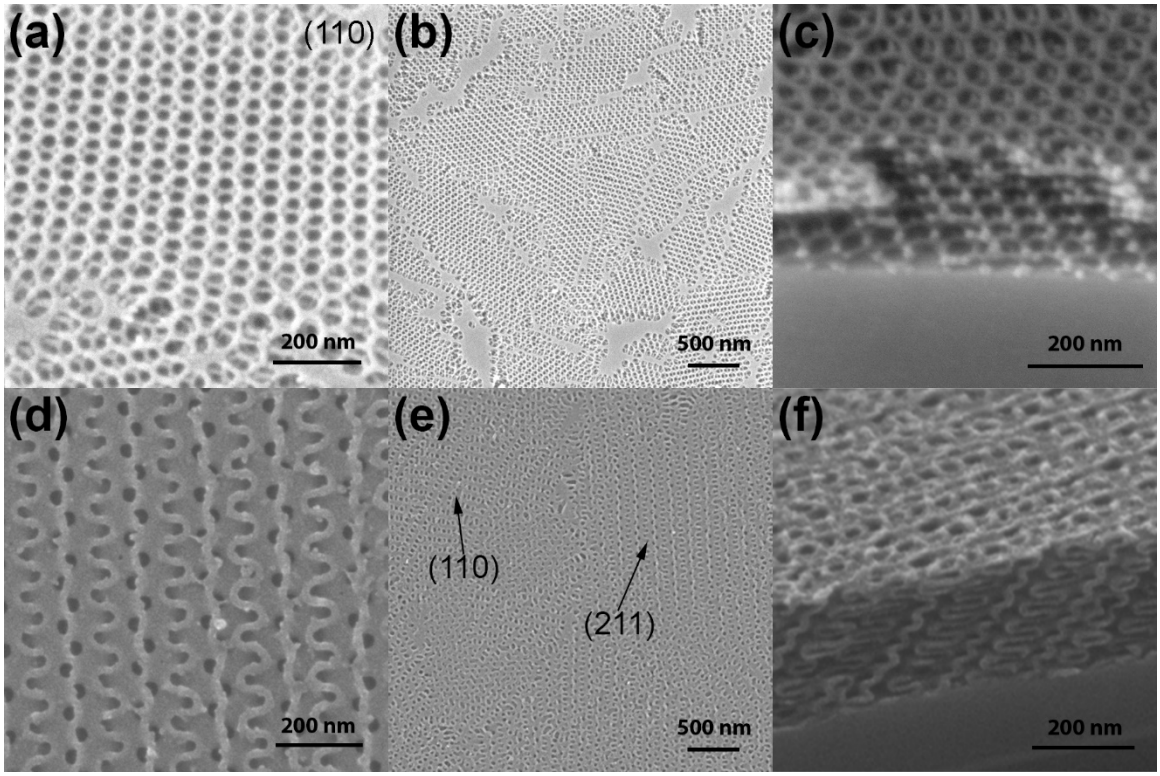

Figure 2.2 SEM characterization of GMR thin films with (a-c) alternating (ISO77-G^{A}MR) and (d-f) double gyroidal (ISO28-G^{D}MR) structures. Arrows in (e) indicate grains with specific orientations.

Grazing incidence small angle X-ray scattering (GISAXS) was employed to gain more insight into the structure of G^{A}MR thin films and possible deviations from ideal behavior. A 2D GISAXS pattern for a G^{A}MR thin film structure directed by ISO77 is shown in Figure 2.3. The diffraction pattern was analyzed using GIXSGUI, a Matlab-based tool for visualization, reduction and indexing of grazing incidence X-ray scattering data.[37] A previous study has shown that the alternating gyroid belongs to the space group #214 (Q^{214}) and has $I4_132$ symmetry.[38] Therefore, the basis coordinates were selected based on space group #214 during indexing. The film normal direction was chosen as [110] based on our SEM results (*vide supra*, Figure 2.1a, 2.2a, S2.3). Although space group #214 is cubic, shrinkage along the film normal [110] direction distorts the unit cell and therefore makes the lattice parameters a, b, c, α, β, γ deviate from the cubic lattice

rule (a=b=c, α=β=γ=90°). A unit cell of the G^A structure is drawn in Figure S2.5 to better illustrate the influence of shrinkage on the lattice parameters. After shrinkage along the [110] direction, the modified unit cell has a=b<c and α=β=90° while γ>90°. With these prerequisites and trial and error in indexing GISAXS diffraction patterns, a set of unit cell parameters, a = b = 51.6 nm, c = 71.0 nm, α = β = 90°, γ=151.4° rendered a very good match to the measured GISAXS pattern as shown in Figure 2.3. A shrinkage of 75% along the film normal [110] direction was estimated from this data analysis. Such large shrinkage has been observed before and is expected to be the result of a combination of solvent vapor annealing, thermal crosslinking, and pyrolysis.[18,39] GISAXS experiments were also conducted on an ISO69-G^AMR film with a GISAXS pattern shown in Figure S2.6. Using a similar indexing procedure as described above, a shrinkage of 77% was determined for this film. All GISAXS experiments corroborated structure and orientation assignments of G^AMR thin films by SEM. Since in comparison to the local scale of SEM the GISAXS X-ray beam footprint is on the millimeter scale, these results suggest that G^AMR nanostructures imaged by SEM were representative for the entire films.

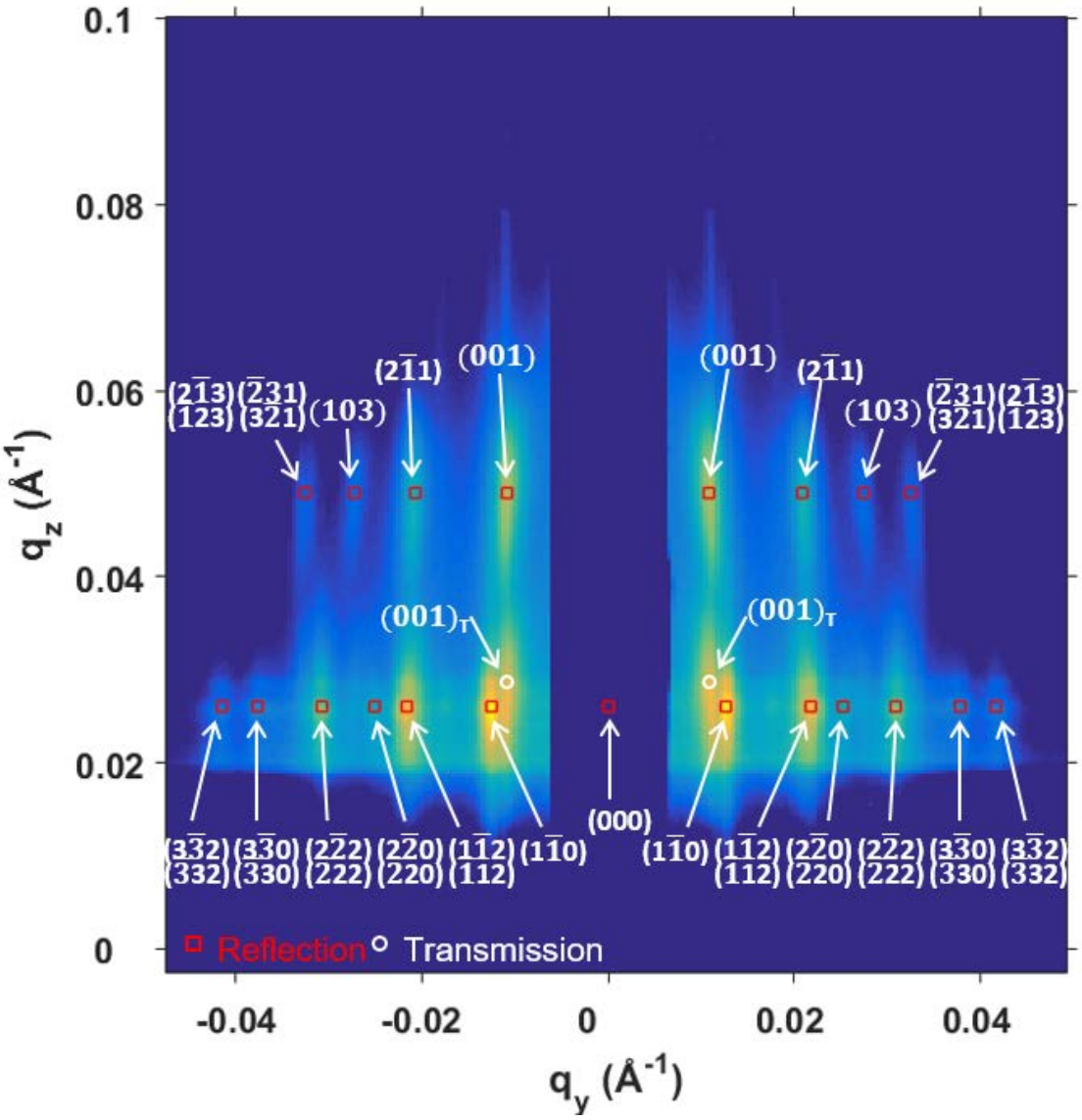

Figure 2.3 GISAXS pattern and associated indexing for sample ISO77-G^{A}MR. The incident angle for this data acquisition was 0.13°.

Pathway to thin films with G^A morphology *via* structure evolution during solvent vapor annealing

In comparison to the double gyroid structure (G^D, Q^{230}), which has been observed in both diblock copolymers and triblock terpolymers, the alternating gyroid (G^A, Q^{214}) structure is a network phase unique to triblock terpolymers. From Figures 1 and 2, G^{A}MR structures are expected to be more open as compared to G^{D}MR structures, which is advantageous as templating

scaffolds. Therefore, in this section we will focus on alternating gyroid thin film formation with particular emphasis on the structural evolution and associated pathway complexity SVA on the way to the final film structure.

In situ GISAXS is a powerful tool for understanding structure evolution of BCP thin films during solvent or thermal annealing, and consequently for optimizing annealing procedures.[40-45] *In situ* GISAXS studies of SVA process on as-spun thin films with ISO77-G^AMR composition was conducted in a flow chamber set up at beamline D1 at CHESS as described in the Methods section. A Filmetrics reflectometer was used to monitor film thickness, t, changes during SVA, allowing to monitor the swelling ratio ($SR=t/t_0-1$) as a function of time, see solid line in Figure 2.4a. The as-spun film didn't have any ordered structure due to the fast evaporation rate during spin-coating. The film quickly swelled to 130% SR, followed by slow deswelling to around 10% SR *via* reducing the solvent (THF) partial pressure by controlling the wet (THF in N_2 stream) and dry (pure N_2 stream) line mixing ratio into the flow chamber as described in the Methods section. Film structure at different swelling stages was monitored and recorded by *in situ* GISAXS. A representative scattering pattern at highest swelling ratio around 130% (red solid line section in Figure 2.4a) is shown in Figure 2.4b. The pattern could be indexed by a face centered cubic (FCC) lattice using indexGIXS software,[46-47] with unit cell parameters of $a = b = c = 69$ nm, $\alpha = \beta = \gamma = 90°$, and the (111) plane parallel to the substrate. A FCC structure at the highest film thickness, *i.e.* the highest solvent content, is consistent with micelle formation of a block copolymer in a selective solvent for at least one of the three blocks of the ISO terpolymer. In the region between 125% SR and 45% SR (blue solid line section in Figure 2.4a), data collected by *in situ* GISAXS evolved to a distinctly different pattern as represented in Figure 2.4c. This scattering pattern was successfully indexed by space group #214 (Q^{214}) using GIXSGUI software[37] with unit cell

parameters of a = b = c = 65 nm, $\alpha = \beta = \gamma = 90°$ and the (110) plane parallel to the substrate. When the film was further deswollen to below 45% SR, the structure started to fade as indicated by the GISAXS pattern shown in Figure 2.4d. Results from this *in situ* GISAXS study suggested that film structure during SVA strongly depended on the stage of swelling and ordered morphologies did not show any deviation from cubic symmetry (*vide supra*). Films had to be quenched from the swollen region with Q^{214} structure (*i.e.* 45%<SR<125%) in order to obtain a final film with alternating gyroid structure. The change in symmetry from the swollen cubic (Figure 2.4c) to the final structure (Figure 2.3) is most likely due to shrinkage during quenching and pyrolysis of the films. Both processes cause a volume decrease which can most easily be accommodated along the z-direction as these thin films are constrained in-plane by the substrate, resulting in a uni-axial shrinkage on the way to the final mesoporous film.

Following the insights provided by our *in situ* GISAXS studies, a reproducible SVA procedure leading to G^A thin film structure was developed using a simplified SVA chamber as detailed in the Methods section and illustrated in Figure S2.1, where film thickness was estimated by characteristic film color correlated to the earlier reflectometry results. For comparison, the corresponding approximate annealing pathway to thin films with G^A structure is plotted as a dashed line in Figure 2.4a. First, THF vapor flow to the annealing chamber was raised to a high level to ensure a fully swollen film. Then, film swelling ratio was decreased stepwise into the region with Q^{214} film structure, followed by a fast quench to freeze the alternating gyroid morphology. As suggested by earlier studies, a slow deswelling rate into the Q^{214} region may help with the structure formation process.[48] This SVA procedure was key to obtain thin films with G^AMR structure as presented in Figures 2a-c and 3.

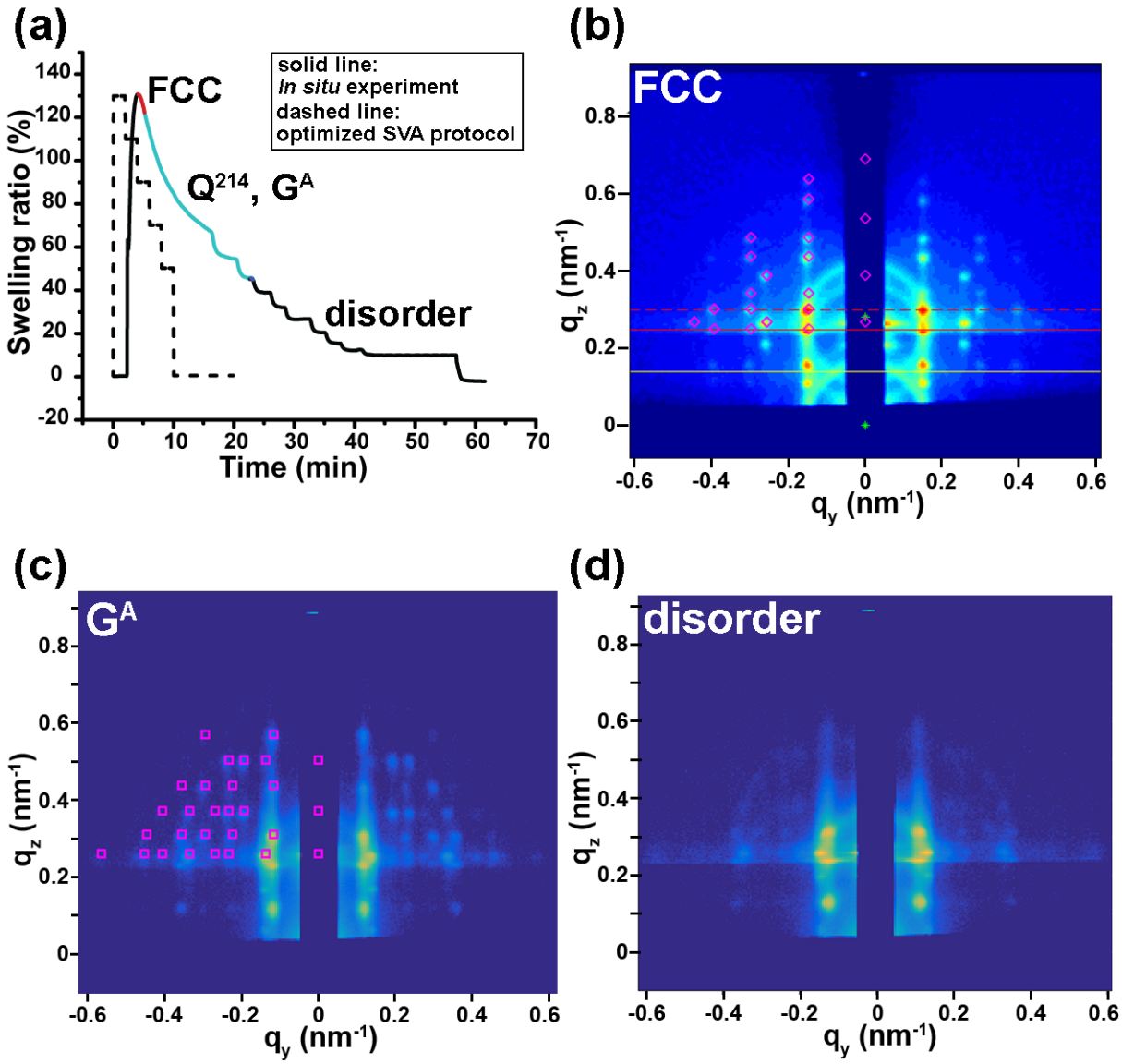

Figure 2.4 Results of *in situ* GISAXS studies of ISO-77 based BCP-resols hybrid thin films during solvent vapor annealing. (a) Film swelling ratio (SR) deduced from Filmetrics reflectometer data during solvent vapor annealing (solid line). Red, blue, and black sections correspond to films with FCC, G^A, and disordered thin film structure, respectively, as identified by *in situ* GISAXS. A reproducible pathway to thin films with G^A structure using a simplified SVA set up is approximated in (a) using a dashed line. Representative GISAXS scattering patterns at (b) SR = 130% with incident angle of 0.15°, indexed as FCC (magenta diamonds), (c) SR =

55% with incident angle of 0.14°, indexed as G^A (magenta squares), and (d) SR = 20% with incident angle of 0.14°, assigned to a film on its way to a disordered state.

Further characterization of G^AMR/C thin films

From GISAXS analysis final ISO69-G^AMR thin films had smaller unit cell parameters (a = b = 44.8 nm, c = 61.2 nm, α = β = 90°, γ=154.2°, Figure S2.6) as compared to ISO77-G^AMR films (a = b = 51.6 nm, c = 71.0 nm, α = β = 90°, γ=151.4°, Figure 2.3) due to the difference in ISO terpolymer molar mass. In order to further demonstrate the influence of macromolecular design in terms of molar mass on accessible pore sizes of G^AMR thin films, top surface SEM images of ISO77-G^AMR and ISO69-G^AMR thin films were analyzed using ImageJ. Detailed analysis steps are illustrated in Figure S2.7. Resulting surface pore size distributions are plotted in Figure 2.5. The observed increase in G^AMR thin film pore size moving from ISO69 to ISO77 demonstrates tunability through BCP molar mass. Uniaxial shrinkage has little influence on surface pore size distributions as shrinkage is along the film normal direction.

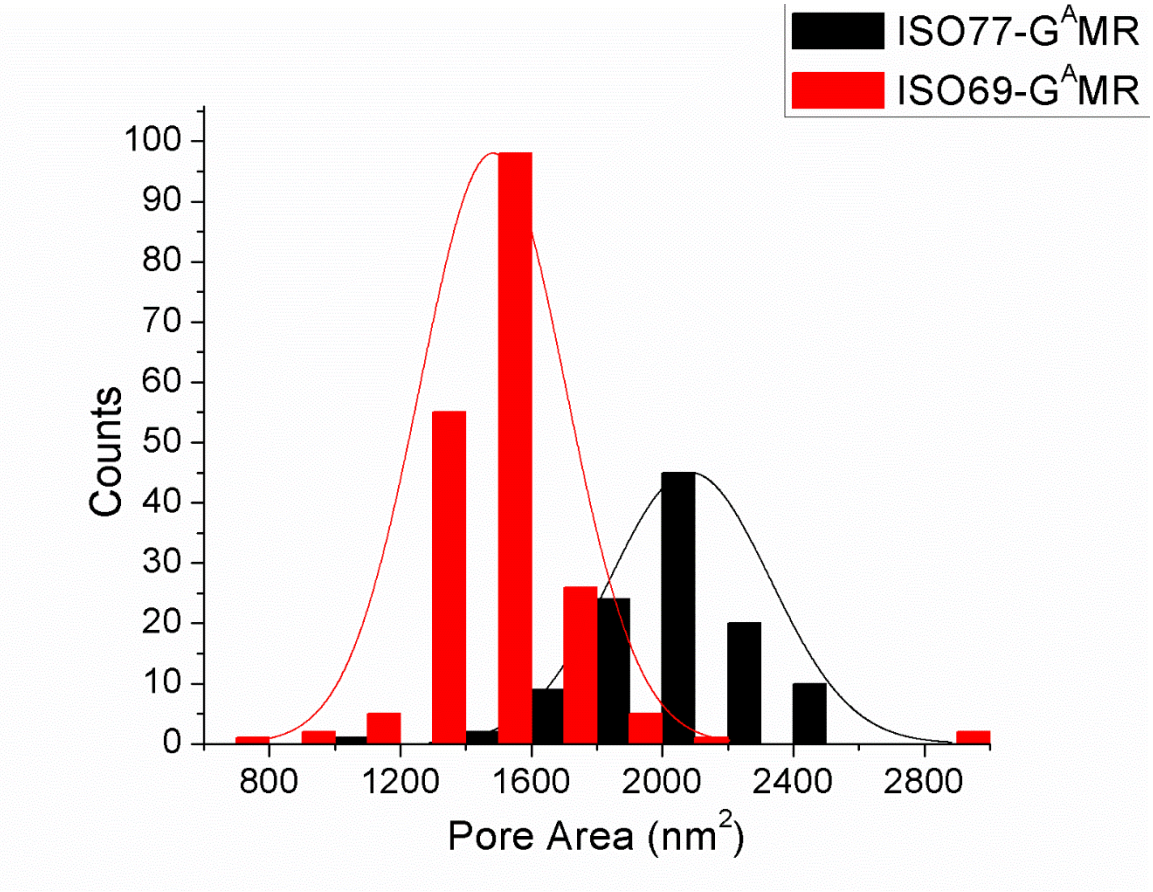

Figure 2.5 Pore size distribution analysis results of top surface SEM images for ISO69-G^{A}MR and ISO77-G^{A}MR thin films. Histograms were fitted by a normal Gaussian distribution with μ = 1461 nm^2 (mean) and σ = 144 nm^2 (standard deviation) for ISO69-G^{A}MR and μ = 2088 nm^2 and σ = 190 nm^2 for ISO77-G^{A}MR.

The advantage of GMR thin films in comparison to previously reported polymer templates is that such resin-based materials can endure harsh processing environments such as non-oxidizing strong acids or very high temperature treatments under inert atmosphere. Previous investigations of bulk films have demonstrated that the terpolymer ISO degrades at around 450 °C while resols simultaneously convert into highly crosslinked resin material.[24] Above 600 °C, the resin starts to carbonize, *i.e.* the GMR thin films are converted into gyroidal mesoporous carbon, GMC. To that end, we heat treated our G^A thin films under nitrogen or argon to 450 °C,

600 °C, and 900 °C, respectively, in a final pyrolysis step. The SEM images of the resulting films depicted in Figure 2.6a-c suggest that under these conditions the mesoporous gyroidal mesostructure is preserved.

When heated to high temperatures, the resin material undergoes carbonization resulting in electrical conductivity.[24,27,49] As a test, conductivity measurements were performed on mesoporous thin films with G^A structure heat treated to 450 ˚C and 900 ˚C, respectively. For films treated to 900 °C, linear voltage/current sweeps were observed resulting in a sheet resistance value of R_s=455 kΩ ± 144 kΩ, corresponding to a resistivity of 9.1 Ω·cm ± 2.9 Ω·cm for an approximated film thickness of 200 nm. In contrast, for films treated to 450 °C, over a voltage range of ± 100 V the current could not be determined within the instrument sensitivity of 1 nA, giving a lower bound for the sheet resistance of 453 GΩ, corresponding to a resistivity of 9.1 MΩ·cm for an approximated film thickness of 200 nm. The difference in resistivity by many orders of magnitude between films treated to 450 °C and 900 °C is consistent with expectations that higher pyrolysis temperatures result in thin film conductivity. Results also suggest connectivity of the mesoporous carbon thin film over macroscopic dimensions, with no observable major crack formation even under high-temperature conditions.

Since these GMR/C thin films show high temperature endurance and non-oxidative acid (*i.e.* hydrofluoric acid) resistance (*vide infra*), they are compatible with a number of deposition processes used in the semiconductor industry. As a result, they potentially can serve as 3D templates for nanoscale materials formation of various metals or semiconductors.[16,22,27] A problem commonly encountered during material deposition into templates with such complex 3D structure is that the deposited material cannot completely infiltrate the nanoscale template pores.

While the specific deposition method plays an important role, the difference in surface energy/hydrophilicity between template and deposited material is also crucial for successful backfilling. Since the resin material used here undergoes different degrees of carbonization and graphitization when treated at different temperatures, the associated material's chemistry changes are expected to induce changes in surface energy/hydrophilicity. We wanted to elucidate this behavior in more detail. To that end, contact angles were first measured on non-structured resin/carbon thin films in order to eliminate the influence of the porous structure. Flat, dense (non-structured) thin films were obtained by spin-coating pure resols solutions. The resulting flat thin films (thickness of ~200-400 nm) were then crosslinked, treated at 450 °C, 700 °C, 800 °C, and 1000 °C under inert atmosphere, respectively, and tested for water contact angles. Figure S2.8 shows SEM images of these dense resin thin films. As depicted in Figure 2.6d, contact angles substantially decreased as pyrolysis temperature increased, indicating that the resin/carbon materials became more hydrophilic as pyrolysis temperature increased. The same trend was observed for GMR/C thin films. Contact angle measurements were conducted on ISO69-G^{A}MR/C thin films heated to 450 °C, 600 °C and 900 °C, respectively. Figure 2.6e again shows decreasing contact angles with increasing pyrolysis temperature, demonstrating similar behavior as for the dense resin materials. The different heat treatment protocols (*i.e.* different temperatures) provide access to G^{A}MR/C thin films with tunable surface energy/hydrophilicity, which enables fine-tuning of surface characteristics to specific backfilling materials.

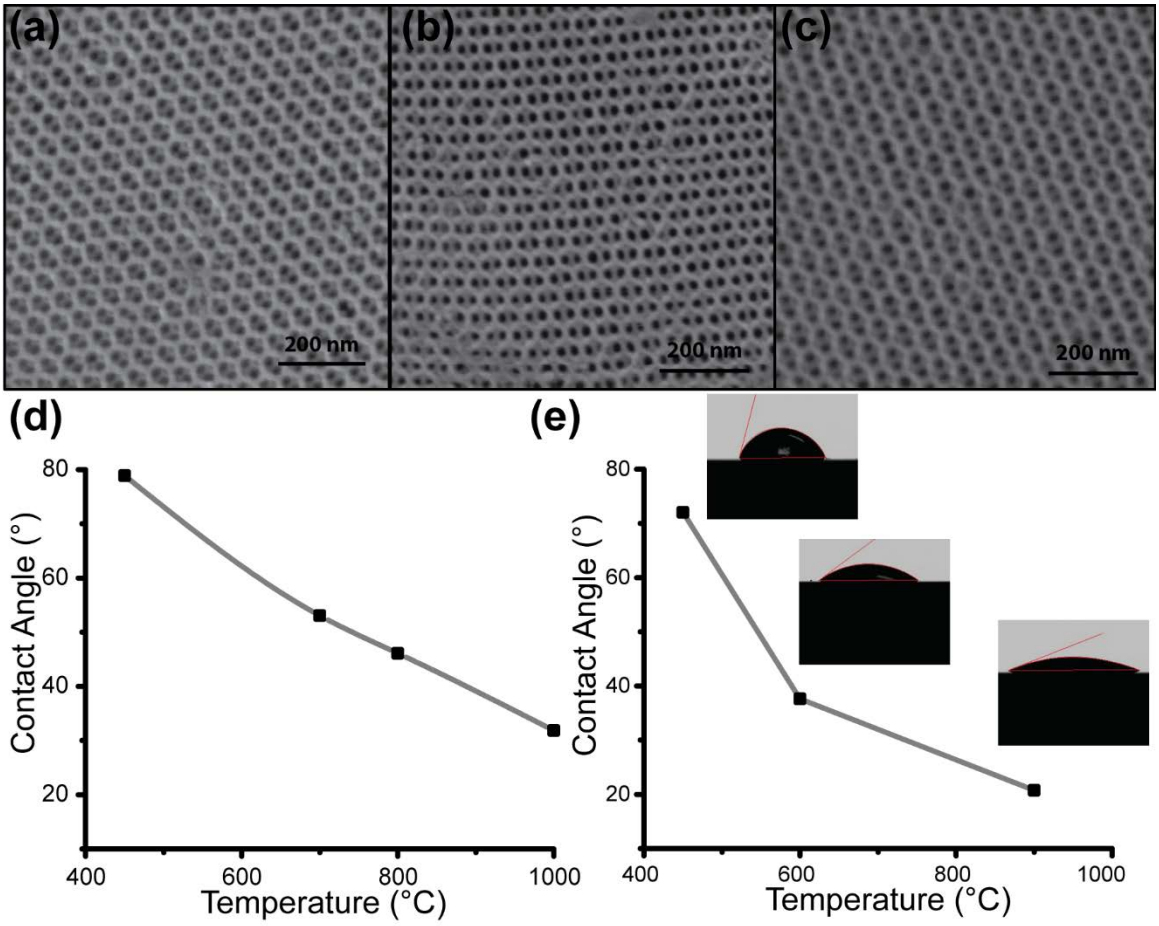

Figure 2.6 SEM images of ISO69-G^{A}MR thin films pyrolyzed to (a) 450 °C, (b) 600 °C, and (c) 900 °C, and contact angle measurements for thin film resin materials heat treated to different temperatures: (d) dense resin/carbon thin films and (e) G^{A}MR/C thin films. Grey lines are guides for the eye only.

GMR thin film transfer between different substrates

In order to increase their applicability as potential 3D templates, we finally demonstrated that these films could be transferred to arbitrary flat substrates. As is well known in the microelectronics field, substrates are crucial to materials deposition and bottom-up film growth. For instance, electroplating requires a substrate with a conductive seed layer and vapor-liquid-solid (VLS) growth of Si needs Au as a catalyst, while the epitaxial growth of single crystal

structures necessitates a specifically oriented single crystal substrate. Use of GMR thin films as templates in such materials growth/deposition methods would require their fabrication on different substrates. Changing substrates also changes surface energy, however, which in turn changes thin film-substrate interactions. Indeed, surface energy has been shown to have a substantial influence on solvent vapor annealing of BCPs,[50-52] resulting in time-consuming re-optimization requirements upon substrate switches, or even complete failure of desired BCP film formation outcomes. This is particularly true for more complex morphologies like ordered BCP gyroidal structures. Here, we demonstrate that such tedious re-optimization efforts can be avoided altogether by a simple film transfer technique, inspired by a widely-used graphene transfer method with PMMA as a protective layer.[32,33]

G^AMR and G^DMR thin film structures discussed so far were fabricated on Si substrates with native oxide layer typically present on commercially available Si wafers. This oxide layer conveniently served as a sacrificial layer helping thin film delamination from Si substrates when soaked in a HF-based bath. GMR thin films broke into small pieces, however, when removed from Si substrates in this way. To overcome this problem, a PMMA protective top layer was employed. The resulting transfer process is illustrated in Figure 2.7a with photos of the different steps shown in Figure 2.7b-j. A piece of a Si wafer of around 1.5 cm^2 with a G^AMR thin film on top (Figure 2.7b) was spin-coated with PMMA solution (M_n(PMMA) = 370 kg/mol, PDI =1.25, Polymer Source; 5 wt% solution in acetone) at 1500 rpm for 30s to form a PMMA protective layer on top of the thin film (Figure 2.7c). Film edges were subsequently cleaned with a razor blade to help the etching agent, *i.e.* HF, get in contact with the sacrificial oxide layer (Figure 2.7d). The thin film was then soaked in a buffered oxide etch (BOE) 6:1 (J.T. Baker) solution (Figure 2.7e). After approximately 3h, the PMMA/resin composite thin film delaminated from the original

silicon wafer and floated to the surface of the etching bath. The film was transferred to a DI water bath (Figure 2.7f) and carefully scooped out with the target substrate, in this case a gold-coated wafer (Figure 2.7g). The film on gold was then blow-dried with N_2 helping the film to stabilize on the new substrate (Figure 2.7h). Finally, soaking the PMMA/resin composite thin film in acetone overnight removed the PMMA protective layer completing the transfer process (Figure 2.7i). To further demonstrate the versatility of this process, a G^AMR thin film was also transferred onto a flexible substrate (indium tin oxide/ITO coated PET, 100 Ω/sq, Sigma-Aldrich), which is commonly used in microelectronics[53] (Figure 2.7j). Apart from surface energy effects that would have required time consuming re-optimization steps for this new substrate, GMR thin film structures are not directly accessible on such polymer based substrates due to their incompatibility with high temperature treatment steps during GMR fabrication.

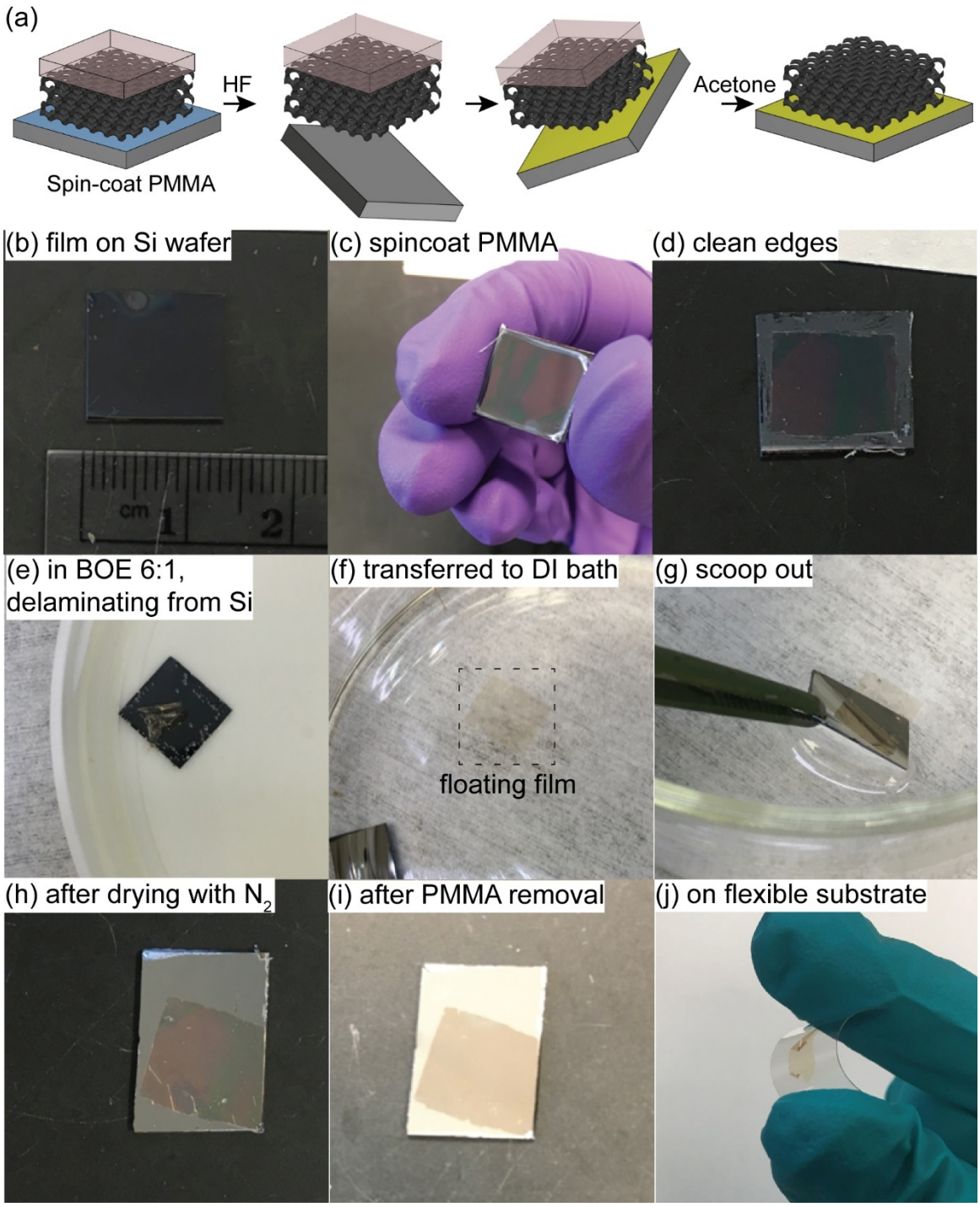

Figure 2.7 (a) Illustration of GMR thin film transfer technique, and photos taken of different steps during the G^{A}MR transfer process onto (b-i) gold-coated wafer and (j) flexible ITO coated PET.

Figure 2.8 shows SEM images of thin film structures after successful transfer onto gold-coated substrates. Top surface and cross-sectional images confirm that both $G^{A}MR$ and $G^{D}MR$ structures were successfully maintained after transfer onto a gold-coated wafer. In low magnification SEM images "wrinkles" were occasionally observed in the transferred $G^{A}MR$ thin films (see Figure 2.8c and d) due to insufficient spreading of the film on the new substrate. SEM images of $G^{A}MR$ thin films after transfer onto an ITO coated PET substrate are shown in Figure S2.9. We expect this transfer method to work for many different types of flat substrates, which should largely expand the application of these 3D networked thin film structures in nanomaterials fabrication.

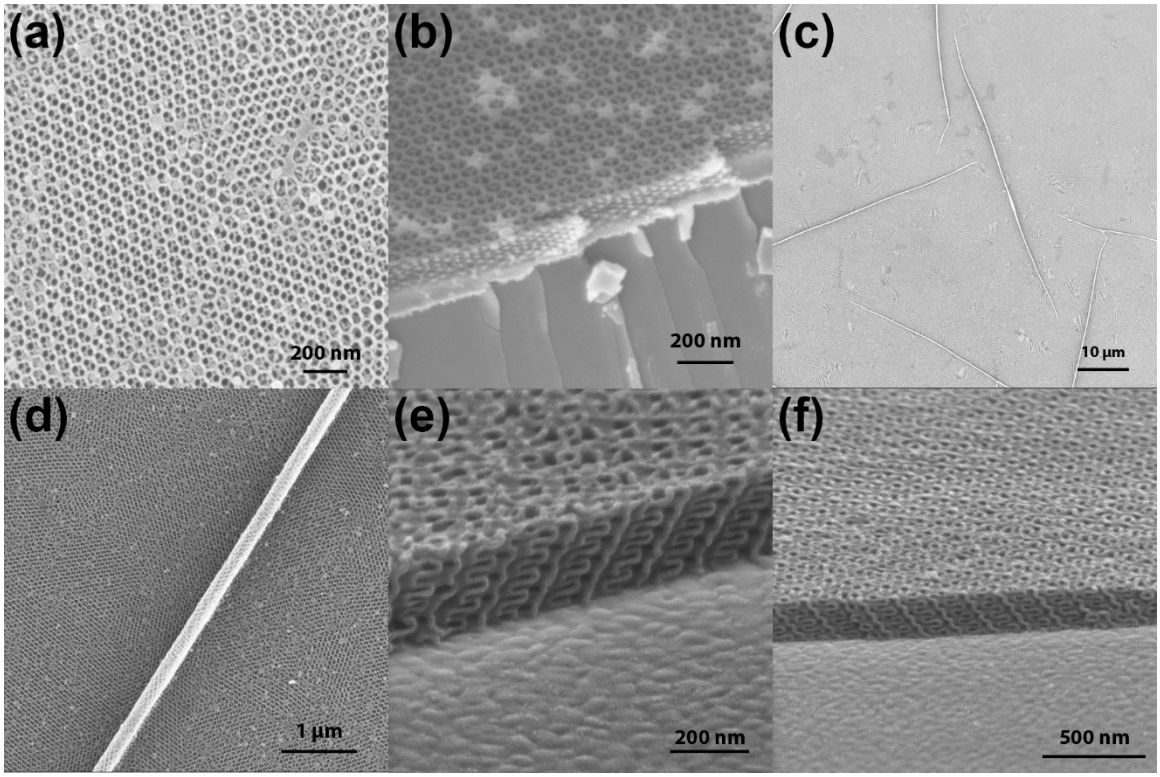

Figure 2.8 SEM images of (a-d) $G^{A}MR$ thin films and (e,f) $G^{D}MR$ thin films after transfer onto gold coated substrates.

Conclusion

In this report, we demonstrated the synthesis of mesoporous resin or carbon thin films with either alternating or double gyroid 3D structure. For the case of the alternating gyroid structure we used a combination of *in situ* reflectometry and *in situ* GISAXS to elucidate structural film evolution during solvent vapor annealing, leading to a reproducible pathway to mesoporous resin and carbon thin films with this structure. We subsequently highlighted the versatility of the resulting 3D structure for nanomaterials formation: Thin film pore size could be tailored by ISO molar mass; Pore surface energy/hydrophilicity could be tuned by heating to different temperatures between 400 °C and 1000 °C; This is expected to be beneficial for materials deposition into the small nanoscale pores by allowing to match template surface energy to that of the back-filling material; High temperature durability under inert gas environments renders thin films compatible with typical deposition methods used in the microelectronics industry such as CVD; It simultaneously provides functional templates with electrical conductivity as required, *e.g.* in on-chip battery devices. The demonstrated ability to transfer these thin films to other desired substrates eliminates time-consuming re-optimization steps of thin film formation, enables the use of substrates that otherwise are not compatible with high temperature formation steps (*e.g.* flexible polymer substrates), and tremendously expands the use of these potential 3D templates for various established back-filling and growth techniques. With these results the GMR/C thin films reported in this work present an advanced materials platform, which we hope will be useful to a range of fundamental and applied nanomaterials research efforts at the characteristic sub-100 nm length scale.

Methods

Synthesis

Three ISO terpolymers with number average molar mass, M_n, of 77, 69, and 28 kg/mol (*i.e.* ISO77, ISO69, and ISO28) and varying compositions were synthesized *via* sequential anionic polymerization as described previously.[54] Polymer characterization details are listed in Table 1. Oligomeric resorcinol-formaldehyde resols and phenol-formaldehyde resols were synthesized *via* well-known polymerization of resorcinol/phenol and formaldehyde under basic conditions as described in ref. 24. Resorcinol-formaldehyde resols and phenol-formaldehyde resols were both characterized by GPC in THF with UV detector at 254 nm wavelength. GPC traces of resorcinol-formaldehyde resols and phenol-formaldehyde resols, as well as of resorcinol and phenol molecules are shown in Figure S2.10. By comparing Figure S2.10 a and b, as well as Figure S2.10 c and d, we see that the peaks at elution volumes of 9.7 ml are from unreacted resorcinol or phenol molecules, respectively. We therefore only integrated the parts that eluted faster than these peaks for resorcinol-formaldehyde and phenol-formaldehyde resols' molar mass assessements, respectively. From these analyses, resorcinol-formaldehyde and phenol-formaldehyde resols were, respectively characterized as follows: M_n = 580 g/mol, M_w = 630, and PDI = 1.08; Mn = 360 g/mol, Mw = 370 g/mol, and PDI = 1.02 (using PS standards in both cases).

Thin film preparation

Two types of gyroidal mesoporous resin thin films with either alternating gyroid (G^AMR) or double gyroid (G^DMR) structure were achieved. G^AMR formation started with an ISO plus resorcinol-resols hybrid solution while G^DMR formation started with an ISO plus phenol-resols hybrid solution. The amount of resols added to the solutions was calculated to match the

PEO+resols weight percentage as listed in Table 1. The final ISO+resols solutions had a total concentration of 5 wt% in THF for resorcinol-resols based solutions and 10 wt% in THF for phenol-resols based solutions, respectively. ISO terpolymers were dissolved in THF and stirred for 30 min, followed by the addition of resols stock solution. After stirring for another 1 hour for ISO+resorcinol-resols solutions and 24 hours for ISO+phenol-resols solutions, thin films were spin-coated in a dry box with relative humidity maintained below 30%. Two types of thin films with targeted alternating gyroidal mesoporous resin structure, *i.e.* ISO69-G^AMR and ISO77-G^AMR, were spin-coated on silicon substrates at a speed of 3000 rpm for 1 min. Films with targeted double gyroidal mesoporous resin structure, ISO28-G^DMR, were spin-coated on silicon substrates at a speed of 1000 rpm for 1min. As-spun films were subjected to different solvent annealing procedures to achieve the desired mesostructures. Films with targeted G^A structure were annealed in THF vapor at room temperature (24 °C) in a flow chamber illustrated in Figure S2.1 (see Supporting Information). Dry nitrogen gas (N_2) was passed through two flow meters. One N_2 stream then went directly into the annealing chamber, referred as the dry line. Another N_2 stream went into a THF solvent reservoir after passing the flow meter and before entering the annealing chamber, referred to as the wet line. The annealing chamber was adapted from a cylindrical bottle with a bottom diameter of 4.5 cm and a height of 9.5 cm. The solvent reservoir was adapted from a conical flask with a bottom diameter of 7.5 cm and a height of 13 cm. The volume of THF in the solvent reservoir was kept around 175 ml. By adjusting flow rates of dry and wet lines, different swelling ratios of the films were achieved. At the beginning of the solvent annealing process the flow rates of dry and wet lines were set as 1.5 SCFH (wet) and 0.2 SCFH (dry) to achieve a relatively high swelling ratio. Flow rates were then adjusted stepwise every 2 mins to 1.5 SCFH (wet) and 0.3 SCFH (dry), 1.5 SCFH (wet) and 0.4 SCFH (dry), 1.25 SCFH

(wet) and 0.4 SCFH (dry), and 1 SCFH (wet) and 0.4 SCFH (dry) to slowly decrease the swelling ratio of the thin film. After staying at 1 SCFH (wet) and 0.4 SCFH (dry) for 2 min, the films were quenched by closing the wet line flow and increasing the dry line flow to its maximum.

For films with targeted G^D structure, the as-spun thin films were first placed onto a vial turned upside down serving as a stage. The film, vial and a petri dish filled with 10 ml of chloroform were then put under a glass dome. The set up was heated on a hotplate at 50 °C for 1 hour, then removed from the hotplate and left under ambient conditions until the remaining chloroform evaporated, usually approximately 40 hours.

After solvent annealing, thin films were cured in an oven at 115 °C for 24 hours to cross-link the resols. Surface capping layers were observed for thin films with double gyroid morphology, hence an extra etching step was required. To that end, cured G^D films were treated with tetrafluoromethane (CF_4) plasma at forward power of 150 W for 4 min to remove the capping layers in an Oxford PlasmaLab 80+ RIE System. After cross-linking (and surface etching for G^D samples) thin films were heated at a rate of 1 °C min^{-1} to 450 °C and pyrolyzed under inert atmosphere (nitrogen or argon) at 450 °C for 3 hours, generating G^AMR or G^DMR thin films. Thin films pyrolyzed at higher temperatures were brought to the final temperature at a rate of 1 °C/min after being stabilized at 450 °C for 3 hours, then remained at the final temperature for another 3 hours. Such heat treatments at final temperatures of 600 °C or higher generated gyroidal mesoporous carbon (GMC) thin films.

Preparation of gold coated wafers

Gold coated Si wafers were either purchased from Sigma Aldrich (99.999% (Au), layer thickness 1000 Å, with titanium as an adhesion layer to bind gold to the silicon wafer) or prepared

via thermally evaporating gold onto Si wafers using CHA SE-600 thermal evaporator. To that end, a 10 nm Cr adhesive layer was first evaporated at a speed of 1Å/sec. A gold layer was subsequently evaporated at a speed of 1Å/sec. The final thickness of the gold layer was around 10 nm.

Materials characterization

Triblock terpolymer molar mass, composition, and polydispersity were determined by a combination of gel permeation chromatography (GPC) and ^{1}H nuclear magnetic resonance (^{1}H NMR) spectroscopy. Scanning electron microscopy (SEM) images of thin films were acquired on a Tescan LM Mira3 FE-SEM with an in-lens detector. Grazing-incidence small-angle X-ray scattering (GISAXS) patterns of thin film structures as shown in Figure 2.3 were acquired at Sector 8-ID-E[55] at the Advanced Photon Source at Argonne National Laboratory with sample-to-detector distance of 2.2 m and incident photon energy of 10.86 keV. Patterns were recorded with a Pilatus 1M detector, and the X-ray beam was 20μm in height and 100μm in width. GISAXS patterns as shown in Figure S2.6 were acquired at beamline G1 at Cornell's High Energy Synchrotron Source (CHESS), with sample-to-detector distance of 2.2 m and incident photon energy of 9.83 keV. Patterns were recorded on a Dectris Pilatus3-200k pixel array detector with an incident beam of 250 μm x 250 μm defined using a standard three-slit setup.

Combined *in situ* GISAXS/reflectometry measurements during solvent vapor annealing

In situ GISAXS patterns shown in Figure 2.4 were acquired at beamline D1 at CHESS, with sample-to-detector distance of 1.8 m and incident photon energy of 10.6 keV. Patterns were recorded on a Dectris Pilatus3-200k pixel array detector. A custom-built vapor annealing chamber used during *in situ* GISAXS experiments was set up at CHESS beamline D1. An illustration

depicting the apparatus is shown in Figure S2.2 (for a photograph of the annealing chamber see Figure 6 of ref. 40). The solvent vapor concentration inside the chamber was controlled by N_2 passing through two flow meters. One N_2 stream after passing a first flow meter went directly into the annealing chamber, and will be referred to as the "dry line". Another N_2 stream after passing a second flow meter first went into a THF solvent reservoir before entering the annealing chamber, and will be referred to as the "wet line". Wet and dry lines mixed before entering the annealing chamber. Two flow meters controlling wet and dry lines were tuned constantly during annealing to maintain the desired solvent-swollen film thickness, which was monitored *in situ* by optical reflectometry measurements (FilMetrics F30 reflectometer). Thickness measurements were taken at a spot which did not get exposed to x-rays during *in situ* GISAXS measurements. Both GISAXS patterns and reflectometry measurements were collected automatically every 5 seconds during the solvent vapor annealing process.

Conductivity measurements

Conductivity measurements were performed by directly contacting the surfaces of films treated at 450 °C and 900 °C, respectively, using an in-line four-point probe setup (Everbeing International Corp.) with a Keithley 2400 sourcemeter. Voltage (V)-current (I) sweeps were performed for 4 spatial points on each film over the range of ± 7 V for the 900 °C films and ± 100 V for the 450 ˚C films. Sweeps were linear in all cases. Linear slopes were employed to calculate sheet resistance (R_s) using the well-known equation in the limit of a very thin film relative to the probe spacing of $R_s = \pi/\ln(2)V/I$. Resistivity was also calculated using $R=R_S \cdot t$, with an approximated film thickness, t. The films tested were fabricated on thermal oxides (100 nm) to eliminate conductivity contributions from substrates.

Acknowledgments

This work was funded by the National Science Foundation (DMR-1707836). P.A.B. was supported by the NSF Graduate Research Fellowship Program (DGE-1650441). This work made use of the Cornell Center for Materials Research Shared Facilities which are supported through the NSF MRSEC program (DMR-1120296), Cornell NanoScale Facility (CNF), a member of the National Nanotechnology Coordinated Infrastructure (NNCI), which is supported by the National Science Foundation (Grant ECCS-1542081), the Cornell High Energy Synchrotron Source (CHESS) which is supported by the National Science Foundation under award DMR-1332208, and the Advanced Photon Source (APS), a U.S. Department of Energy (DOE) Office of Science User Facility operated for the DOE Office of Science by Argonne National Laboratory under Contract No. DE-AC02-06CH11357. Q.Z acknowledges Y. Li (Wiesner group, Cornell University), M. Dolejsi (Nealey group, University of Chicago) and T. Segal-Peretz (Nealey group, University of Chicago) for helpful discussions. H.S.S and S.X. acknowledges Z. Jiang (APS) for his help with beamline setup. H.S.S., S.X. and P.F.N gratefully acknowledge support by U.S. Department of Energy, Basic Energy Sciences, Argonne National Laboratory, Materials Sciences, and Engineering Division for aspects of the work related to GISAXS and solvent vapor annealing. K.W.T. acknowledges a startup grant from Nanyang Technological University.

REFERENCES

1. Zhang, H.; Yu, X.; Braun, P. V. Three-Dimensional Bicontinuous Ultrafast-Charge and-Discharge Bulk Battery Electrodes. *Nat. Nanotechnol.* **2011**, *6*, 277-281.
2. Kim, O. H.; Cho, Y. H.; Kang, S. H.; Park, H. Y.; Kim, M.; Lim, J. W.; Chung, D. Y.; Lee, M. J.; Choe, H.; Sung, Y. E. Ordered Macroporous Platinum Electrode and Enhanced Mass Transfer in Fuel Cells Using Inverse Opal Structure. *Nat. Commun.* **2013**, *4*, 2473.
3. Kim, J. E.; Oh, J. H.; Kotal, M.; Koratkar, N.; Oh, I. K. Self-Assembly and Morphological Control of Three-Dimensional Macroporous Architectures Built of Two-Dimensional Materials. *Nano Today* **2017**, *14*, 100-123.
4. Braun, P. V. Materials Chemistry in 3D Templates for Functional Photonics. *Chem. Mater.* **2013**, *26*, 277-286.
5. Hur, K.; Francescato, Y.; Giannini, V.; Maier, S. A.; Hennig, R. G.; Wiesner, U. Three-Dimensionally Isotropic Negative Refractive Index Materials from Block Copolymer Self-Assembled Chiral Gyroid Networks. *Angew. Chem. Inter. Ed.* **2011**, *50*, 11985-11989.
6. Bauer, J.; Schroer, A.; Schwaiger, R.; Kraft, O. Approaching Theoretical Strength in Glassy Carbon Nanolattices. *Nat. Mater.* **2016**, *15*, 438-443.
7. Lee, J. H.; Singer, J. P.; Thomas, E. L. Micro-/Nanostructured Mechanical Metamaterials. *Adv. Mater.* **2012**, *24*, 4782-4810.
8. Valev, V. K.; Baumberg, J. J.; Sibilia, C.; Verbiest, T. Chirality and Chiroptical Effects in Plasmonic Nanostructures: Fundamentals, Recent progress, and Outlook. *Adv. Mater.* **2013**, *25*, 2517-2534.
9. Salvatore, S.; Demetriadou, A.; Vignolini, S.; Oh, S. S.; Wuestner, S.; Yufa, N. A.; Stefik, M.; Wiesner, U.; Baumberg, J.J.; Hess, O.; Steiner, U. Tunable 3D Extended Self-Assembled Gold Metamaterials with Enhanced Light Transmission. *Adv. Mater.* **2013**, *25*, 2713-2716.
10. Dolan, J. A.; Wilts, B. D.; Vignolini, S.; Baumberg, J. J.; Steiner, U.; Wilkinson, T. D. Optical Properties of Gyroid Structured Materials: from Photonic Crystals to Metamaterials. *Adv. Opt. Mater.* **2015**, *3*, 12-32.

11. Shimmin, R. G.; Vajtai, R.; Siegel, R. W.; Braun, P. V. Room-Temperature Assembly of Germanium Photonic Crystals through Colloidal Crystal Templating. *Chem. Mater.* **2007**, *19*, 2102-2107.
12. von Freymann, G.; Kitaev, V.; Lotsch, B. V.; Ozin, G. A. Bottom-Up Assembly of Photonic Crystals. *Chem. Soc. Rev.* **2013**, *42*, 2528-2554.
13. Tan, K. W.; Saba, S. A.; Arora, H.; Thompson, M. O.; Wiesner, U. Colloidal Self-Assembly-Directed Laser-Induced Non-Close-Packed Crystalline Silicon Nanostructures. *ACS Nano* **2011**, *5*, 7960-7966.
14. Selimis, A.; Mironov, V.; Farsari, M. Direct laser writing: Principles and Materials for Scaffold 3D Printing. *Microelectron. Eng.* **2015**, *132*, 83-89.
15. Brüser, B.; Staude, I.; von Freymann, G.; Wegener, M.; Pietsch, U. Visible Light Laue Diffraction from Woodpile Photonic Crystals. *Appl. Optics* **2012**, *51*, 6732-6737.
16. Arora, H.; Du, P.; Tan, K. W.; Hyun, J. K.; Grazul, J.; Xin, H. L.; Muller, D.A.; Thompson, M.O.; Wiesner, U. Block Copolymer Self-Assembly–Directed Single-Crystal Homo-and Heteroepitaxial Nanostructures. *Science* **2010**, *330*, 214-219.
17. Park, S.; Kim, Y.; Ahn, H.; Kim, J. H.; Yoo, P. J.; Ryu, D. Y. Giant Gyroid and Templates from High-Molecular-Weight Block Copolymer Self-assembly. *Sci. Rep.* **2016**, *6*.
18. Crossland, E. J.; Kamperman, M.; Nedelcu, M.; Ducati, C.; Wiesner, U.; Smilgies, D. M.; Toombes, G.E.; Hillmyer, M.A.; Ludwigs, S.; Steiner, U.; Snaith, H. J. A Bicontinuous Double Gyroid Hybrid Solar Cell. *Nano Lett.* **2008**, *9*, 2807-2812.
19. Scherer, M. R.; Li, L.; Cunha, P.; Scherman, O. A.; Steiner, U. Enhanced Electrochromism in Gyroid-Structured Vanadium Pentoxide. *Adv. Mater.* **2012**, *24*, 1217-1221.
20. Scherer, M. R.; Steiner, U. Efficient Electrochromic Devices Made from 3D Nanotubular Gyroid Networks. *Nano Lett.* **2012**, *13*, 3005-3010.
21. Salvatore, S.; Vignolini, S.; Philpott, J.; Stefik, M.; Wiesner, U.; Baumberg, J. J.; Steiner, U. A High Transmission Wave-Guide Wire Network Made by Self-assembly. *Nanoscale* **2014**, *7*, 1032-1036.
22. Cowman, C. D.; Padgett, E.; Tan, K. W.; Hovden, R.; Gu, Y.; Andrejevic, N. Muller, D.; Coates, G.W.; Wiesner, U. Multicomponent Nanomaterials with Complex Networked Architectures from Orthogonal Degradation and Binary Metal Backfilling in ABC Triblock Terpolymers. *J. Am. Chem. Soc.* **2015**, *137*, 6026-6033.

23. Hsueh, H. Y.; Yao, C. T.; Ho, R. M. Well-Ordered Nanohybrids and Nanoporous Materials from Gyroid Block Copolymer Templates. *Chem. Soc. Rev.* **2015**, 44, 1974-2018.
24. Werner, J. G.; Hoheisel, T. N.; Wiesner, U. Synthesis and Characterization of Gyroidal Mesoporous Carbons and Carbon Monoliths with Tunable Ultralarge Pore Size. *ACS Nano* **2013**, *8*, 731-743.
25. Werner J. G.; Johnson S. S., Vijay V.; Wiesner U. Carbon-Sulfur Composites from Cylindrical and Gyroidal Mesoporous Carbons with Tunable Properties in Lithium-Sulfur Batteries, *Chem. Mater.* **2015**, *27*, 3349–3357.
26. Werner J. G.; Scherer M. R. J.; Steiner U.; Wiesner U. Gyroidal Mesoporous Multifunctional Nanocomposites *via* Atomic Layer Deposition, Nanoscale 2014, 6, 8736-8742.
27. Tan, K. W.; Jung, B., Werner, J. G.; Rhoades, E. R.; Thompson, M. O.; Wiesner, U. Transient Laser Heating Induced Hierarchical Porous Structures from Block Copolymer–Directed Self-Assembly. *Science*, **2015**, *349*, 54-58.
28. Deng, G.; Zhang, Y.; Ye, C.; Qiang, Z.; Stein, G. E.; Cavicchi, K. A.; Vogt, B. D. Bicontinuous Mesoporous Carbon Thin Films *via* an Order–Order Transition. *Chem. Commun.* **2014**, *50*, 12684-12687.
29. Qiang, Z.; Xue, J.; Cavicchi, K. A.; Vogt, B. D. Morphology Control in Mesoporous Carbon Films Using Solvent Vapor Annealing. *Langmuir*, **2013** 29, 3428-3438.
30. Zhou, Z.; Liu, G. Controlling the Pore Size of Mesoporous Carbon Thin Films through Thermal and Solvent Annealing. *Small*, **2017** 13, 1603107.
31. Albert, J. N.; Epps, T. H. Self-Assembly of Block Copolymer Thin Films. *Materials Today* **2010**, 13, 24-33.
32. Gao, T.; Li, Z.; Huang, P. S.; Shenoy, G. J.; Parobek, D.; Tan, S.; Lee, J.K.; Liu, H.; Leu, P. W. Hierarchical Graphene/Metal Grid Structures for Stable, Flexible Transparent Conductors. *ACS Nano* **2015**, *9*, 5440-5446.
33. Li, X.; Zhu, Y.; Cai, W.; Borysiak, M.; Han, B.; Chen, D.; Piner, R. D.; Colombo, L.; Ruoff, R. S. Transfer of Large-Area Graphene Films for High-Performance Transparent Conductive Electrodes. *Nano Lett.* **2009**, *9*, 4359-4363.

34. Gurarslan, A.; Yu, Y.; Su, L.; Yu, Y.; Suarez, F.; Yao, S.; Zhu, Y.; Ozturk, M.; Zhang, Y.; Cao, L. Surface-Energy-Assisted Perfect Transfer of Centimeter-Scale Monolayer and Few-Layer MoS2 Films onto Arbitrary Substrates. *ACS nano*, **2014** *8*, 11522-11528.
35. Feng, D.; Lv, Y.; Wu, Z.; Dou, Y.; Han, L.; Sun, Z.; Xia, Y.; Zheng, G.; Zhao, D. Free-Standing Mesoporous Carbon Thin Films with Highly Ordered Pore Architectures for Nanodevices. *J. Am. Chem. Soc.*, **2011** 133, 15148-15156.
36. Chatterjee, J.; Jain, S.; Bates, F. S. Comprehensive Phase Behavior of Poly(Isoprene-b-Styrene-b-Ethylene Oxide) Triblock Copolymers. *Macromolecules* **2007** 40, 2882-2896.
37. Jiang, Z. GIXSGUI: a MATLAB Toolbox for Grazing-Incidence X-Ray Scattering Data Visualization and Reduction, and Indexing of Buried Three-Dimensional Periodic Nanostructured Films. *J. Appl. Cryst.* **2015**, *48*, 917-926.
38. Epps, T. H.; Cochran, E. W.; Bailey, T. S.; Waletzko, R. S.; Hardy, C. M.; Bates, F. S. Ordered Network Phases in Linear Poly (Isoprene-b-Styrene-b-Ethylene Oxide) Triblock Copolymers. *Macromolecules* **2004**, *37*, 8325-8341.
39. Tanaka, S.; Katayama, Y.; Tate, M. P.; Hillhouse, H. W.; Miyake, Y. Fabrication of Continuous Mesoporous Carbon Films with Face-Centered Orthorhombic Symmetry through a Soft Templating Pathway. *J. Mater. Chem*, **2007** 17, 3639-3645.
40. Posselt, D.; Zhang, J.; Smilgies, D. M.; Berezkin, A. V.; Potemkin, I. I.; Papadakis, C. M. Restructuring in Block Copolymer Thin Films: *In Situ* GISAXS Investigations during Solvent Vapor Annealing. *Prog. Polym. Sci.* **2017** 66, 80-115.
41. Schuster, J.; Köhn, R.; Döblinger, M.; Keilbach, A.; Amenitsch, H.; Bein, T. *In Situ* SAXS Study on a New Mechanism for Mesostructure Formation of Ordered Mesoporous Carbons: Thermally Induced Self-Assembly. *J. Am. Chem. Soc.* **2012** 134, 11136-11145.
42. Chavis, M. A.; Smilgies, D. M.; Wiesner, U. B.; Ober, C. K. Widely Tunable Morphologies in Block Copolymer Thin Films through Solvent Vapor Annealing Using Mixtures of Selective Solvents. *Adv. Funct. Mater.* **2015** 25, 3057-3065.
43. Bai, W.; Yager, K. G.; Ross, C. A. *In Situ* Characterization of the Self-Assembly of a Polystyrene–Polydimethylsiloxane Block Copolymer During Solvent Vapor Annealing. *Macromolecules.* **2015** 48, 8574-8584.
44. Shin, C.; Ryu, D. Y.; Huh, J.; Kim, J. H.; Kim, K. W. Order-to-Order Transitions of Block Copolymer in Film Geometry. *Macromolecules.* **2009** 42, 2157-2160.

45. Shelton, C. K.; Epps, T. H. Block Copolymer Thin Films: Characterizing Nanostructure Evolution with *in Situ* X-Ray and Neutron Scattering. *Polymer* **2016** 105, 545-561.
46. Smilgies D. M.; Blasini D. R. Indexation Scheme for Oriented Molecular Thin Films Studied with Grazing-Incidence Reciprocal-Space Mapping. *J. Appl. Cryst.* **2007** 40, 716-718.
47. Busch, P.; Rauscher, M.; Smilgies, D. M.; Posselt, D.; Papadakis, C. M. Grazing-Incidence Small-Angle X-Ray Scattering (GISAXS) from Thin, Nanostructured Block Copolymer Films–The Scattering Cross-Section in the Distorted-Wave Born Approximation. *J. Appl. Cryst*, **2006** *39*, 433.
48. Albert, J. N.; Young, W. S.; Lewis III, R. L.; Bogart, T. D.; Smith, J. R.; Epps III, T. H. Systematic Study on the Effect of Solvent Removal Rate on the Morphology of Solvent Vapor Annealed ABA Triblock Copolymer Thin Films. *ACS Nano*, **2011** 6, 459-466.
49. Li, X.; Larson, A. B.; Jiang, L.; Song, L.; Prichard, T.; Chawla, N.; Vogt, B. D. Evolution of Mechanical, Optical and Electrical Properties of Self-Assembled Mesostructured Phenolic Resins during Carbonization. *Microporous Mesoporous Mater*. **2011** 138, 86-93.
50. Epps, T. H.; DeLongchamp, D. M.; Fasolka, M. J.; Fischer, D. A.; Jablonski, E. L. Substrate Surface Energy Dependent Morphology and Dewetting in an ABC Triblock Copolymer Film. *Langmuir* **2007**, *23*, 3355-3362.
51. Sinturel, C.; Vayer, M.; Morris, M.; Hillmyer, M. A. Solvent Vapor Annealing of Block Polymer Thin Films. *Macromolecules* **2013**, *46*, 5399-5415.
52. Wan, L.; Ji, S.; Liu, C. C.; Craig, G. S.; Nealey, P. F. Directed Self-Assembly of Solvent-Vapor-Induced Non-Bulk Block Copolymer Morphologies on Nanopatterned Substrates. *Soft Matter* **2016**, *12*, 2914-2922.
53. Mannsfeld, S. C.; Tee, B. C.; Stoltenberg, R. M.; Chen, C. V. H.; Barman, S.; Muir, B. V.; Sokolov, A. N.; Reese, C; Bao, Z. Highly Sensitive Flexible Pressure Sensors with Microstructured Rubber Dielectric Layers. *Nat. Mater.* **2010**, *9*, 859-864.
54. Bailey, T. S.; Hardy, C. M.; Epps, T. H.; Bates, F. S. A Noncubic Triply Periodic Network Morphology in Poly (Isoprene-b-Styrene-b-Ethylene Oxide) Triblock Copolymers. *Macromolecules* **2002**, *35*, 7007-7017.
55. Jiang, Z.; Li, X.; Strzalka, J.; Sprung, M.; Sun, T.; Sandy, A. R.; Narayanan, S.; Lee, D. R.; Wang, J. The Dedicated High-Resolution Grazing-Incidence X-Ray Scattering

Beamline 8-ID-E at the Advanced Photon Source. *J. Synchrotron Radiat.* **2012** 19, 627-636.

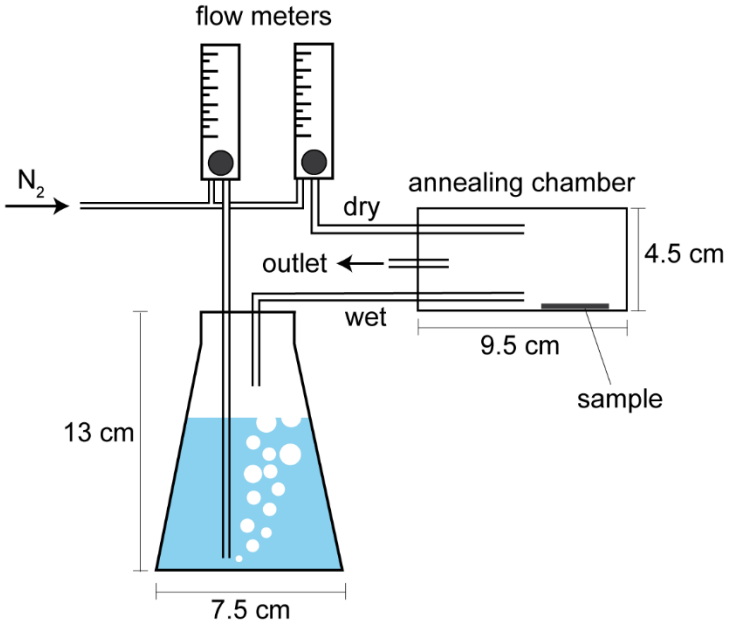

Figure S2.1 Illustration of flow chamber used for solvent vapor annealing of G^{A}MR thin films.

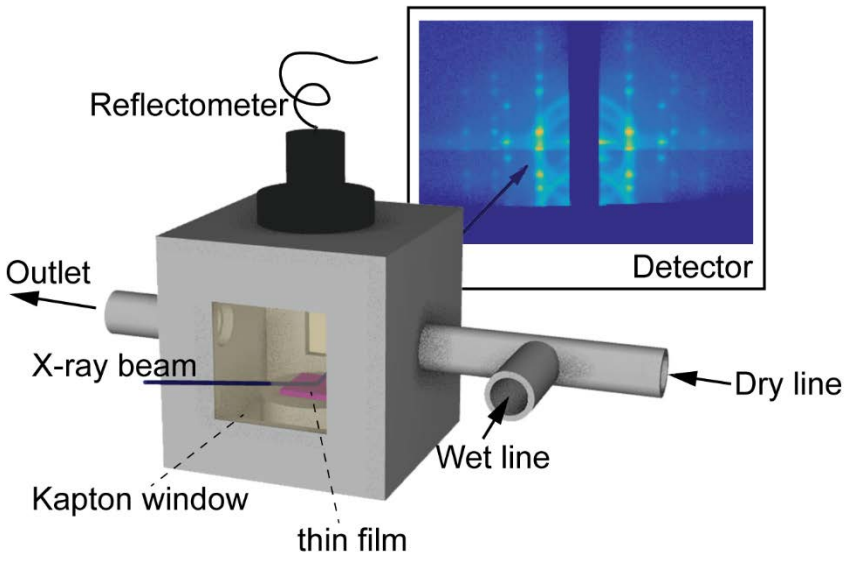

Figure S2.2 Illustration of flow chamber used in *in situ* GISAXS study at beamline D1 at CHESS.

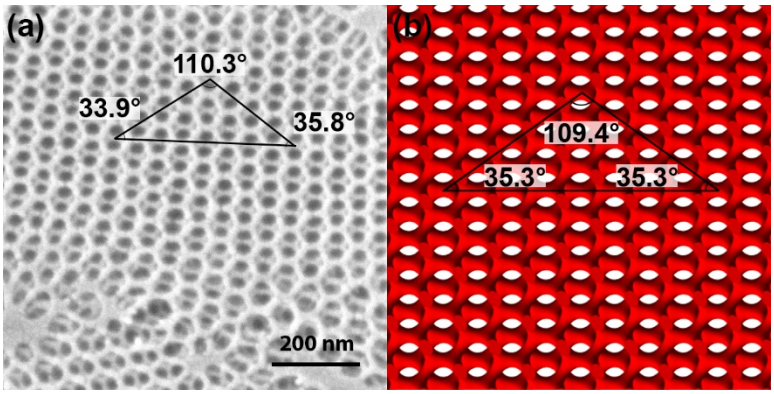

Figure S2.3 Comparison of several angles (a) measured from an SEM image of ISO77-G^AMR film and (b) calculated from an alternating gyroid model showing the (110) lattice plane. The similarity of measured and calculated angles further confirms that the top surface of this thin film is the (110) plane of the alternating gyroid, G^A.

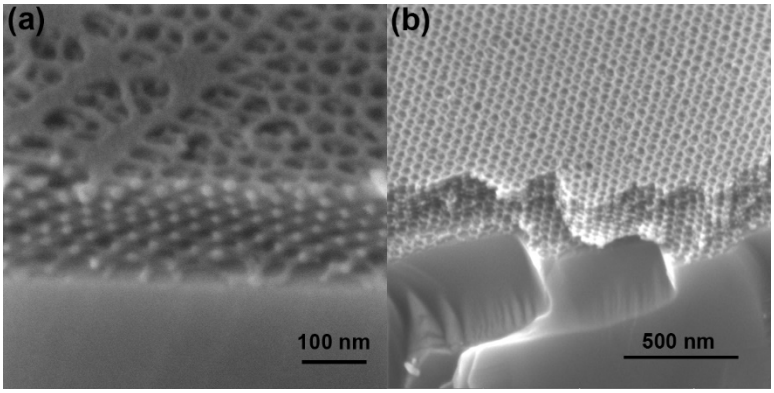

Figure S2.4 Cross-sectional images of (a) ISO77-G^AMR and (b) ISO69-G^AMR.

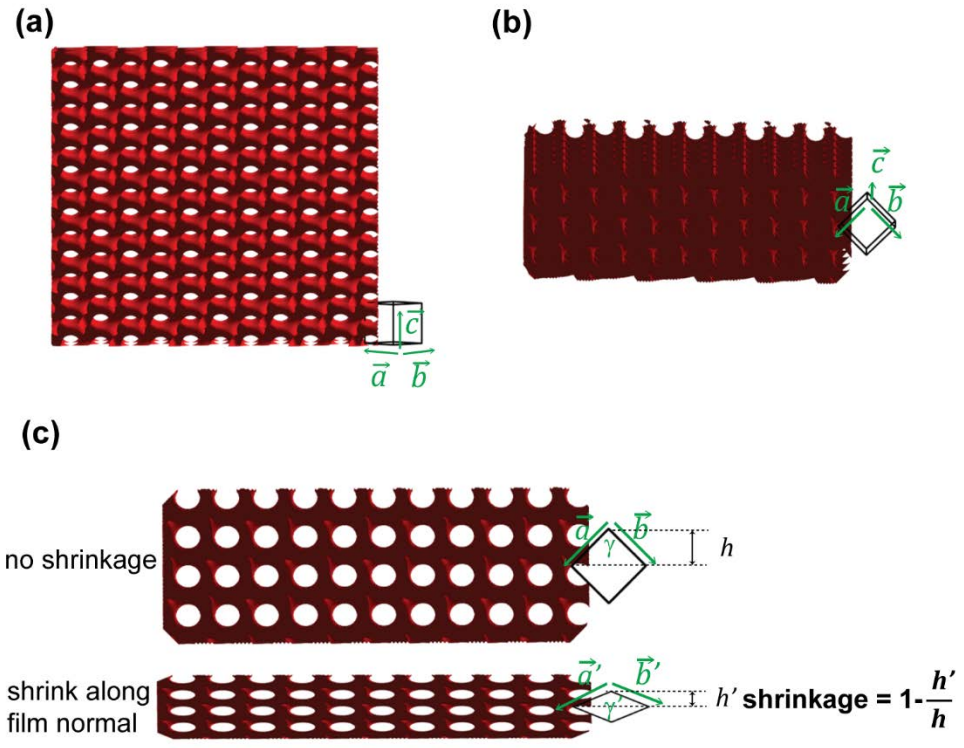

Figure S2.5 Alternating gyroid thin film model viewed from (a) top surface (along the [110] direction) and (b) cross-section (along the [0 0 1] direction). (c) Cross-sectional illustrations of thin films with and without shrinkage. The unit cell and unit cell vectors, $\vec{a}, \vec{b}, \vec{c}$, and angle γ are also shown in the illustration. An ideal thin film without shrinkage would have cubic unit cell with $a = b = c$ and $\gamma = 90°$. When the film shrinks along the film normal, *i.e.* along the [110] direction, the unit cell deforms to no longer have cubic symmetry. Due to the constraint within the (110) plane (*i.e.* film surface plane) provided by the substrate, we have $c' \approx c$. The shrinkage along the vertical direction (*i.e.* along the [110] direction) gives $a'=b'<a=b$ and $\gamma' > 90°$. By assuming $c' = c$, shrinkage of the film is calculated by $1 - \frac{h'}{h}$.

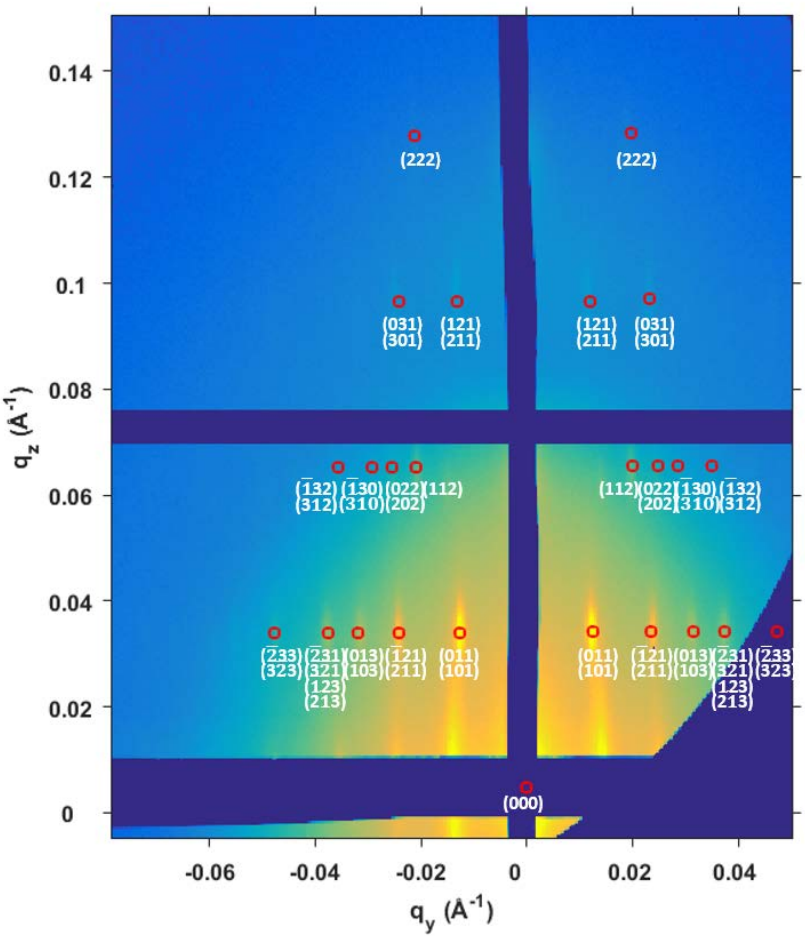

Figure S2.6 GISAXS pattern with indexing for ISO69-G^{A}MR. The basis coordinates were selected based on space group #214; unit cell parameters used for indexing were a = b = 44.8 nm, c = 61.2 nm, α = β = 90°, γ=154.2°, with [110] selected as the film normal direction. The shrinkage was determined as 77%. The incident angle for this measurement was 0.027°.

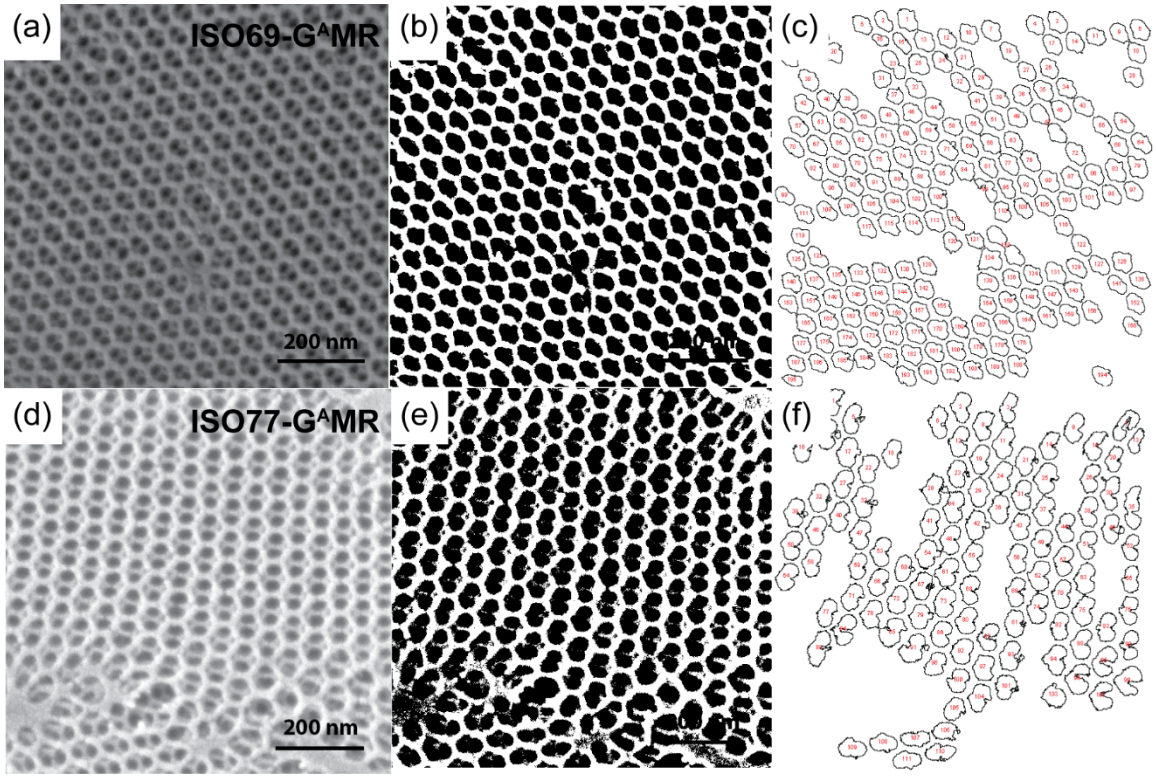

Figure S2.7 Image processing details for pore size analysis of (a-c) ISO69-G^AMR and (d-f) ISO77-G^AMR. (a,d) SEM images used for pore size analysis. (b,e) Set threshold of (a) and (c) as auto in ImageJ. A list of pore area values were obtained using ImageJ build-in function "analyze particles" and each pore used for calculation was traced and shown in (c) and (f). Pore area values were then plotted in histogram form in Figure 2.4 with a bin size of 200 nm^2 and fitted by a Gaussian distribution.

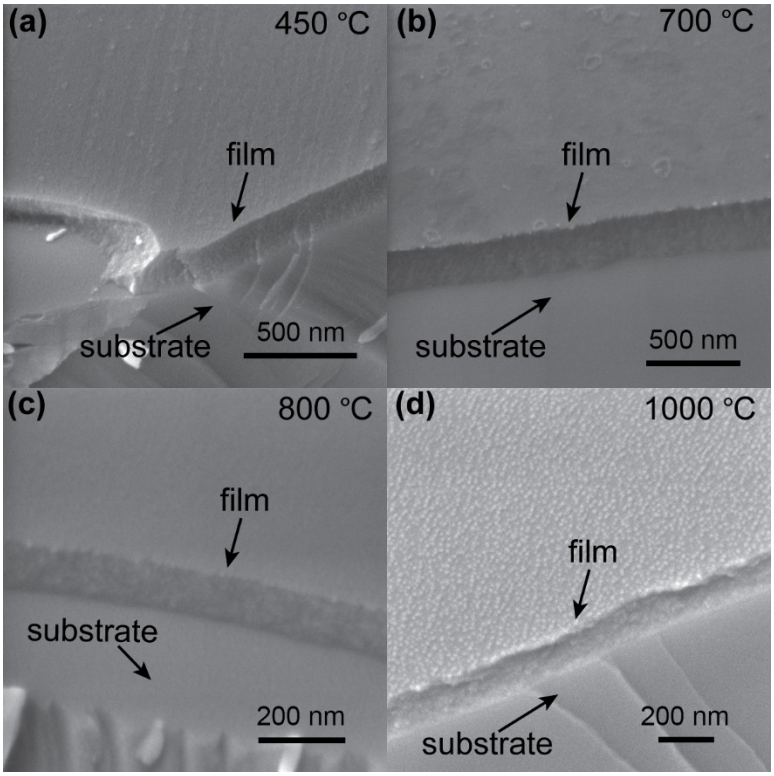

Figure S2.8 SEM images of dense resin/carbon thin films treated at (a) 450 °C, (b) 700 °C, (c) 800 °C, and (d) 1000 °C.

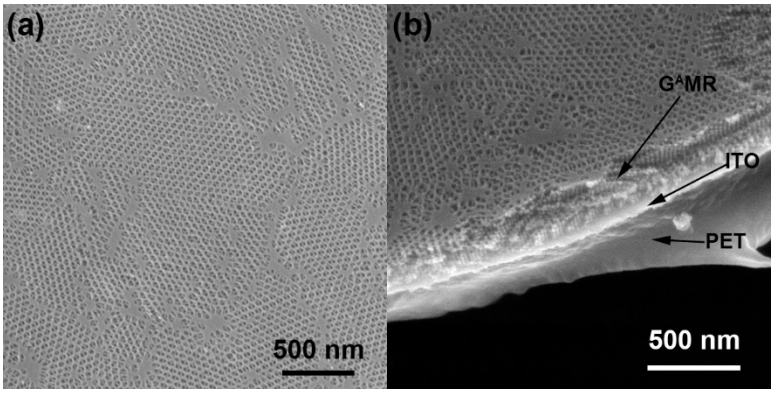

Figure S2.9 SEM images of $G^{A}MR$ thin films after transfer onto ITO coated PET substrates.

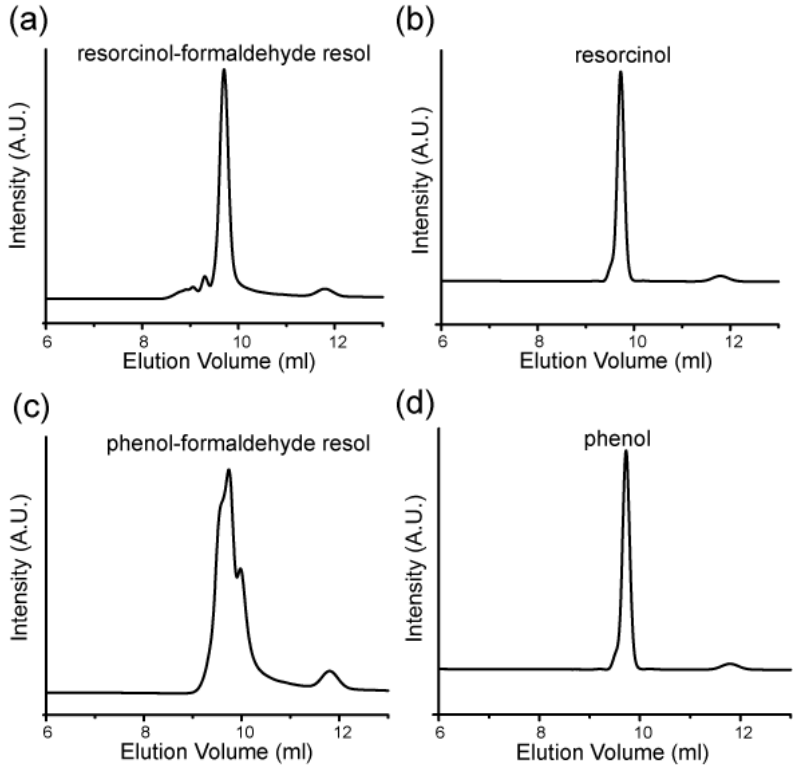

Figure S2.10 GPC traces of (a) resorcinol-formaldehyde resols, (b) resorcinol molecules, (c) phenol-formaldehyde resols, and (d) phenol molecules.

CHPATER 3

TUNING SUBSTRUCTURE AND PROPERTIES OF SUPPORTED ASYMMETRIC TRIBLOCK TERPOLYMER MEMBRANES[*]

Abstract

Asymmetric poly(isoprene-*b*-styrene-*b*-4-vinylpyridine) (ISV) block copolymer membranes fabricated via self-assembly and non-solvent induced phase separation (SNIPS) process have drawn significant attention due to the simple processing method and the generation of high-quality isoporous ultrafiltration membranes. With the present study on SNIPS membrane substructure, we systematically varied membrane casting parameters to tune the cross-sectional morphologies of SNIPS membranes while simultaneously preserving top surface structure. Parameters such as polymer concentration, evaporation time, solvent ratio, and coagulation bath temperature were investigated to control transformation of commonly produced sponge-like cross-sectional morphologies into more open and permeable finger-like substructures. Membranes with sponge-like and finger-like substructures were then integrated onto nylon supports for enhanced mechanical properties. Hydraulic permeability tests at various pH conditions gave distinct open-state flux values

for SNIPS membranes with different sublayer morphologies, while maintaining pH responsive functionality resulting from the poly(4-vinylpyridine) block.

---

[*] Reprinted (adapted) with permission from Q. Zhang, Y. M. Li, Y. Gu, R. M. Dorin, U. Wiesner, Tuning Substructure and Properties of Supported Asymmetric Triblock Terpolymer Membranes, *Polymer* **107**, 398-405 (2016). Copyright Elsevier.

Introduction

Polymeric membranes have widely been used in filtration fields because of their plentiful materials choices, robust mechanical properties, and compatibility with various fabrication techniques such as track-etching, lithography, and solvent based methods.[1]

Among these methods, membranes generated through non-solvent induced phase separation (NIPS) attract great interest due to the simple fabrication procedure and accessibility to a range of pore sizes under various casting conditions. The polymer, commonly a homopolymer (e.g. polysulfone[2]), is dissolved into a good solvent, casted on a substrate and immersed into a coagulation bath. As phase inversion occurs with the exchange of solvent and non-solvent (coagulant), membranes are formed by precipitation of the polymer. One of the most useful properties of NIPS membranes is the ability to tailor pore size with casting solution compositions and membrane casting conditions.[3] There are generally two types of cross-sectional membrane morphologies obtained through varying system conditions: 1) dense, sponge-like and 2) open, finger-like structures. Sponge-like and finger-like membranes are used as reverse osmosis and ultrafiltration membranes, respectively, due to their pore size distribution. Although widely used in industry, NIPS membranes are limited due to the trade-off between selectivity and permeability[4]. Membranes with a sponge-like cross section usually have low permeability but are more pressure resistant due to their dense structure. On the other hand, finger-like membranes have high permeability yet low selectivity with respect to solute rejection due to a wide pore size distribution.

Advancing the field from conventional NIPS membranes, Peinemann *et al.*[5] first reported and demonstrated the fabrication of poly(styrene-*b*-4-vinylpyridine) (PS-*b*-P4VP or SV) diblock copolymer derived asymmetric membranes. Block copolymers are an attractive material for the

fabrication of membranes due to their ability to self-assemble into well-ordered structures. PS-*b*-P4VP derived membranes were generated through a hybrid process of block copolymer self-assembly and NIPS (SNIPS)[6]. Membranes were prepared by 1) dissolving the polymer into an appropriate solvent system, 2) casting a thin film with a doctor blade, 3) solvent evaporation for a specified amount of time to allow block copolymer self assembly, and 4) immersion into a non-solvent (water) bath to induce precipitation of the polymer and kinetically trap the structure in a thermally non-equilibrium state. The resultant membranes were characterized by a disordered graded macroporous substructure beneath an ordered selective skin layer. Since then, Phillip *et al.*[7] applied the hybrid SNIPS process to a triblock terpolymer, poly(isoprene-*b*-styrene-*b*-4-vinylpyridine) (PI-*b*-PS-*b*-P4VP or ISV) because of the inherent mechanical stability associated with the addition of the rubbery PI block. Membranes made from this triblock terpolymer had triple the toughness compared to its diblock counterpart.

The asymmetry of the SNIPS membranes eliminates the trade-off of permselectivity by enabling selectivity, attributed to the isoporous skin layer, and permeability, associated with the macroporous substructure. Numerous studies have been reported on the tunability of the isoporous self-assembled selective layer. Nunes *et al*. studied the effect of different solvent system compositions[8], and metal-complexation[9,10] on their PS-*b*-P4VP system. Pendergast *et al.*[11] investigated various parameters including varying polymer concentration, compositions of volatile to less volatile solvent mixtures, and evaporation times on their ISV polymer system. Dorin *et al.* explored the effect of block copolymer molar mass[12] and the use of small angle x-ray scattering (SAXS)[6] as a screening tool to predict the top surface structure.

In contrast to the past focus on the top separation layer, few studies report on the investigation of parameters controlling the substructure. Current literature details various block

copolymer membrane systems with sponge-like[5,7,12-15], comblike[15] and fingerlike[15,16] morphologies. The current study focuses on the investigation of parameters affecting the substructure to enable its tunability which in turn controls membrane performance (i.e. permeability) without disrupting the self-assembly of the top surface selective layer.

To that end we systematically study several key factors in order to tune the substructure of ISV SNIPS membranes from sponge-like to finger-like. Parameters such as polymer concentration, evaporation time, solvent system, and coagulation bath temperature are shown to affect the substructure morphology. Tunability between sponge-like and finger-like substructures is achieved while preserving the isoporous skin layer responsible for membrane selectively, regardless of substructure morphology. Hydraulic permeability tests at various pH conditions demonstrate the substructure's influence on permeability while leaving pH responsive behavior, associated with the P4VP block[17,18], unperturbed. Additionally, ISV membranes with both types of substructures are integrated onto nylon supports to further improve mechanical stability.

Methods

Polymer synthesis

Four triblock terpolymers, poly(isoprene-*b*-styrene-*b*-4-vinylpyridine) (PI-*b*-PS-*b*-P4VP, ISV) were synthesized via sequential anionic polymerization as previously detailed by Phillip *et al.*[7]. ISV terpolymer characteristics were determined by a combination of gel permeation chromatography (GPC) and ^{1}H NMR. The experimentally determined molar mass (M_n), volume fractions of each block (*f)* and polydispersity index (PDI) of each triblock terpolymer are listed in Table 3.1.

Table 3.1 Summary of ISV terpolymer characteristics.

Polymer	M_n (kg/mol)	f_{PI}	f_{PS}	f_{P4VP}	PDI
ISV115	115	0.26	0.62	0.12	1.16
ISV117	117	0.29	0.59	0.12	1.13
ISV118	118	0.23	0.66	0.11	1.12
ISV139	139	0.26	0.61	0.13	1.16

*Number average molar mass (M_n), volume fraction (*f*) and polydispersity index (PDI).

Membrane fabrication

ISV terpolymers were dissolved in a binary solvent system of 1,4-dioxane (DOX) and tetrahydrofuran (THF) in the appropriate ratios (by weight) and concentrations (see results and discussion section). Utilizing the SNIPS process to prepare membranes, the following steps were taken: 1) the casting solution was pipetted onto a substrate, 2) a thin film was casted with a doctor blade, 3) evaporation of the solvent system for a specified amount of time, and 4) immersion into a coagulation bath. The resultant membranes were dried at ambient conditions before further characterization.

Scanning Electron Microscopy (SEM)

ISV membranes were sputter coated with gold-palladium for 6-7 s prior to SEM imaging using a Denton Vacuum Desk II. SEM micrographs were acquired using a Tescan Mira3 field emission scanning electron microscope (FE-SEM)

Membrane performance tests

For permeability tests and to evaluate the pH-responsive nature of the ISV membranes, neat and supported membrane films were evaluated in a stirred cell (Amicon 8010, Millipore, Co.)

with a volume of 10 mL with an active area of 4.1 cm^2. Three data points were averaged to estimate the permeability under varying pH conditions. pH buffers of sodium acetate and acetic acid were prepared for pH values ranging from 3 to 6. pH buffers of imidazole and hydrochloric acid were prepared for pH values ranging from 7 to 8. The buffer solutions were tested with a pH probe before conducting performance tests.

Viscosity tests

The rheological properties of all solutions were measured by a Discovery Hybrid Rheometer (DHR-3) with a 40 mm 2.0° cone plate configuration at room temperature.

Solubility parameters calculation

Hansen solubility parameters (δ_d, δ_p, δ_h) of water, DOX and THF were obtained from literature[3]. Equation (1) was used to calculate solubility parameters (δ_d, δ_p, δ_h) of solvent mixtures:

$$\delta_{i,S} = \frac{\sum_j (X_j V_j \delta_{i,j})}{\sum_j (X_j V_j)} \quad (1)$$

where X_j, V_j and $\delta_{i,j}$ denote the mole fraction, molar volume and solubility parameter of a specific component j in the mixture, respectively.

The solubility parameter difference ($\delta_{S\text{-}NS}$) between solvent and non-solvent was calculated by

$$\delta_{S-NS} = \sqrt{[(\delta_{d,S} - \delta_{d,NS})^2 + (\delta_{p,S} - \delta_{p,NS})^2 + (\delta_{h,S} - \delta_{h,NS})^2]} \quad (2)$$

Both equations were obtained from the literature[19].

Results and discussion

The formation mechanism of sponge-like and finger-like substructures in NIPS membranes has been extensively studied.[3,19] One dominating theory in the field attributes the different substructures to the demixing rate. In this theory, upon plunging the thin film into a coagulation bath, the casting dope solution separates into two liquid phases, a polymer-rich phase and a polymer-poor phase, designated as liquid-liquid demixing. The substructure's pore sizes are largely determined by this demixing rate. If instantaneous demixing occurs, the polymer-rich phase precipitates quickly to form a solid membrane while the polymer-poor phase converts into large voids, resulting in an open, finger-like cross-sectional morphology. If demixing is delayed, polymer, solvent and non-solvent stay miscible in one phase before phase separation occurs causing a denser sponge-like structure in the final membrane. As the SNIPS process is a combination of self-assembly and NIPS, the formation mechanism of cross-sectional morphology deduced from NIPS membranes should be applicable to SNIPS membranes to tailor sublayer structure.

Among the many variables that influence the demixing rate, we investigated four parameters– casting solution concentration, evaporation time, solvent system, and coagulation bath temperature – to study their effects on the substructure of SNIPS membranes. These parameters are easily adjusted in the membrane fabrication process and include both kinetic and thermodynamic factors that influence the demixing rate.

Concentration and evaporation time dependence

ISV117 was dissolved in a solvent system of DOX/THF = 5/5 with varying polymer concentrations of 9 wt%, 10 wt% and 11 wt%. ISV117 membranes were prepared by the SNIPS

process with evaporation times of 45 s and 60 s. SEM characterizations of ultrafiltration layers and cross sections are presented in Figure 1. With increasing solution concentration at a constant evaporation time (45 s), the membrane cross section transformed from a dominantly finger-like substructure to a half finger-like, half sponge-like substructure. By increasing the evaporation time from 45 s to 60 s, membranes casted with varying concentrations all resulted in dense sponge-like substructures.

The transformation from finger-like to sponge-like morphology at higher concentrations, as well as longer evaporation times, as previously demonstrated, is due to delayed demixing.[20] With increasing concentration or evaporation time, the casting dope solution becomes more viscous before being plunged into the coagulation bath. This rheological hindrance reduces the solvent and non-solvent exchange rate, delaying liquid-liquid demixing, therefore resulting in denser sponge-like substructures.

In addition to the tunable sublayers, SEM images of the top surfaces of all six membranes showed similar mesopores with narrow pore size distributions (inset images in Figure 3.1, Figure S3.1 and S3.2 in supporting information). The ability to maintain the isoporous skin layer while changing the substructure promises high selectivity with tunable permeabilities but also distinguishes the ISV terpolymer system as a robust system for the fabrication of ultrafiltration membranes via SNIPS process.

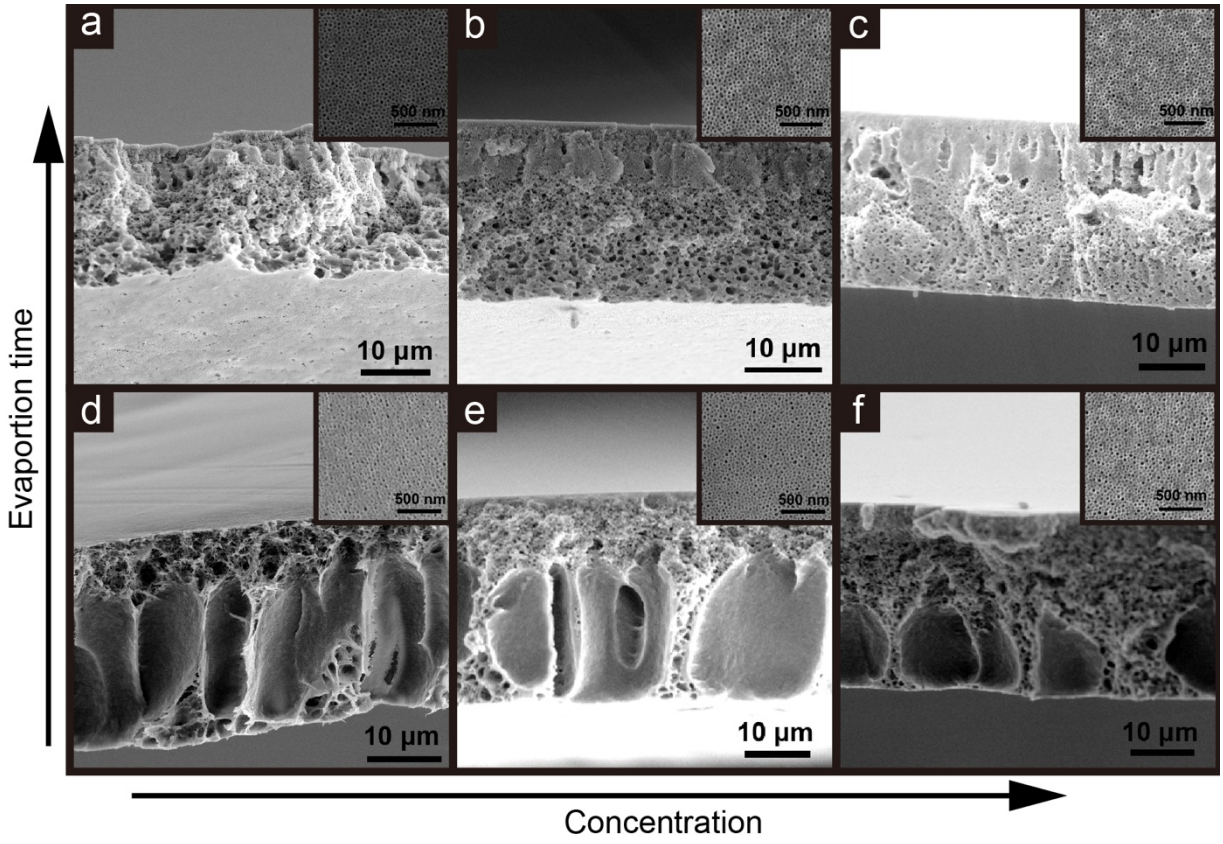

Figure 3.1 Cross-sectional morphology evolution influenced by casting solution concentration and evaporation time. SEM images of cross sections and top surfaces (inset images) of SNIPS membranes cast from (a,d) 9 wt%, (b,e) 10 wt%, and (c,f) 11 wt% ISV117 solutions in DOX/THF = 5/5 at evaporation times of (a-c) 60 s and (d-f) 45 s.

Solvent system dependence

Typically in the SNIPS process, the solvent system used for the casting solution is a mixture of two or more solvent components. At least one solvent is volatile which aids in the formation of an isoporous skin layer derived from block copolymer self-assembly. Specifically for the ISV system, a mixture of DOX and THF are used. By adjusting the solvent ratio in the casting solutions, substructure morphologies can be tuned. ISV139 was dissolved in solvent

systems of DOX/THF in ratios of 5/5, 6/4, and 7/3 at the same polymer concentration (9 wt%). Under the same casting conditions (45 s of evaporation), membranes' cross-sectional structures changed significantly. The membrane casted from DOX/THF = 5/5 system exhibited a hierarchical cross-sectional morphology (Figure 3.2a). Pore sizes gradually increase from the membrane's top to bottom surface. By increasing the DOX/THF ratio to 6/4, a half sponge-like and half-finger-like substructure appeared (Figure 3.2b). In the membrane casted from DOX/THF = 7/3 system, the finger-like morphology ran through almost the entire substructure of the membrane as indicated in Figure 3.2c. The SEM characterization and analysis of the respective isoporous skin layers are shown in Figures S3.3 and S3.4 again demonstrating good control over pore size distribution.

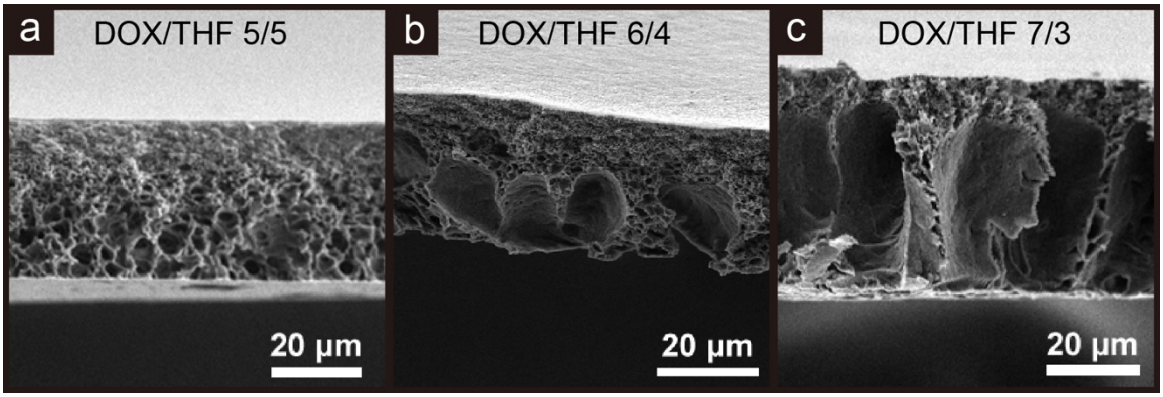

Figure 3.2 Solvent system influence on cross-sectional morphology. SEM images of cross sections of SNIPS membranes cast from 9 wt% ISV139 solutions with (a) DOX/THF = 5/5, (b) DOX/THF = 6/4, and (c) DOX/THF = 7/3 solvent systems at evaporation time of (a-c) 45 s.

To understand the cause of this trend, viscosities of the three casting solutions were analyzed with a rheometer under a series of shear rates. Viscosity data are shown in Figure 3.3. The casting solution containing DOX/THF = 7/3 has the highest viscosity while the casting solution in DOX/THF = 5/5 is the least viscous. As mentioned above, more viscous solutions

usually result in delayed demixing giving denser, sponge-like structures due to rheological hindrance. From the opposite trend seen here, viscosity is not the leading factor in determining substructure morphology in this case.

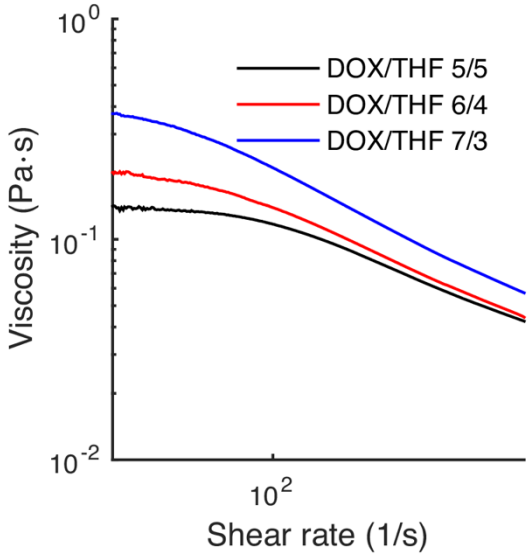

Figure 3.3 Viscosity of ISV139 casting solutions with DOX/THF = 5/5 (black) DOX/THF = 6/4 (red) and DOX/THF = 7/3 (blue) solvent systems.

Solvent - Non-Solvent (S-NS) affinity is another important parameter that determines the demixing rate. Calculation of S-NS affinity is detailed in the Experimental Section. A low solubility parameter difference between S-NS ($\delta_{S\text{-}NS}$) indicates a high S-NS affinity, which favors instantaneous demixing because of the fast solvent - non-solvent exchange. Vandezande *et al.*[19] varied S-NS affinities by several approaches and observed cross section morphology changes. The variation of solvent mixture ratios could also result in different S-NS affinities. Therefore, we calculated $\delta_{S\text{-}NS}$ between water and various solvents including DOX, THF and their mixtures at ratios of 5/5, 6/4, and 7/3 (Table 3.2). The $\delta_{S\text{-}NS}$ values in Table 3.2 indicate that DOX has the highest affinity with water while THF has the lowest. In the mixture systems, $\delta_{S\text{-}NS}$ decreases with

increasing DOX/THF ratio. Accordingly, the affinity between solvent and coagulant has the trend of 7/3 > 6/4 > 5/5. Therefore, DOX/THF = 7/3 system has the highest S-NS exchange rate (i.e. instantaneous demixing) resulting in a more finger-like structure.

Another possible contribution, also studied by Vandezande *et al.*,[19] is the THF ratio in the co-solvent mixture. THF has a lower boiling point as compared to DOX and tends to evaporate faster than DOX. The preferential evaporation of THF creates a concentrated polymer barrier layer which slows down the (S-NS) exchange rate. Hence, with higher THF content (DOX/THF = 5/5), the membrane presents a denser cross-sectional substructure at equivalent evaporation times. To conclude, the observed substructure morphology evolution as a function of DOX/THF solvent ratio most likely is due to a synergistic effect of both S-NS affinity and preferential evaporation of THF.

Table 3.2 Hansen solubility parameters (δ_d, δ_p, δ_h) of solvents and non-solvents and solubility parameter differences ($\delta_{S\text{-}NS}$) between solvent and non-solvent

	δ_d ($MPa^{1/2}$)	δ_p ($MPa^{1/2}$)	δ_h ($MPa^{1/2}$)	$\delta_{S\text{-}NS}$ ($MPa^{1/2}$)
H_2O	15.5	16	42.3	0
DOX	16.8	5.7	8	35.8
THF	19	10.2	3.7	39.2
DOX/THF 7/3	17.5	7.2	6.6	36.9
DOX/THF 6/4	17.8	7.7	6.1	37.2
DOX/THF 5/5	18.0	8.1	5.7	37.5

Coagulation bath temperature dependence

In addition to changing the concentration and evaporation time, coagulation bath temperature can kinetically influence the demixing rate. In Figure 3.4, SNIPS membranes cast from the same solution (7 wt% ISV139, DOX/THF = 5/5) and casting conditions (45 s) were plunged into coagulation baths at room temperature (~20 °C) and at 50 °C. SEM images show a clear transformation from predominant sponge-like to predominant finger-like substructures as coagulation bath temperature increases. SEM characterization of the isoporous skin layers is shown in Figure S3.5. Previously, this behavior was also reported and explained in NIPS membrane systems.[21] At high coagulation bath temperatures, the system kinetically favors instantaneous demixing which results in larger pore sizes and, in our case, the finger-like substructure.

Obvious transformations between sponge-like and finger-like substructures are only observed under certain casting conditions. Although, as shown in Figure S3.6, cross-sectional morphologies transformed to larger pore sizes with increasing bath temperature, this temperature increase cannot completely overcome the rheological hindrance due to the high concentration (9 wt%) and long evaporation time (55 s), and as a result, did not fully convert the membrane to a finger-like substructure.

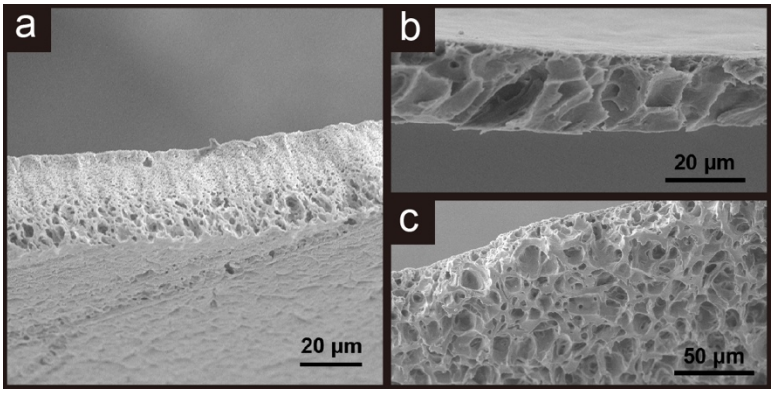

Figure 3.4. SEM images of cross sections and bottom layer of SNIPS membranes cast from 7 wt% ISV 139 solutions in DOX/THF = 5/5 at an evaporation time of 45 s and immersed in a water coagulation bath at (a) room temperature resulting in a dense sponge-like substructure, and (b,c) 50°C resulting in an open finger-like cross section.

Membranes atop nylon support

For final use of block copolymer derived SNIPS membranes it is desirable to cast the material on supports that provide additional mechanical stability during handling and use. In the last part of this study we therefore wanted to find out whether control over sponge-like and finger-like substructures could be preserved when casting was performed in the presence of a support structure and finally how the support would influence permeability of the final assembly. To this end ISV115 and ISV118 polymer casting solutions were prepared by dissolving ISV terpolymer into a binary solvent system of DOX and THF in a 7/3 ratio (by weight). Neat and supported ISV115 membranes were cast from a 11 wt% polymer solution with an evaporation time of 30 s. Neat and supported ISV118 membranes were cast from a 11 wt% polymer solution with an evaporation time of 30s. A lower concentration neat ISV118 membrane was cast from a 9 wt% polymer solution and an evaporation time of 45s. Casting solutions were pipetted onto glass substrates to generate neat, unsupported membranes. For supported membranes, casting solutions were pipetted directly onto 0.1 or 0.2 μm nylon substrates (Sterlitech, Inc.) as it eliminates additional fabrication steps and is therefore preferred. The casting solutions were casted using a doctor blade with a height between 0.203 and 0.229 mm. The neat and supported thin films were allowed to evaporate for specified times before immersion into a coagulation bath.

The optimized casting conditions chosen for ISV115 and ISV118 membrane fabrication were based on polymer concentration, solvent ratio, and evaporation time parameters that yielded a uniform and porous top surface above the desired sponge-like or finger-like macroporous substructure. Molar mass of the ISV terpolymers is another parameter that controls substructure. An additional parameter, viscosity, was taken into consideration for the fabrication of supported ISV118 membranes as the increased viscosity of the casting solution impeded its infiltration through the nylon substrate while allowing the membrane to remain atop the nylon substrate.

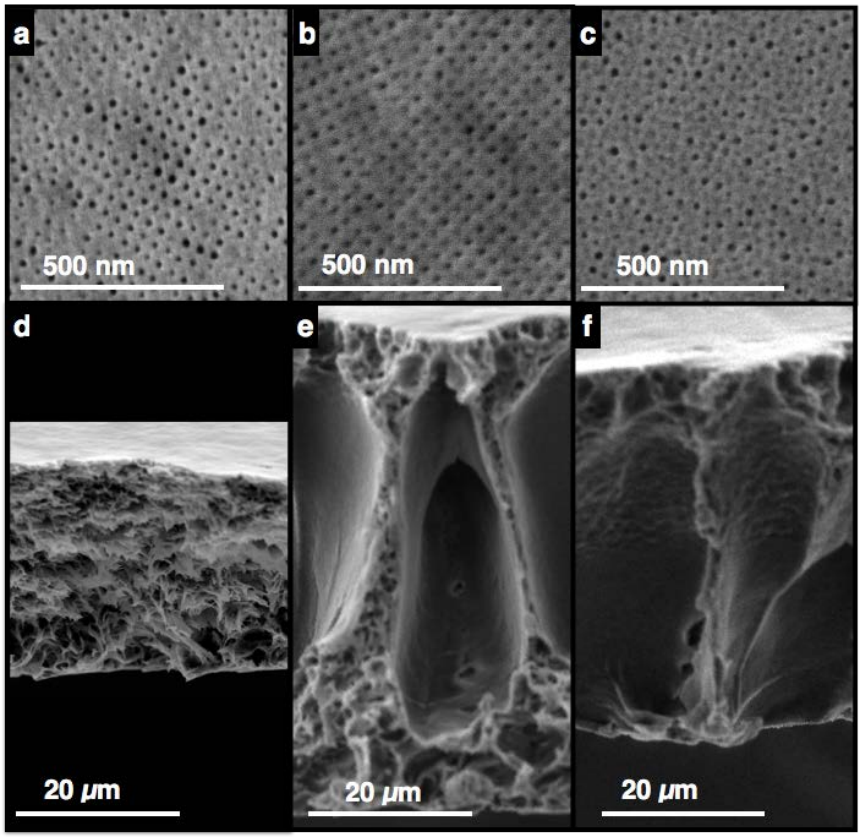

Figure 3.5 SEM micrographs of top surfaces (top row) and cross sections (bottom row) of neat SNIPS membranes cast from (a,d) 11 wt% ISV115 at evaporation time of 30 s, membrane thickness t = ~26 μm; (b,e) 11 wt% ISV118 at evaporation time of 30 s, t = ~55 μm; and (c,f) 9 wt% ISV118 at evaporation time of 45s, t = ~48 μm. In all cases DOX/THF = 7/3 was used as solvent system.

Furthermore, the trends discussed using results shown in Figure 3.1 for the ISV117 terpolymer are applicable to terpolymer ISV118. For example, the membrane derived from 9 wt% ISV118 with 45 s evaporation time has a finger-like substructure. By increasing the concentration (i.e. moving to 11 wt%) but lowering the evaporation time to 30s, the cross-sectional morphology stays finger-like, see Figure 3.5. Moreover, increasing the evaporation time to 45s for 11 wt% ISV118 leads to a transition to a sponge-like morphology (see supporting information, Figure S7), also in good agreement with results from Figure 1. While those trends are applicable over a range of polymers, exact parameters, in particular the evaporation time, may be different for each specific terpolymer in order to tune for optimal finger-like versus sponge-like substructures as well as surface structure.

Casting under the aforementioned conditions for neat ISV115 and ISV118 resulted in ordered, isoporous membranes with a sponge-like and finger-like substructure, respectively, see SEM micrographs of top surfaces and cross sections depicted in Figure 5. Supported membranes were then fabricated by directly casting the ISV115 and ISV118 (both 11 wt%) thin films onto porous, nylon substrates. Figure 3.6a,d depicts the top surface and cross sectional image of a 0.2 μm nylon substrate with an internally inert polyester support. As demonstrated in Figure 3.6, the top surface, characterized by uniform pores and the respective sponge-like or finger-like cross sections were retained atop the nylon substrates. This demonstrates that membranes characterized by sponge-like and finger-like substructures can both be integrated with a support layer.

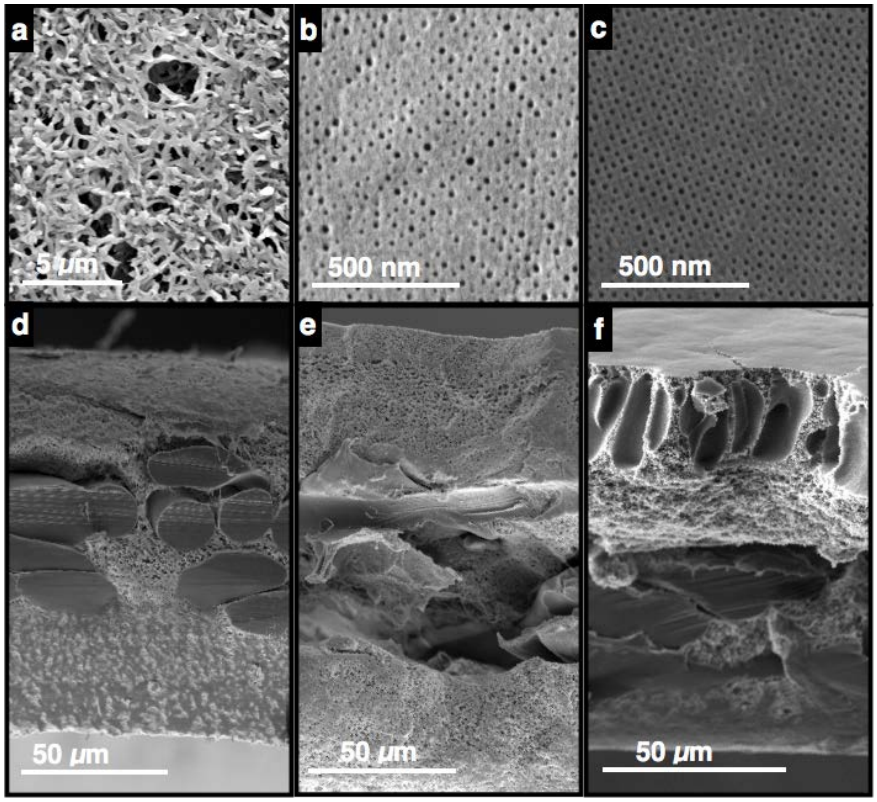

Figure 3.6 Membranes casted on nylon supports. SEM micrographs of top surfaces (top row) and cross sections (bottom row) of (a,d) 0.2 µm nylon support and SNIPS membranes cast from solutions in DOX/THF = 7/3 at evaporation time of 30s and concentrations of: (b, e) 11 wt% ISV115 on 0.2 µm nylon, and (c, f) 11 wt% ISV118 on 0.1 µm nylon. 0.1 and 0.2 µm nylon differ by average pore sizes and permeabilities (see supporting information, Figure S3.8 and S3.9).

Due to the pH-responsive nature of the P4VP block membrane performance was characterized by measuring the permeability at varying pH conditions[7,9,10,14]. Permeability measurements were taken with a stirred cell on membranes with an applied N_2 gas pressure of 1-2 psi. Membrane compression is observed at higher pressures, with sponge-like substructures more pressure resistant than finger-like substructures (see supporting information Figure S3.10). From the results shown in Figure 3.7, it can be concluded that the pH-responsive nature of the ISV membranes adhered to a nylon support was preserved.

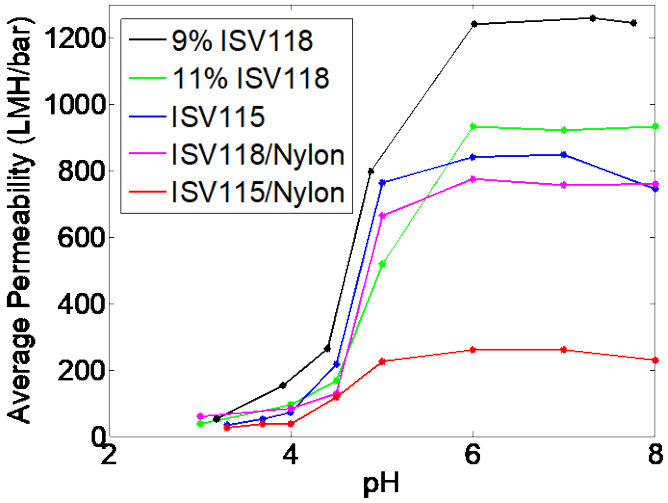

Figure 3.7 Performance of neat and supported ISV115 and ISV118 membranes under varying pH conditions.

As expected, in general membranes with a finger-like substructure have enhanced permeability as compared to membranes with sponge-like substructures. The difference in flux of neat membranes, see corresponding SEM micrographs in Figure 3.5 and permeabilities in Figure 3.7, is attributed to thickness and substructure differences. The 11 wt% ISV118 membrane is ~10 μm thicker than a membrane from 9 wt% ISV118 resulting in lower permeability due to a longer path. The 11 wt% ISV115 (sponge-like) membrane has lower permeability relative to a membrane from 11 wt% ISV118 since sponge-like substructures (ISV115) provide more resistance to flow than finger-like channels (ISV118). However, it is important to look at the structural details of block copolymer derived SNIPS membranes casted on supports in order to fully understand the observed behavior. For example, adhering a ISV115 membrane with a sponge-like substructure to a nylon support resulted in a permeability reduction by a factor of 3.3 at neutral pH conditions. When analyzing SEMs of the cross-sectional structure of this membrane we observed the formation of a dense layer at the interface of the membrane and nylon support (see supporting information, Figures S3.11 and S3.12) not observed for the unsupported membrane and most

likely responsible for this large permeability reduction. A smaller permeability reduction factor of 1.7 at similar pH conditions was found for supported finger-like ISV118 membranes. Despite the complexities of the SNIPS membrane system which are due to the multitude of parameters associated with the SNIPS process, these results suggest tunability of membrane performance as a consequence of specifics of the substructure even in the case that membrane supports are used during membrane fabrication.

Conclusion

In this work, we systematically demonstrated methods to tune the substructure of SNIPS membranes between sponge-like and finger-like morphologies while simultaneously leaving the self-assembled and ordered top surface layer intact. The mechanism of substructure formation was shown to be determined by the demixing rate, which was influenced by kinetic parameters such as concentration, evaporation time, and coagulation bath temperature, as well as by thermodynamic parameters including solvent and non-solvent (S-NS) affinity. Asymmetric ISV membranes integrated with a porous nylon support for improved mechanical stability maintained isoporous ultrafiltration surface layers and simultaneously allowed control over sponge-like and finger-like substructures. Results suggest high tunability and robustness of asymmetric membrane structure for the ISV triblock terpolymer system which should enable fine tuning of structure to simultaneously maximize membrane selectivity and permeability.

Acknowledgments

The authors would like to acknowledge funding of this work by the Defense Threat Reduction Agency (DTRA) Contract No. HDTRA1-13-C0003. Y.G. was funded by the National

Science Foundation (DMR-1409105). This work utilized the Cornell Center for Materials Research (CCMR) facilities supported by NSF MRSEC program (DMR-1120296).

REFERENCES

1. D. A. Bernards, T. A. Desai, Nanoscale porosity in polymer films: fabrication and therapeutic applications, Soft Matter 6 (2010) 1621-1631.

2. Q. Z. Zheng, P. Wang, Y. N. Yang, Rheological and thermodynamic variation in polysulfone solution by PEG introduction and its effect on kinetics of membrane formation via phase-inversion process, J. Membr. Sci. 279 (2006) 230-237.

3. G. R. Guillen, Y. Pan, M. Li, E. M. Hoek, Preparation and characterization of membranes formed by nonsolvent induced phase separation: a review, Ind. Eng. Chem. Res. 50 (2011) 3798-3817.

4. J. R. Werber, C. O. Osuji, M. Elimelech, Materials for next-generation desalination and water purification membranes, Nat. Rev. Mater. (2016) 16018.

5. K.V. Peinemann, V. Abetz, P.F.W. Simon, Asymmetric superstructure formed in a block copolymer via phase separation, Nat. Mater. 6 (2007) 992-996.

6. R. M. Dorin, D. S. Marques, H. Sai, U. Vainio, W. A. Phillip, K. V. Peinemann, S.P. Nunes, U. Wiesner, Solution small-angle X-ray scattering as a screening and predictive tool in the fabrication of asymmetric block copolymer membranes, ACS Macro Lett. 1 (2012) 614-617.

7. W.A. Phillip, R.M. Dorin, J. Werner, E.M.V. Hoek, U. Wiesner, M. Elimelech, Tuning Structure and Properties of Graded Triblock Terpolymer-Based Mesoporous and Hybrid Films, Nano Lett. 11 (2011) 2892-2900.

8. S. P. Nunes, M. Karunakaran, N. Pradeep, A. R. Behzad, B. Hooghan, R. Sougrat, H. He, K. V. Peinemann, From micelle supramolecular assemblies in selective solvents to isoporous membranes, Langmuir 27 (2011) 10184-10190.

9. S. P. Nunes, A. R. Behzad, B. Hooghan, R. Sougrat, M. Karunakaran, N. Pradeep, U. Vainio, K. V. Peinemann, Switchable pH-responsive polymeric membranes prepared via block copolymer micelle assembly, Acs Nano 5 (2011) 3516-3522.

10. S. P. Nunes, R. Sougrat, B. Hooghan, D. H. Anjum, A. R. Behzad, L. Zhao, N. Pradeep, I. Pinnau, U. Vainio, K. V. Peinemann, Ultraporous films with uniform nanochannels by block copolymer micelles assembly, Macromolecules 43(2010) 8079-8085.

11. M.M. Pendergast, R.M. Dorin, W.A. Phillip, U. Wiesner, E.M.V. Hoek, Understanding the structure and performance of self-assembled triblock terpolymer membranes, J. Membr. Sci. 444 (2013) 461-468.

12. R.M. Dorin, W.A. Phillip, H. Sai, J. Werner, M. Elimelech, U. Wiesner, Designing block copolymer architectures for targeted membrane performance, Polymer 55 (2014) 347-353.

13. J. Hahn, V. Filiz, S. Rangou, J. Clodt, A. Jung, K. Buhr, C. Abetz, V. Abetz, Structure formation of integral-asymmetric membranes of polystyrene-block-Poly (ethylene oxide), J. Polym. Sci., Part B: Polym. Phys. 51 (2013) 281-290.

14. Y. Gu, U.Wiesner, Tailoring Pore Size of Graded Mesoporous Block Copolymer Membranes: Moving from Ultrafiltration toward Nanofiltration, Macromolecules 48 (2015) 6153-6159.

15. F. Schacher, T. Rudolph, F. Wieberger, M. Ulbricht, A. H. Muller, Double stimuli-responsive ultrafiltration membranes from polystyrene-block-poly (N, N-dimethylaminoethyl methacrylate) diblock copolymers, ACS Appl. Mater. Interfaces 1(2009) 1492-1503.

16. Y. Gu, R. M. Dorin, U. Wiesner, Asymmetric organic–inorganic hybrid membrane formation via block copolymer–nanoparticle co-assembly, Nano lett. 13 (2013) 5323-5328.

17. A. M. Mika, R. F. Childs, J. M. Dickson, Chemical valves based on poly (4-vinylpyridine)-filled microporous membranes, J. Membr. Sci. 153 (1999) 45-56.

18. M. Tagliazucchi, O. Azzaroni, I. Szleifer, Responsive polymers end-tethered in solid-state nanochannels: when nanoconfinement really matters, J. Am. Chem. Soc. 132 (2010) 12404-12411.

19. P. Vandezande, X. Li, L. E. Gevers, I. F. Vankelecom, High throughput study of phase inversion parameters for polyimide-based SRNF membranes, J. Membr. Sci. 330 (2009) 307-318.

20. A. K. Hołda, B. Aernouts, W. Saeys, I. F. Vankelecom, Study of polymer concentration and evaporation time as phase inversion parameters for polysulfone-based SRNF membranes. J. Membr. Sci. 442 (2013) 196-205.

21. Q. Z. Zheng, P. Wang, Y. N. Yang, D. J. Cui, The relationship between porosity and kinetics parameter of membrane formation in PSF ultrafiltration membrane, J. Membr. Sci. 286 (2006) 7-11.

APPENDIX B

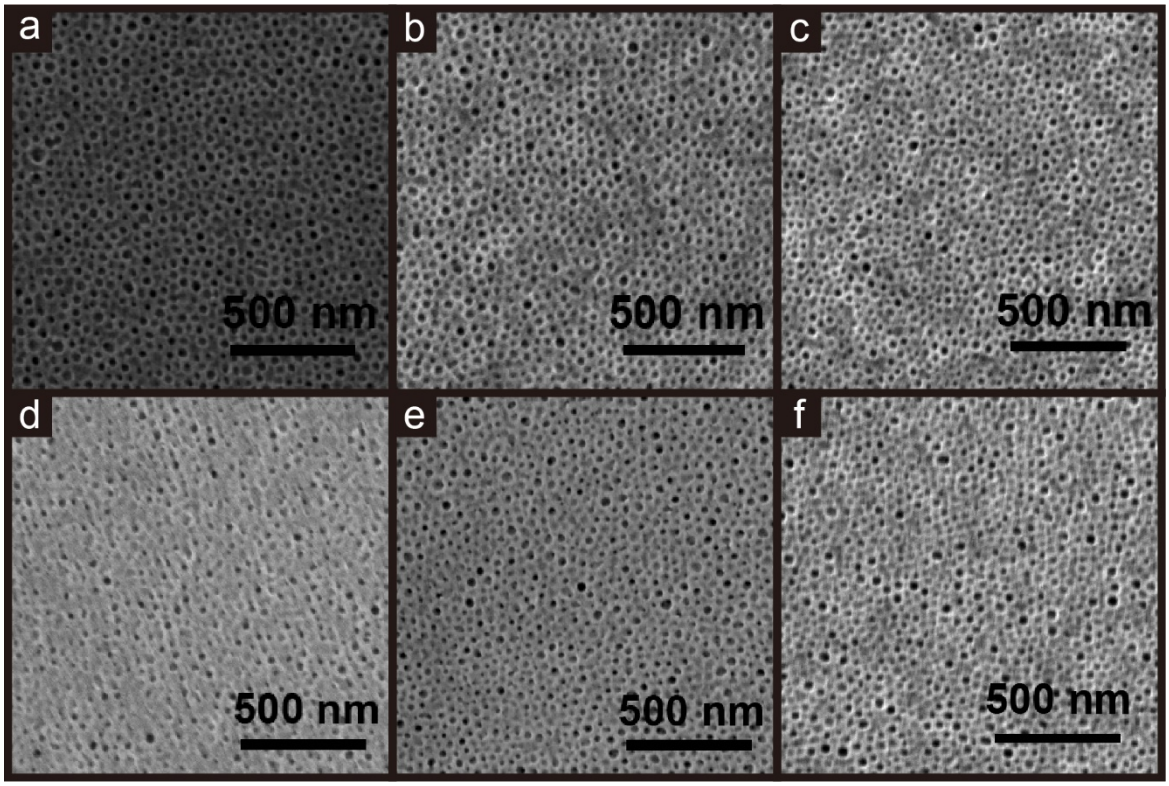

Figure S3.1 SEMs of the top surface layers of membranes discussed in Figure 1. Membranes are cast from (a,d) 9 wt%, (b,e) 10 wt%, and (c,f) 11 wt% ISV117 solutions in DOX/THF=5/5 at evaporation times of (a-c) 60 s and (d-f) 45 s.

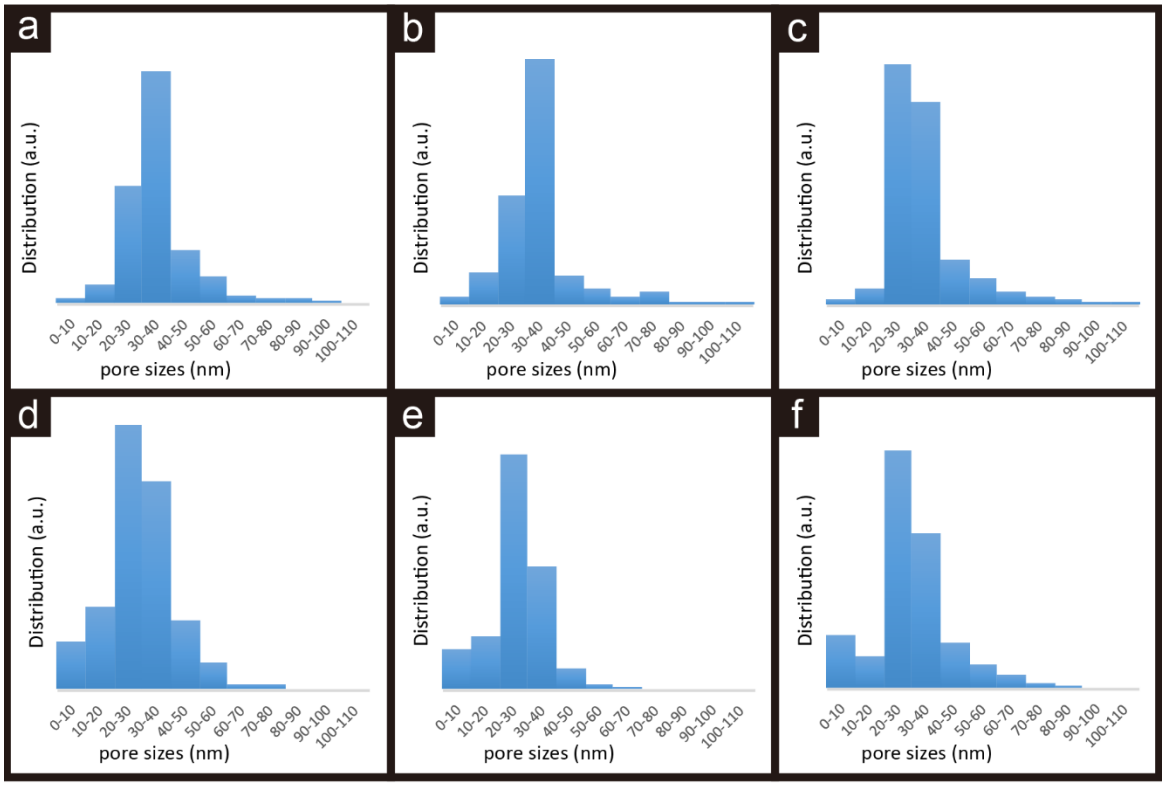

Figure S3.2 ImageJ analyses of pore size distributions of surface layers corresponding to SEMs shown in Figure S3.1.

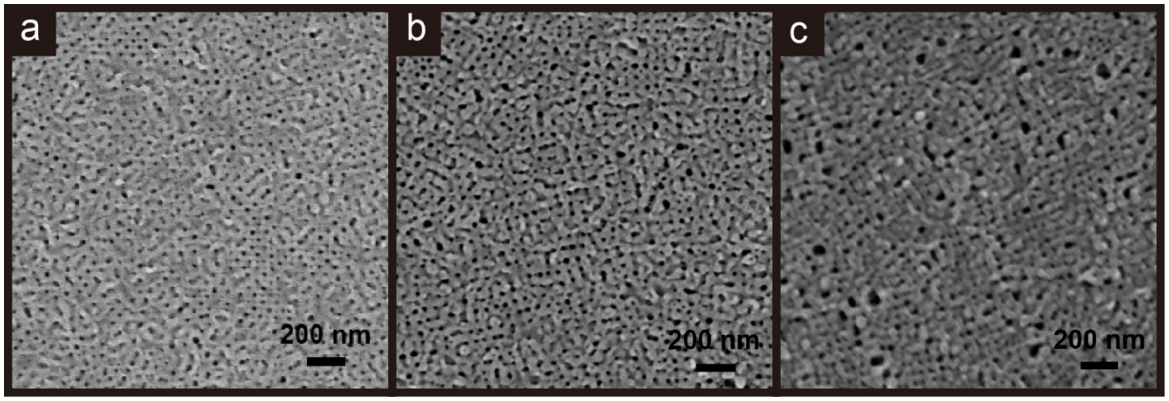

Figure S3.3 SEM images of top surface of SNIPS membranes cast from 9 wt% ISV139 solutions with (a) DOX/THF=5/5 (b) DOX/THF=6/4 and (c) DOX/THF=7/3 solvent systems at evaporation time of 45 s.

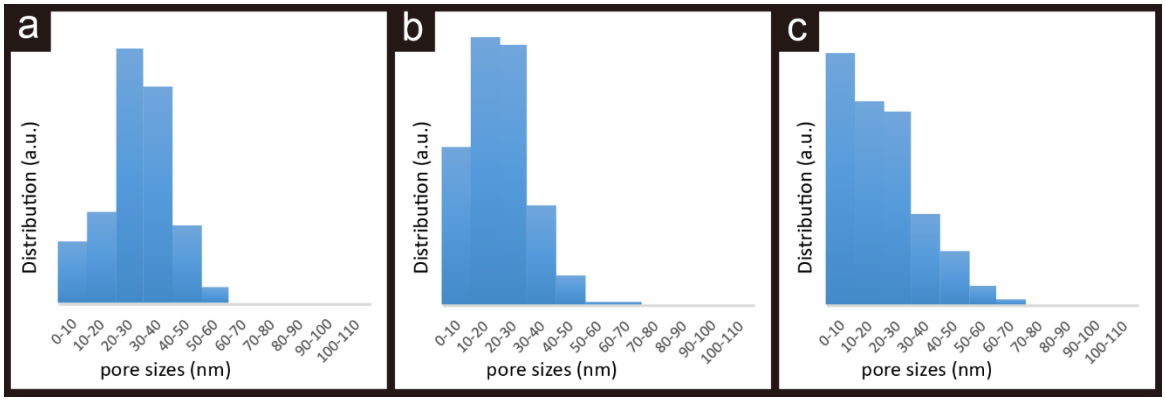

Figure S3.4 ImageJ analyses of the pore size distributions of surface layers corresponding to SEMs shown in Figure S3.

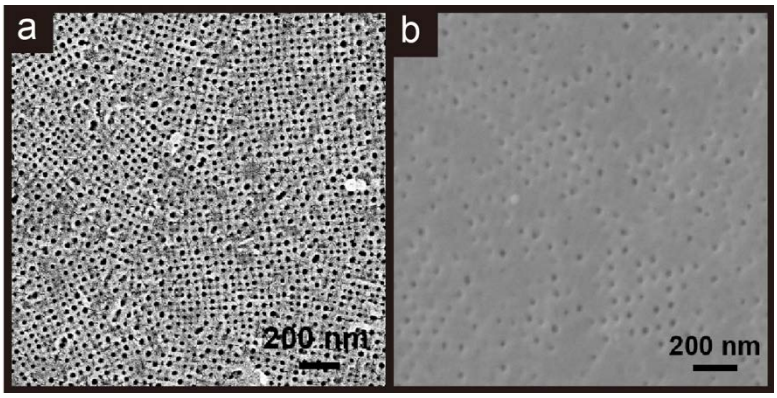

Figure S3.5 SEM images of top surfaces of SNIPS membranes cast from 7 wt% ISV139 solutions in DOX/THF=5/5 at an evaporation time of 45 s and immersed in (a) room temperature and (b) 50°C coagulation baths.

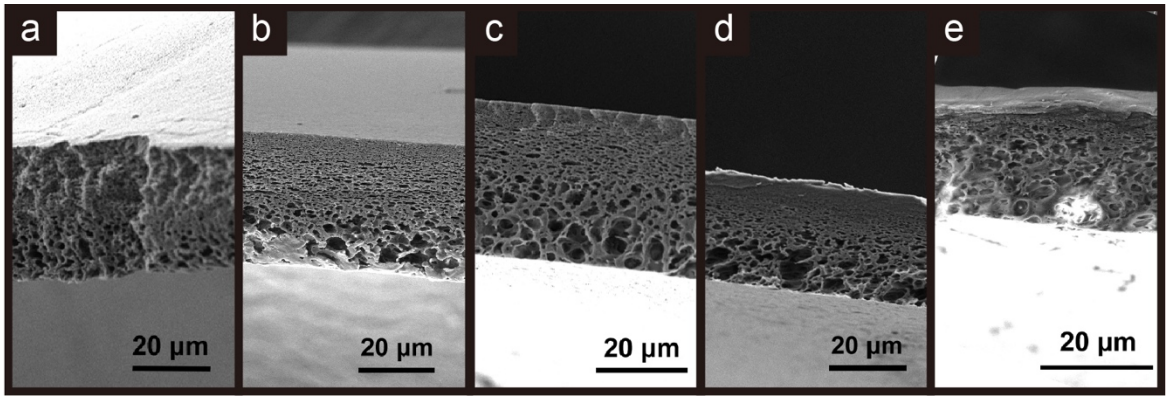

Figure S3.6 SEM images of cross sections of SNIPS membranes cast from 9 wt% ISV139 solutions in DOX/THF=5/5, evaporation time of 55 s, and immersed into coagulation baths held at (a) 8 °C (b) 20 °C (c) 30 °C (d) 40 °C and (e) 50 °C.

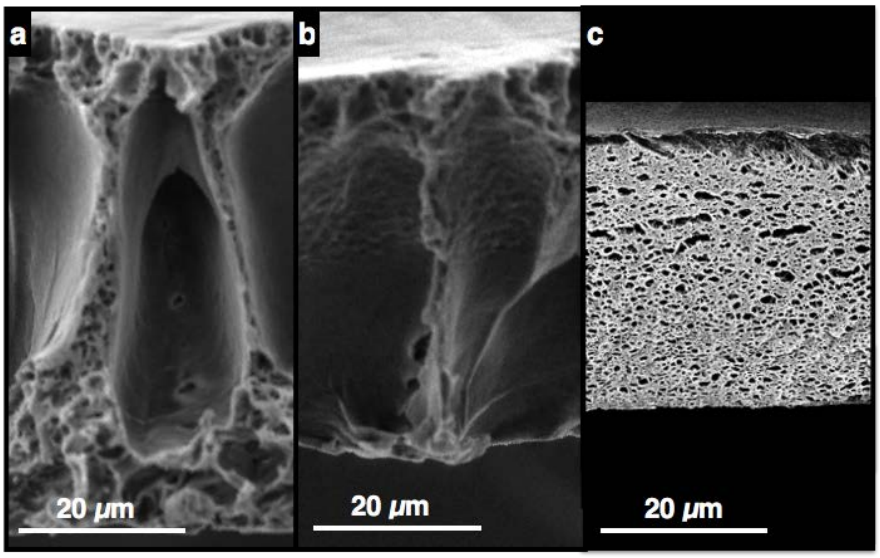

Figure S3.7 Evolution of cross-sectional morphology from finger-like to sponge-like substructures for ISV118 terpolymer through variation of polymer concentration and evaporation time. (a) 11 wt% ISV118; 30s; (b) 9 wt% ISV118; 45s; (c) 11 wt% ISV118; 45s. All membranes were derived from DOX/THF=7/3 solutions.

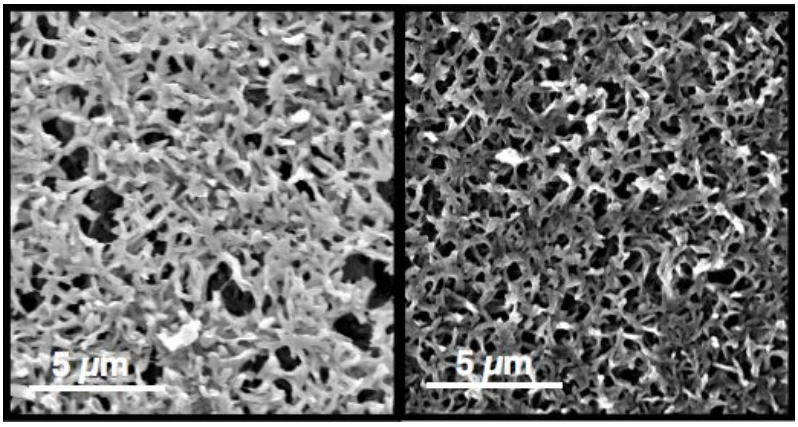

Figure S3.8 SEM images of nylon support top surfaces with average pore sizes of 0.1 (right) and 0.2 (left) μm.

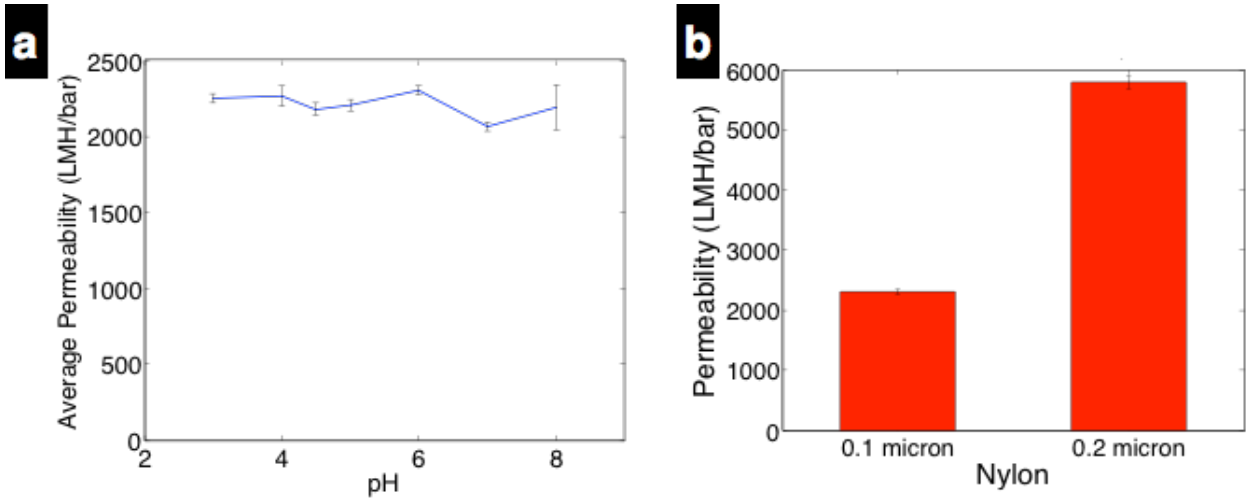

Figure S3.9 (a) pH-dependent permeability of 0.1 μm support. (b) Permeability of 0.1 μm and 0.2 μm nylon supports at pH=6.

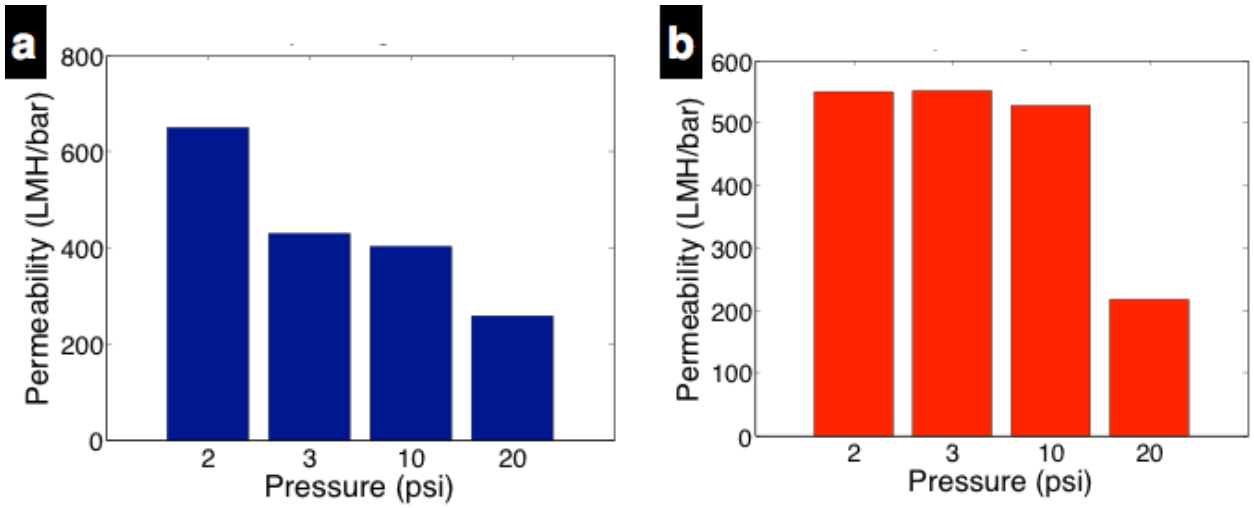

Figure S3.10 Pressure dependent hydraulic permeability of neat membranes cast from 11 wt% (a) ISV118 (finger-like) and (b) ISV115 (sponge-like) solutions in DOX/THF=7/3 for evaporation times of 30 s.

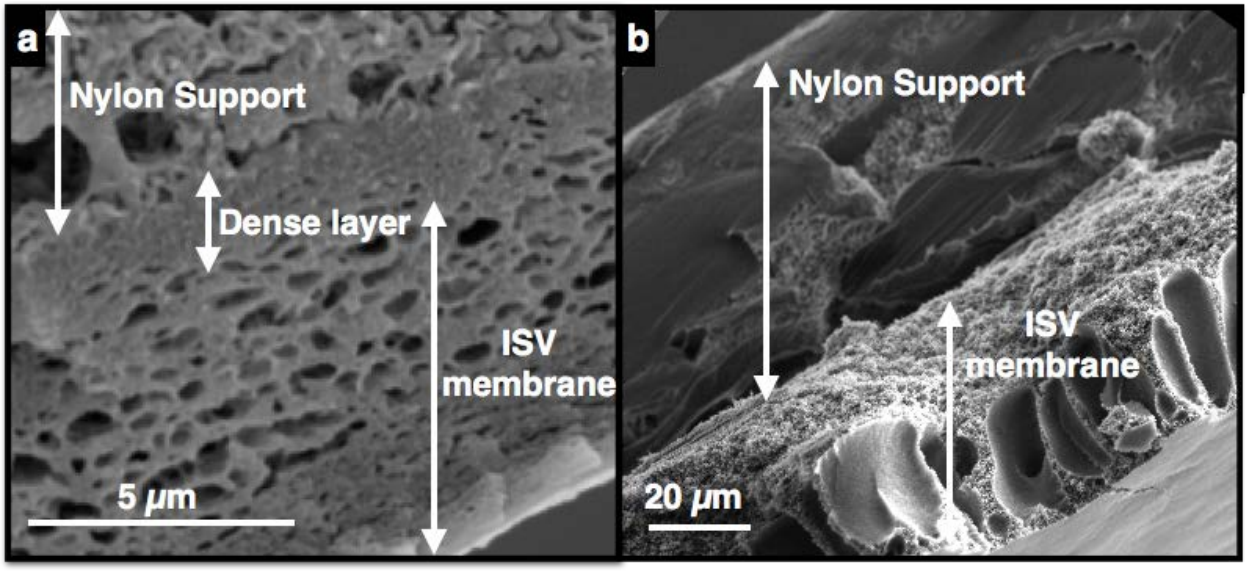

Figure S3.11 Comparison of interfacial layer of supported membranes. (a) Supported ISV115 membrane exhibits a reduction in permeability by a factor of 3.3 due to the formation of a dense layer at the interface of membrane and nylon support. No such dense layer is observed at the interface for (b) supported ISV118 membrane. Casting conditions for both membranes were 11 wt% terpolymer solutions in DOX/THF=7/3 and an evaporation time of 30 s.

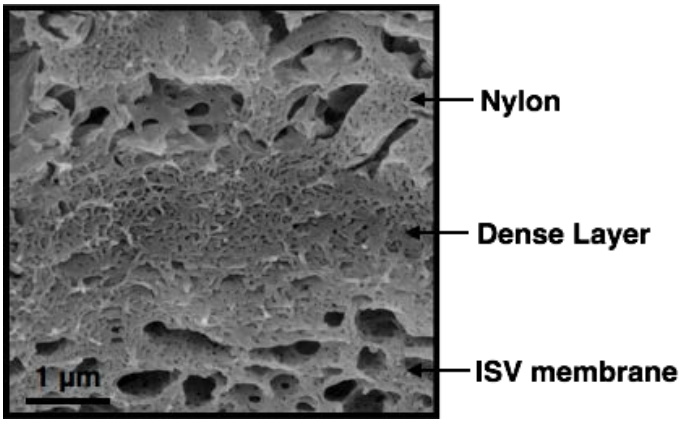

Figure S3.12 SEM micrograph zooming in to the interface layer shown at lower magnification in Figure S3.11a evidencing ISV polymer infiltrating the nylon support reflecting good adhesion between ISV membrane and support.

CHAPTER 4

EFFECT OF HUMIDITY ON SURFACE STRUCTURE AND PERMEATION OF TRIBLOCK TERPOLYMER DRIVED SNIPS MEMBRANES*

Abstract

Block copolymer (BCP) ultrafiltration (UF) membranes derived from a hybrid process of BCP self-assembly and non-solvent induced phase separation (SNIPS) exhibit an asymmetric structure consisting of ordered pores in a selective skin layer above a highly permeable substructure. In this work, we investigate relative humidity (RH) as a casting condition that influences poly(isoprene-*b*-styrene-*b*-4-vinylpyridine) (ISV) membrane surface structure in terms of order and uniformity. An optimum RH of 40-45% is determined to produce membranes characterized by a high density of square packed pores with a narrow pore size distribution. Membranes casted at lower and higher RH show a drop off in order and uniformity. The RH dependent structural changes correlate well with small molar mass dye solute (methyl orange; molar mass of 327 g/mol) diffusion rates: Membranes casted at 40% RH reveal higher diffusivity than when casted at 75% RH. The rate of permeation is further controlled via pH dependent pore closure as well as through ISV terpolymer molecular architecture with increasing solute diffusivity observed in membranes casted from increasing terpolymer molar mass. Experimental findings on small molar mass solute permeability can only be accounted for when compared with theoretical predictions from a hydrodynamic theory combined with the effects of tortuosity when a simplified membrane structure is assumed. Results suggest that SNIPS derived BCP membranes may have potential for applications in drug delivery.

[*] Reprinted (adapted) with permission from Y. M. Li, Q. Zhang, J. R. Álvarez-Palacio, I. F. Hakem, Y. Gu, M. R. Bockstaller, U. Wiesner, Effect of humidity on surface structure and permeation of triblock terpolymer derived SNIPS membranes, *Polymer* **126**, 368-375 (2017). Copyright Elsevier.

Introduction

Polymeric membranes fabricated via block copolymer (BCP) self-assembly plus non-solvent induced phase separation (SNIPS)[1] process rise as strong candidates for next generation asymmetric ultrafiltration (UF) membranes due to their advantageous combination of uniform pore size and high pore density. The highly ordered mesoporous surface with narrow pore size distribution promises high resolution while the high pore density together with the macroporous substructure gives rise to high permeability. Since the first publication on SNIPS membranes derived from BCP poly(styrene-*b*-4-vinylpyridine) (SV) in 2007[2], the SNIPS process has been studied extensively for various BCPs over the past decade.

A primary focus in the emerging SNIPS derived BCP membrane field to date has been the exploration of membrane properties through molecular design. Functionalizing membranes through molecular architecture rather than process control is a paradigm shift in the membrane field and promises substantial expansion of membrane capabilities. For example, BCP membranes containing a poly(4-vinylpyridine) (P4VP) or poly(acrylic acid) (PAA) block are pH-responsive[2-4] resulting in changes in effective pore size upon pH variations. Mechanical properties like membrane toughness can be largely enhanced through the addition of a rubbery polyisoprene block to the high glass transition (T_g) matrix block of BCP UF membranes.[3] For foreign molecule attachment, membranes can be designed with covalent binding sites by e.g. adding a functional group at the hydrophilic chain end decorating the pore walls allowing for thiol-ene click chemistry based post-fabrication steps.[5] Lastly, the blending of two (or more) BCPs into the casting dope enables a novel “mixing and matching” approach to e.g. tailoring of membrane surface chemistry from different polymers.[6]

Another main focus of SNIPS membrane studies has been the structure control of the selective top separation layer. Although first systematic studies regarding control of SNIPS membrane substructure are emerging,[7] the overwhelming majority of reports has the regularly patterned, self-assembled mesopores at the top surface at the center of attention. For a number of BCP systems casting conditions have been tested to achieve a regularly patterned surface structure including casting dope composition, evaporation time and coagulation bath conditions.[8-10] Other studies have focused on the tuning of pore size, by varying BCP molar mass or through the incorporation of additives.[9,11] Finally, several studies elucidate the formation mechanisms of these well-organized selective layers.[3,12-15] Most recently, *in-situ* grazing incidence small angle x-ray scattering (GISAXS) has been employed to better understand the structure evolution during organic solvent evaporation steps,[16-18] revealing structural phase transitions in the top separation layer.[17]

Despite numerous studies of parameters affecting SNIPS membrane structure and membrane formation mechanisms, systematic investigations of the relationship between surface structure and membrane performance as well as comparisons and benchmarking with existing UF membranes in terms of achievable resolution are still limited. In previous work, polyethylene oxide (PEO) or protein rejection and flux tests have been used to characterize membrane performance. Rejection tests have mainly been employed for pore size characterization via molecular weight cut off (MWCO) curves[3] while permeability has been assessed via flux tests. To move the use of SNIPS membranes beyond conventional separation applications and towards protein or drug delivery vehicles, and inspired by studies of single file diffusion through nanochannels for protein delivery applications,[19] it is interesting to characterize the diffusion of small molar mass solutes through asymmetric SNIPS membranes as a function of membrane

structure. To that end, in the present study we first investigated the effects of relative humidity (RH) on surface structure of SNIPS derived UF membranes from poly(isoprene-*b*-styrene-*b*-4-vinylpyridine) (PI-*b*-PS-*b*-P4VP, ISV) and subsequently correlated the observed structural changes with the permeation of a model dye solute through the BCP membranes thereby identifying parameters that tailor the rate of diffusion.

To the best of our knowledge, this is the first report on the influence of RH on the top surface structure of SNIPS derived UF membranes. Results demonstrate that ISV based membrane top surface structure is sensitive to RH and reaches an optimum at mid-range RH around 40-45%, while higher or lower humidity disturbs the surface structure. Interestingly, it is observed that higher casting solution concentrations render the membranes less sensitive to RH changes. Top surface structural changes directly correlate with model small molar mass dye solute permeation rates, with membranes casted at optimum mid-range RH possessing higher diffusivities. Additional control over the rate of small model solute diffusion is achieved through parent terpolymer molar mass as evidenced by membranes fabricated under RH conditions providing optimized surface structures. Finally, measured membrane permeability is compared to theoretical predictions to account for the experimental observations.

Methods

Polymer synthesis

Three ISV triblock terpolymers were synthesized via sequential anionic polymerization as previously described [8]. The polymers were characterized by gel permeation chromatography (GPC) and ^{1}H NMR for molar mass (M_n), volume fractions of each block (*f*), and polydispersity

index (PDI). A summary of characterization results for each ISV triblock terpolymer used in this study is provided in Table 4.1.

Table 4.1 Summary of ISV terpolymer characteristics.

Polymer	M_n **(kg/mol)**	f_{PI}	f_{PS}	f_{P4VP}	**PDI**
ISV43	43	0.24	0.56	0.20	1.02
ISV99	99	0.23	0.63	0.14	1.20
ISV119	119	0.19	0.65	0.16	1.17

*Number average molar mass (M_n), volume fraction (f), and polydispersity index (PDI).

Membrane Fabrication

ISV terpolymers were dissolved in a binary solvent system of 1,4-dioxane (DOX) and tetrahydrofuran (THF) in a 7/3 weight ratio and appropriate concentrations (see results and discussion section). The SNIPS process was conducted inside a drybox following these steps: 1) the casting solution was pipetted onto a substrate (glass or nylon support); 2) a thin film was casted with a doctor blade at a gate height of 220 μm; 3) solvent evaporated for a specified amount of time, and 4) the film was immersed into a water coagulation bath. Levels of RH inside the drybox were controlled by either introducing a hot water bath or sparging with dry N_2 to increase or decrease RH, respectively. A humidity meter (Model: VWR-61161-378) was used to monitor RH during casting. Levels of RH were adjusted before casting. The stream of dry N_2 was stopped

before the start of the casting process to prevent air disturbances during the evaporation step. Humidity fluctuations during the evaporation step were within +/- 2% RH.

Scanning Electron Microscopy (SEM)

Scanning electron microscopy (SEM) images of membranes were acquired on a Tescan LM Mira3 FE-SEM with an in-lens detector. Pore Size distributions and Fast Fourier transform (FFT) analyses of the top surfaces were performed via ImageJ with the Radial Profile Extended plugin (Philippe Carl). For comparison, the pore size data was fitted with both a normal Gaussian distribution and a log-normal distribution using Matlab's fitting tool with the bin width set to 1.

Membrane Permeation Studies

The permeation of a model dye solute, methyl orange, through the series of ISV based triblock terpolymer membranes was evaluated in a side-by-side diffusion cell (PermeGear). The setup (Figure 4.1) consisted of two chambers, the donor (right chamber) and receptor (left chamber) cell, with a volume of 3 mL each and containing a magnetic stirrer. The terpolymer membrane was placed between the two chambers with the selective surface layer facing the donor cell. The setup was sealed by clamping the cells tightly together and placed on a stir plate with a continuous stir rate of 200 rpm. The donor cell was filled with 3 mL of a methyl orange solution (1.0 mg methyl orange per mL buffer solution of the respective pH) while the receptor cell was filled with the same volume of the respective buffer solution. For membrane "closed state" studies, pH=4 buffer solutions were prepared with sodium acetate and acetic acid. For membrane "open state" studies, pH=7 buffer solutions were prepared with imidazole and hydrochloric acid. 0.1M

buffer solutions were tested with a pH probe before conducting experiments. Receptor cell aliquots (300 μL) were taken every 20 minutes for three hours for "open state" experiments and every 20 minutes for four hours for "closed state" experiments. Receptor cell aliquots were replaced with the same volume of the corresponding buffer solution.

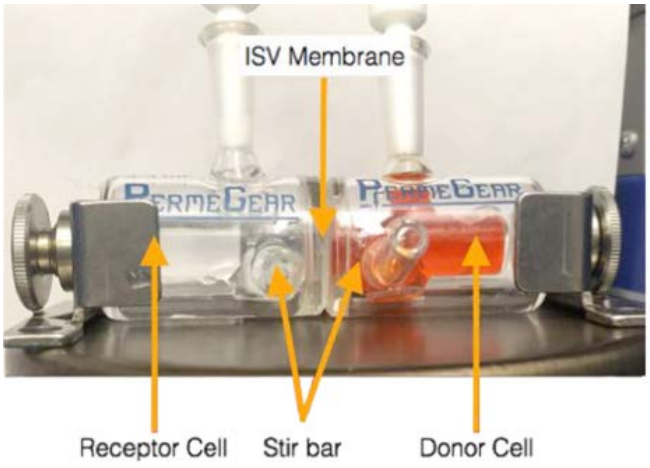

Figure 4.1 Experimental setup for membrane permeation studies: side-by-side stirred cell

The concentration of diffusant (methyl orange) was measured using a UV-VIS spectrophotometer (Varian Cary Model 5000) at a wavelength of 480 nm. Concentrations were determined based on standard curves of methyl orange. The diffusion constant of methyl orange can be determined from the cumulative mass $Q(t)$ of permeant passing through the membrane. The relevant relation is obtained by integration of the flux through the membrane (which is given by the well-known solution to Fick's second law for solute diffusion through pores) and reads as[20]

$$Q(t) = C(\varepsilon A)(\tau l)\left\{\frac{Dt}{(\tau l)^2} - \frac{1}{6} - \frac{2}{\pi^2}\sum_{n=1}^{\infty}\frac{(-1)^n}{n^2}e^{-n^2\pi^2\frac{Dt}{(\tau l)^2}}\right\} \quad (1)$$

Here, $Q(t)$ describes the cumulative mass of solute at time t. (εA) is the effective pore area of the membrane (ε is the porosity of the membrane and, A = 1.54 cm^2), (τl) is the length of the tortuous path (with, τ being the tortuosity). C is the concentration of solute (methyl orange) in the donor cell (C = 1 mg/mL) and, D is the diffusion coefficient (in our results section also referred to as D(exp). In the limit of large time t (*i.e.*, in the case of the steady state) $Q(t)$ simplifies to,

$$Q(t) = C(\varepsilon A)\frac{D}{\tau l}\left\{t - \frac{(\tau l)^2}{6D}\right\} \qquad (2)$$

Equation (2) has an intercept on the *t-axis*, referred to as the "time lag",[21] or t_{lag}, that follows as,

$$t_{\text{lag}} = \frac{(\tau l)^2}{6D} \qquad (3)$$

The steady state permeability, P (also referred to as P(exp) in our results section), for the transport of the permeant through the pores of the membrane can be evaluated by dividing Eqn. 2 by the concentration C and evaluating the time derivative to get,

$$P = \frac{1}{AC}\frac{dQ(t)}{dt} \equiv \frac{\varepsilon D}{\tau l} \qquad (4)$$

Note that either Eqn. 3 or Eqn. 4 can be applied to get the diffusion constant of solutes from the cumulative mass measurements (i.e. D(exp) = $P\tau\, l/\varepsilon$). If a lag time can be obtained experimentally (*i.e.*, if t_{lag} is in the range of conveniently accessible timescales), then analysis of Eqn. 3 is generally the preferable approach since only knowledge of the tortuosity is required.

Since in the presence of nano-sized pores hydrodynamic effects on the mobility of the solute molecules cannot be excluded, the theoretical effective diffusion coefficient of methyl orange diffusing in the membranes, $D(\lambda)$, was determined using Renkin's hydrodynamic model

(that describes the diffusion of a solid, spherical solute through an array of cylindrical pores with comparable size) valid for $0 \leqslant \lambda < 0.4$[22]:

$$D(\lambda) = (1-\lambda)^2(1 - 2.104\lambda + 2.09\lambda^3 - 0.95\lambda^5)D_w \qquad (5)$$

where λ is the solute-to-pore ratio (r_s/r_p) and D_w is the diffusivity of methyl orange dye in water. The first term in Eqn. 5, known as the 'steric factor', describes the restriction of the solute molecules entering into the pores (it is given by the ratio of the effective area $\pi(r_p\text{-}r_s)^2$ to the actual area πr_p^2). The second term describes the effect of the viscous drag due to the wall once the diffusant enters the pore. Membrane pore size was determined through image analysis of SEM micrographs using the ImageJ package. The solute size (in nm) was calculated by[23]:

$$\log_{10}(r_s) = -1.3363 + 0.395\log_{10}(M_w) \qquad (6)$$

where M_w is the molar mass of methyl orange (327 g/mol).

Eqn. 6 yields a solute radius equal to 0.45 nm, in good agreement with the value, r_s = 0.47 nm, obtained from a geometrical approximation ($r_s = (3M_w/(4\pi\rho N_{Av}))^{1/3}$), where ρ = 1.28 g/ml denotes the density of methyl orange at T = 25°C and N_{Av} is the Avogadro number,[22] and an experimental value of r_s=0.40 nm in NaCl solution.[24]

The permeability coefficient, $P(\lambda)$, can be estimated theoretically as follows,

$$P(\lambda) = \frac{\varepsilon D(\lambda)}{\tau l} \qquad (7)$$

Results and discussion

Effect of relative humidity (RH) on membrane top surface structure

The quality of the top surface pore structure is a key factor with regards to the high-performance of SNIPS derived UF membranes. SNIPS membranes are of particular interest due to their highly ordered mesopores derived from BCP self-assembly leading to high pore densities and uniform pore size. The casting conditions to achieve membranes with an optimum surface structure, including solvent system, solution concentration, evaporation time, etc., have been studied extensively. In this work, we evaluated another crucial, yet easy-to-ignore factor – relative humidity (RH).

ISV SNIPS membranes were casted inside a drybox as detailed in the experimental section. Inside the drybox, RH was controlled during the casting process by introducing water vapor or sparging with dry N_2. A humidity meter was used to determine RH during the evaporation process.

A membrane series from a solution of 9 wt% ISV119 in a 7/3 DOX/THF solvent mixture was produced by casting membranes at different RH employing an evaporation time of 200 s. Resultant membrane top surface structures as revealed by scanning electron microscopy (SEM) are shown in the top row of Figure 4.2. Associated FFT analyses of these SEM images are shown in Figure 4.3a.

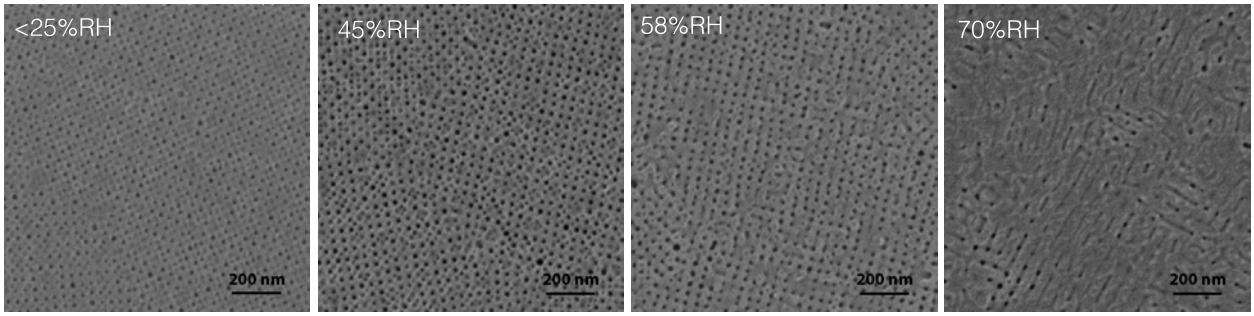

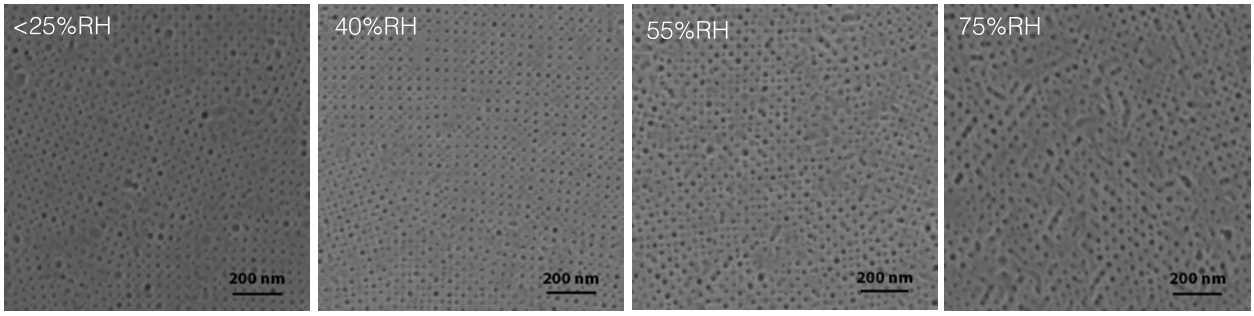

Figure 4.2 SEM micrographs of ISV119 membrane top surfaces casted at varying RH Membranes in the top row were obtained from a solution of 9 wt% ISV119 in a 7/3 DOX/THF solvent mixture and an evaporation time of 200 s. Membranes in the bottom row were fabricated from a solution of 11 wt% ISV119 in 7/3 DOX/THF solvent system casted onto 0.1 μm Nylon supports with an evaporation time of 100 s.

From the SEM images, top surfaces exhibited open and highly ordered pores with few defects when casted at 45% RH. FFT analysis confirmed pores packed in a 2D square lattice consistent with previous reports on ISV membranes.[3,25] At low humidity, (<25% RH), the top surface retained a well-ordered structure but with less open pores as compared to membranes casted at 45% RH. Increasing the humidity to 58% resulted in the presence of wormlike defects in the top surface. By further increasing the RH to 70%, top surface structure deteriorated substantially and assignment of a pore lattice from the associated FFT analysis is difficult. This series of membrane top surface structures suggested that the optimum RH value for casting ISV SNIPS membranes is at ~45%, with deterioration of the ordered pore surface structure when moving in particular to higher RH.

A second RH series was performed from a more concentrated ISV polymer solution. A solution of 11 wt% ISV119 in 7/3 DOX/THF solvent system was casted onto 0.1 μm Nylon

supports with an evaporation time of 100 s. The corresponding membrane top surface SEM images are shown in the bottom row of Figure 4.2. From these SEM images, the optimum RH remained to be around 40%, while this time higher and lower RH lead to an increase in surface defects. Furthermore, when compared with results of the 9 wt% ISV series, the 11 wt% ISV image series does not present as much of a surface structure disruption as RH is increased to 70% or above. This is also reflected in the FFT analyses (Figure 4.3), exhibiting improved lattice formation for higher RH values when moving from 9 wt% to 11 wt% ISV solutions. At RH above 70%, it was not possible from the FFT analysis to assign a lattice of the membrane casted from 9 wt% solution, while the counterpart from 11 wt% solution matched well with a square lattice. SEM top surface images were further analyzed for pore size distribution using ImageJ as shown in Figure 4.4. Results reveal that the membrane casted at 40% RH has the smallest average pore size when compared to membranes casted at <25%, 55%, and 75% RH. Furthermore, the membrane casted at 40% RH also exhibits a substantially narrower pore size distribution which is crucial for achieving high-resolution in separation processes. The coefficient of variation, σ/μ (ratio of standard deviation, σ, and mean, μ), is smallest in membranes casted at 40% RH (σ/μ= 0.36, 0.28, 0.36, and 0.38 for 25%, 40%, 55%, and 75% RH, respectively, for normal Gaussian fits and σ/μ= 0.14, 0.12, 0.14, and 0.15 for 25%, 40%, 55%, and 75% RH, respectively, for log-normal distributions[26]).

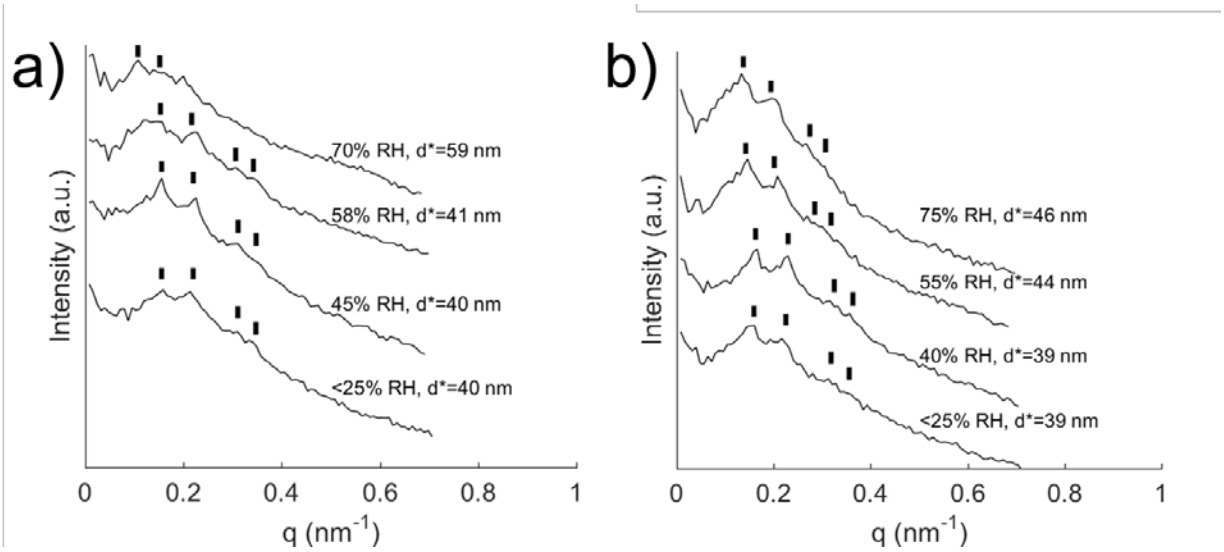

Figure 4.3 Radially integrated FFTs of SEM images of ISV119 membranes casted at varying RH from polymer casting solutions of a) 9 wt% and b) 11 wt%.

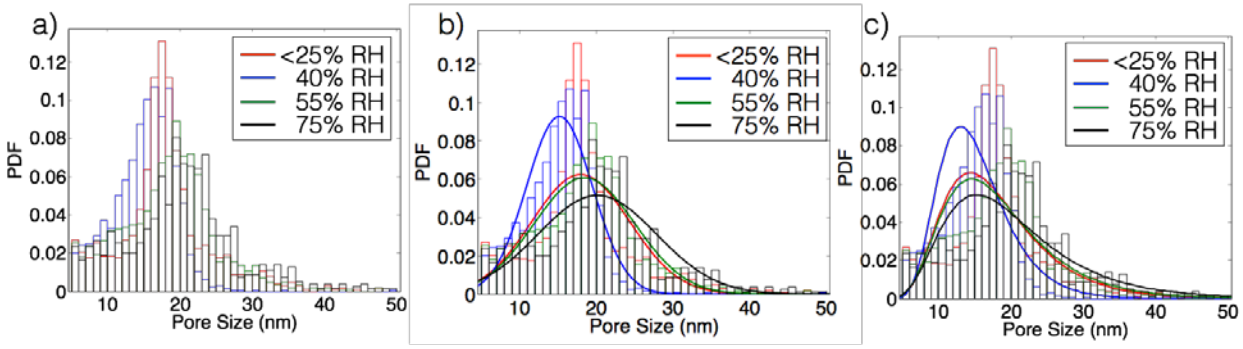

Figure 4.4 Pore size distribution analyses of ISV119 membranes casted at varying RH from polymer casting solutions of 11 wt%. a) pore size histograms; b) histograms with corresponding normal Gaussian fits (σ/μ= 0.36, 0.28, 0.36, and 0.38 for 25%, 40%, 55%, and 75% RH, respectively); c) histograms with corresponding log-normal fits (σ/μ= 0.14, 0.12, 0.14, and 0.15 for 25%, 40%, 55%, and 75% RH, respectively).

The FFT analyses of the top surface SEM images also allowed us to quantify the respective pore-to-pore distances, d^*. Comparing results in Figure 4.3a and b for both 9 wt% and 11 wt%

ISV humidity series suggests that with increasing humidity, d^* increases. While values for d^* stay unchanged for low (<25%) and mid range (45% and 40%) RH, increasing RH further to first 58% or 55%, and then to 70% or 75%, increases d^* substantially. This increase in pore-to-pore distance results in a concomitant decrease in surface pore density, see results for the 11 wt% ISV series in Table 4.2. Therefore, when assuming a constant pore size and pore size distribution, membranes casted at RH around 45% not only have more well defined top surface layers with narrower pore-size distributions expected to provide higher resolution, they should also be more permeable as a result of higher pore densities.

Table 4.2 Pore density of humidity series casted from 11 wt% solution

Humidity	**Pore density ($x10^{14}$ pores/m^2)**
<25%RH	6.8
40%RH	8.0
55%RH	6.7
75%RH	5.1

Permeation studies of small molar mass model solute

Influence of relative humidity on permeation

We investigated the effect of RH on solute transport properties of ISV119 membranes (11 wt%; 100s evaporation time) casted at 40% and 75% RH conditions. **Figure 4.5** shows the cumulative amounts of methyl orange dye permeated through ISV119 membranes at neutral pH,

i.e. at a pH where the poly(4-vinlypyridine) chains are un-protonated and the pores therefore open, as compared to pH=4, i.e. a pH at which protonation leads to chain stretching and therefore to closed pores (pK_a(P4VP)=4.6).[3] The values of the diffusion coefficient, *D*(exp), calculated from the time-lag method (Eqn. 3), for the open states are listed in Table 4.3. A convexity or lag-time can be observed at short elapsed times before the system reaches a pseudo-steady state. The permeation rate of methyl orange is higher by almost a factor 4 in membranes casted at the optimized RH of 40% as compared to membranes cast at 75% RH. The higher permeation rate is consistent with the more highly ordered surface structure with fewer defects and resulting higher pore density of more narrowly size-distributed pores. On the time scale of the experiments, membranes in the closed state at pH=4 were not permeable at all to the small molar mass solute methyl orange.

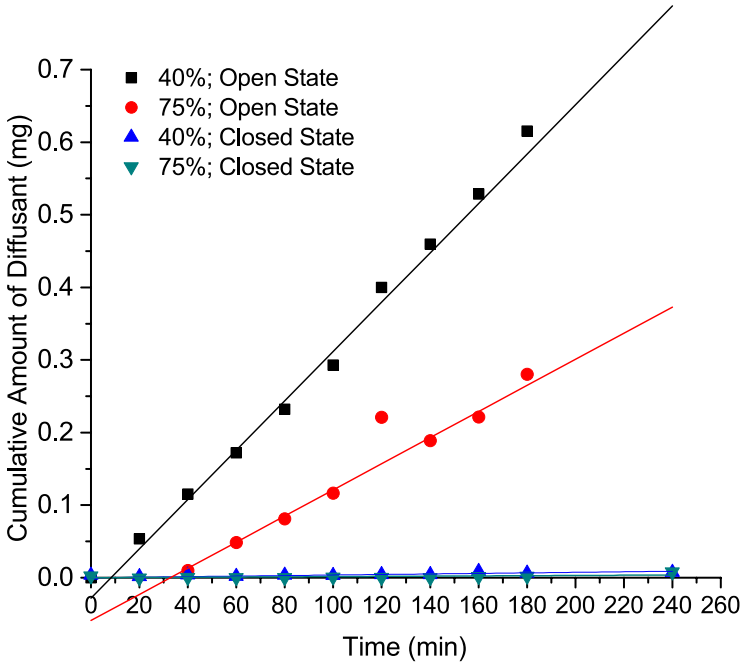

Figure 4.5 Cumulative amounts of methyl orange permeated through ISV119 membranes casted at 40% and 75% RH in open and closed states. Lag-times for ISV119 membranes in the open state are 8.3 min and 33 min for membranes casted at 40% and 75% RH, respectively (Table 4.3).

Table 4.3 Diffusion coefficient of methyl orange diffusing through ISV119 membranes casted from 40% and 75%RH together with membrane pore size analysis results.

Polymer	***D*(exp)** **($\times 10^{-8}$ cm^2/s)[a]**	ε	$r_p=\mu$	σ
ISV119 40% RH	3.3 t_{lag}= 8.3 min	15.76%	7.9	2.5
ISV119 75% RH	0.8 t_{lag}= 33 min	18.34%	10.7	4.7

[a]As determined through the time-lag method (Eqn. 3).

Average pore size (r_p or μ) and porosity (ε) determined from ImageJ analysis and σ calculated from log normal fits (see text).

Influence of pore size on permeation

To gain a greater understanding of the relationship between BCP architecture, membrane structure, and performance, the permeation of the model dye methyl orange was evaluated for a series of ISV membranes with varying molar mass. As previously reported by Dorin *et al.*,[25] membranes fabricated from ISV terpolymers with similar volume fractions but increasing molar mass are characterized by increasing pore diameters. As a result, ISV membrane water and polymer solute rejection performance could be systematically tuned through tailoring of

terpolymer molar mass. The present study was designed to assess small molar mass solute transport through ISV membranes as a function of molar mass.

Membranes fabricated from varying molar mass terpolymers were prepared by dissolving the triblock terpolymer into a binary solvent system of 7/3 DOX/THF by weight ratio. Supported membranes were cast from a 16 wt% ISV43, 12 wt% ISV99, and 11 wt% ISV119 polymer solution pipetted directly onto a 0.1 μm nylon support (Sterlitech Inc.) with an evaporation time of 100s and the optimized casting condition of 40% RH. SEM micrographs of the top surfaces are shown in Figure 4.6. All membrane top surfaces are characterized by highly ordered pores forming square lattices.

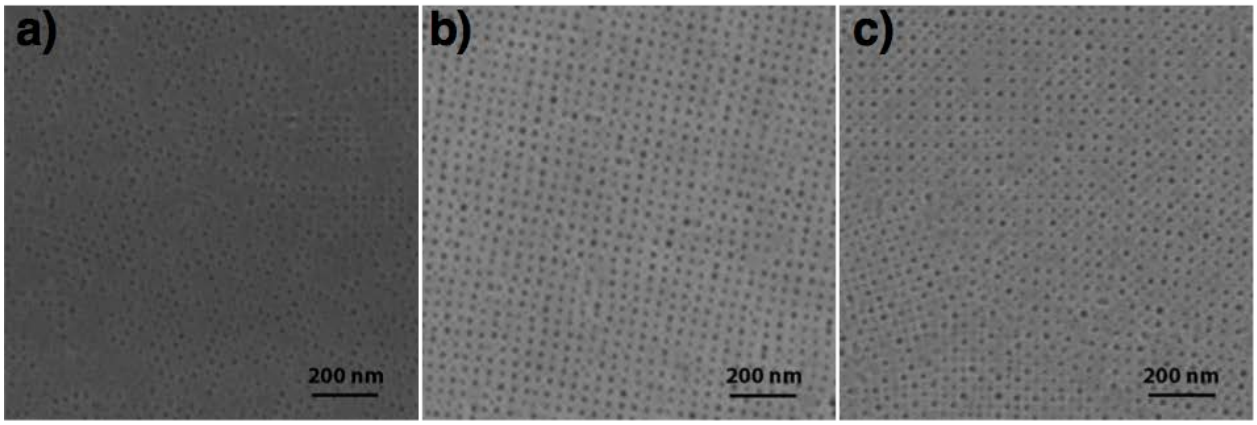

Figure 4.6 SEM characterization of top surfaces of ISV membranes from a) ISV43, b) ISV99, and c) ISV119, all cast at 40% RH. Supported membranes were cast from a 16 wt% ISV43, 12 wt% ISV99, and 11 wt% ISV119 polymer solution in 7/3 DOX/THF pipetted directly onto a 0.1 μm nylon support (Sterlitech Inc.) with an evaporation time of 100s.

The ISV43, ISV99, and ISV119 membranes were subjected to pH 7 (“open” state) and pH 4 (“closed” state) solutions of methyl orange as described above. The 0.1M buffer solutions used

in the permeation experiments is expected to screen the electrostatics associated with the charged dye molecule. The cumulative amount of diffusant through the membranes in different states over time is shown in Figure 4.7 with corresponding calculated values of *D*(exp) listed in Table 4.4.

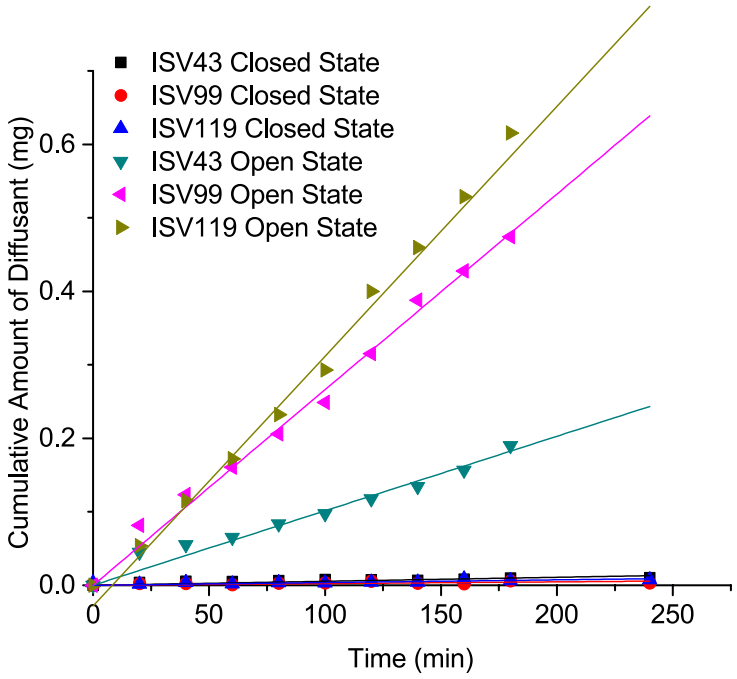

Figure 4.7 Cumulative amounts of methyl orange permeated through varying molar mass ISV triblock terpolymer membranes for open and closed states.

Table 4.4 Diffusion and permeability coefficients of methyl orange permeating through different ISV membranes for closed and open states together with membrane pore size analysis results.

	Closed State	**Open State**	**Open State**				
Polymer	***D*(exp)[a] (x10^{-8} cm^2/s)**	***D*(exp) (x10^{-8} cm^2/s)**	***P*(exp)* (x10^{-5} cm/s)**	**Pore density (x10^{14} pores/m^2)**	***ε***	***r_p=μ***	***σ***
ISV43	15.3	280[a]	1.1	4.6	3.86%	5.2	1.4
ISV99	1.4	160[a]	2.9	7.2	18.33%	9.0	2.0
ISV119	2.5	220[a]/3.3[b] t_{lag}=8.3 min	3.5	8.0	15.76%	7.9	2.5

* As determined from Eqn. 4 *i.e.*, *P*(exp)=slope/(*AC*)

[a] As determined through Eqn. 4.

[b] As determined through the time-lag method (Eqn. 3).

Average pore size (r_p or μ) and porosity (ε) determined from ImageJ analysis and σ calculated from log normal fits (see text).

Under neutral conditions ("open" state), the permeation rate of methyl orange increased with ISV terpolymer molar mass. While this is the expected behavior, closer inspection reveals that this trend is based on two different effects. Average pore size from image analysis (see Table 4.4) first increases from 10 nm for ISV43 to 18 nm for ISV99, but then decreases to 16 nm for ISV119. Therefore, pore size alone cannot explain the observed trend in *P*(exp) in Table 4.4.

Interestingly, for the molar mass series of terpolymer membranes studied here contrary to expected behavior the pore density increases with molar mass (Table 4.4, right side). So while moving from ISV99 to ISV119 average pore size decreases from 18 to 16 nm, pore density increases from 7.2 to 8.0x10^{14} pores/m^2. Together with differences in substructure not assessed here, this may account for the increased diffusion of the small molar mass model solute. The low

pore density of ISV43 membranes may be due to closed pores, unrecognized by ImageJ during analysis, compare top surface SEM images in Figure 4.6.

As expected, under acidic conditions ("closed" state), the permeation rate again is reduced to a minimal amount for all membranes tested (compare Figures 4.5 and 4.7). In the "closed" state, pores are effectively closed preventing diffusion of methyl orange through the membranes. The lack of diffusion through the ISV membrane is likely a result of pore size changes and not primarily an effect of electrostatics. This is supported by the fact that the charge of the methyl orange dye in the 0.1M buffer solution is expected to be fully screened. The change in permeation rate from 220 x 10^{-8} cm^2/s ("open" state) to 2.5 x 10^{-8} cm^2/s ("closed" state) for ISV119 membranes can be regarded as an "on" and "off" switch brought on by pH changes.

In order to provide deeper insights into the effects of membrane structure on small molar mass solute transport, experimental results were compared to theoretical predictions. It is essential to characterize the entirety of the cross section of ISV membranes for permeation analysis. ISV membranes are characterized by a surface separation layer, which has a simple cubic structure[3, 17] (~100-200 nm thick; described above) on top of a 3D interconnected macroporous sponge-like substructure. Furthermore, the relatively thick (~50-60 μm) and asymmetric sponge type substructure of these ISV membranes consists of macropore walls that themselves are mesoporous, (i.e. the substructure is not only asymmetric, but truly hierarchical).[3] This is in stark contrast to what has been described for PS-*b*-P4VP diblock copolymer derived UF membranes.[2] Therefore, we expect tortuous paths of solute molecules through these mesopores all the way through the entire membrane. As a result, in order to simplify the theoretical description, we used the hindered diffusion model and assumed a constant porosity throughout. For example, the measured diffusion coefficient, D(exp), of methyl orange dye in UF membrane ISV99 in the open state at pH 7 (160

x 10^{-8} cm^2/s) is about a factor of three lower than the bulk solution value that is calculated using the Stokes-Einstein relationship, $D_w = k_bT/(6\pi \eta r_s)$ ~ 5.4 x 10^{-6} cm^2/s (where k_b is Boltzmann's constant, T = 25°C, and η is the viscosity of water at 25°C, and the solute radius is estimated from Eqn. 6 as r_s = 0.45 nm). Based on the hydrodynamic theory for hindered diffusion of a solid, spherical solute through an array of cylindrical pores with comparable size as described by the Renkin equation (Eqn. 5), theoretical diffusion coefficients, $D(\lambda)$, were calculated for the different ISV terpolymer membranes as listed in Table 4.5. A hindered diffusion model was chosen to simplify solute diffusion through the complex pore structures of ISV membranes using the whole membrane thickness of l = 100 μm. Here we note that the assumption of continuity of the cylindrical nanopore structure of the separation layer across the total membrane thickness is not consistent with the actual membrane structure that shows a graded morphology with interconnected meso-, and macroporous regions (*vide infra*). Nevertheless, in the absence of a complete description of the membrane structure, the applied approximation was found to be helpful to interpret transport in terpolymer based UF membranes. Following this approach, the diffusion coefficients (for ISV119 membranes) were determined through Eqn. 3 (time-lag method) and Eqn. 4 for comparison. Additionally, theoretical permeability coefficients, $P(\lambda)$, were determined as a function of solute-to-pore size ratio and tortuosity **(**Eqn. 7**)**. In order to compare experimental and theoretical permeability coefficients, $P(\lambda)$ values were first calculated assuming a membrane thickness of l = 100 μm and without taking tortuosity into account (i.e. τ=1). The resulting values were within the same order of magnitude as P(exp), (compare columns 2 and 4 in Table 4.5).

As evidenced in earlier studies by cross sectional SEM images, neither separation layer nor substructure of ISV terpolymer membranes consist of vertical cylinder pores. For example, in

the separation layer the cubic pore network is characterized by vertical and horizontal channels.[3,6-8,11] The solutes' pathway is therefore expected to be very tortuous as molecules can move vertically as well as horizontally through the selective layer. By equating P(exp) to $P(\lambda)$, calculated values of τ, used here as a fitting parameter, fall close to the typical tortuosity range of 1.5 – 2.5[27] for mesoporous membranes. These results suggest that the combined effects of hydrodynamic hindered diffusion and pore tortuosity can account for the observed small molar mass solute transport through ISV based UF membranes taking into account the entire membrane thickness (l = 100 μm).

For comparison $P(\lambda)$ values were also calculated assuming that only the selective top separation layer with l = 100 nm contributes to hindered diffusion. It is obvious from Table 4.5 that this does not provide satisfactory results as theoretical $P(\lambda, \tau = 1)$ values now are different by orders of magnitude from the experiments (compare $P(\lambda)$ in column 6 with P(exp) in column 2). Furthermore, matching experimental with theoretical results would require non-physical tortuosity values as also shown in Table 4.5 (column 7).

Table 4.5 Summary of diffusion and permeability coefficients from theoretical predictions and experimental data.

Membrane	***P*(exp)*** **(x10^{-5} cm/s)**	***D*(λ)** **(x10^{-6} cm^2/s)**	***P*(λ)** **(x10^{-5} cm/s)** τ**=1** ***l*=100 μm**	τ^c ***l*=100 μm**	***P*(λ)** **(x10^{-2} cm/s)** τ**=1** ***l*=100 nm**	τ^c ***l*=100 nm**	***D*(exp)** **(x10^{-6} cm^2/s)** τ**=1**
ISV43	1.1	3.7	1.4	1.3	1.4	1300	2.8[a]
ISV99	2.9	4.4	8.0	2.8	8.0	2800	1.6[a]
ISV119 (40% RH)	3.5	4.2	6.6	1.9	6.6	1900	2.2[a] (0.033[b]; t_{lag}=8.3 min)
ISV119 (75% RH)	1.5	4.5	8.3	5.5	8.3	5500	0.8[a] (0.008[b]; t_{lag}=33 min)

[*] As determined from Eqn. 4 *i.e.*, *P*(exp)=slope/(*AC*)

[a] As determined from Eqn. 4, $D(\text{exp}) = P(\text{exp})\,(\tau l)\,/\varepsilon$ (assuming $\tau = 1$),

[b] As determined by the time-lag method (Eqn. 3),

[c] As determined by equating *P*(exp) to $P(\lambda, \tau)$.

Conclusion

In summary, ISV membranes derived from the SNIPS process were fabricated from ISV triblock terpolymers ranging in molar mass from 43 kg/mol to 119 kg/mol at varying levels of RH during the casting process. Investigations into the influence of RH on membrane surface structure revealed that ISV membranes exhibited optimal surface ordering and pore density when casted at mid range values around 40-45% RH. The observed structural changes correlated with differences in permeation rate of a model small molar mass solute through membranes casted at

optimal and non-optimal RH, with higher diffusivity observed in the membrane characterized by a more ordered surface structure obtained at optimal RH.

Analysis into the relationship between triblock terpolymer molecular size and diffusion performance revealed that membranes fabricated from higher molar mass ISV terpolymers exhibited higher small molar mass solute diffusivity. Results could be rationalized by taking into account observed membrane pore size and pore density. Moreover, combining predictions of a hydrodynamic theory assuming hindered diffusion of a solid, spherical solute through an array of cylindrical pores of comparable size with the effect of pore tortuosity, observed values of the small molar mass solute permeability coefficients could only be accounted for when the entire membrane thickness (l = 100 μm) rather than only the thickness of the top separation layer (l = 100 nm) was used in the calculations.

The ability to extend the use of SNIPS membranes away from regular separation applications and towards the use as well-controlled delivery vehicles rests on tuning membrane properties via BCP molecular design and architecture as well as on finding optimal membrane casting conditions. This study suggests that through tailoring of BCP molar mass and relative humidity during casting, the rate of release and diffusion of solutes through SNIPS membranes can be controlled for targeted performance.

Acknowledgments

The authors would like to acknowledge funding of this work by the FLIR Systems, Inc. and the Defense Threat Reduction Agency (DTRA) Contract No. HDTRA1-13-C0003. This work utilized the Cornell Center for Materials Research (CCMR) facilities supported by NSF MRSEC

program (DMR-1120296). Y.G. acknowledges funding by the National Science Foundation (DMR-1409105).

REFERENCES

1. R.M. Dorin, D. Salomon Marques, H. Sai, U. Vainio, W.A. Phillip, K.V. Peinemann, S.P. Nunes, U. Wiesner, Solution Small Angle X ray Scattering as a Screening and Predictive Tool in the Fabrication of Asymmetric Block Copolymer Membranes, ACS Macro Lett. 1 (2012) 614−617.

2. K.V. Peinemann, V. Abetz, P.F.W. Simon, Asymmetric superstructure formed in a block copolymer via phase separation, Nat. Mater. 6 (2007) 992-996.

3. W.A. Phillip, R.M. Dorin, J. Werner, E.M. Hoek, U. Wiesner, M. Elimelech, Tuning structure and properties of graded triblock terpolymer-based mesoporous and hybrid films, Nano Lett. 11 (2011) 2892-2900.

4. R.A. Mulvenna, J.L. Weidman, B. Jing, J.A. Pople, Y. Zhu, B.W. Boudouris, W.A. Phillip, Tunable nanoporous membranes with chemically-tailored pore walls from triblock polymer templates, J. Membr. Sci. 470 (2014) 246-256.

5. Q. Zhang, Y. Gu, Y.M. Li, P.A. Beaucage, T. Kao, U. Wiesner, Dynamically Responsive Multifunctional Asymmetric Triblock Terpolymer Membranes with Intrinsic Binding Sites for Covalent Molecule Attachment, Chem. Mater. 28 (2016) 3870–3876.

6. Y.M. Li, D. Srinivasan, P. Vaidya, Y. Gu, U. Wiesner, Asymmetric Membranes from Two Chemically Distinct Triblock Terpolymers Blended during Standard Membrane Fabrication, Macromol. Rapid Commun. 37 (2016) 1689-1693.

7. Q. Zhang, Y.M. Li, Y. Gu, R.M. Dorin, U. Wiesner, Tuning substructure and properties of supported asymmetric triblock terpolymer membranes, Polymer 107 (2016) 398-405.

8. M.M. Pendergast, R.M. Dorin, W.A. Phillip, U. Wiesner, E.M.V. Hoek, Understanding the structure and performance of self-assembled triblock terpolymer membranes, J. Membr. Sci. 444 (2013) 461-468.

9. S. Rangou, K. Buhr, V. Filiz, J.I. Clodt, B. Lademann, J. Hahn, A. Jung, V. Abetz, Self-organized isoporous membranes with tailored pore sizes, J. Membr. Sci. 451 (2014) 266-275.

10. A. Jung, S. Rangou, C. Abetz, V. Filiz, V. Abetz, Structure Formation of Integral Asymmetric Composite Membranes of Polystyrene-block-Poly (2-vinylpyridine) on a Nonwoven, Macromol. Mater. Eng. 297 (2012) 790-798.

11. Y. Gu, U. Wiesner, Tailoring Pore Size of Graded Mesoporous Block Copolymer Membranes: Moving from Ultrafiltration toward Nanofiltration, Macromol. 48 (2015) 6153-6159.

12. S.P. Nunes, R. Sougrat, B. Hooghan, D.H. Anjum, A.R. Behzad, L. Zhao, N. Pradeep, I. Pinnau, U. Vainio, K.V. Peinemann, Ultraporous films with uniform nanochannels by block copolymer micelles assembly, Macromol. 43 (2010) 8079-8085.

13. V. Abetz, Isoporous block copolymer membranes, Macromol. Rapid Commun. 36 (2015) 10-22.

14. C. Stegelmeier, V. Filiz, V. Abetz, J. Perlich, A. Fery, P. Ruckdeschel, S. Rosenfeldt, S. Förster, Topological paths and transient morphologies during formation of mesoporous block copolymer membranes, Macromol. 47 (2014) 5566-5577.

15. L. Oss-Ronen, J. Schmidt, V. Abetz, A. Radulescu, Y. Cohen, Y. Talmon, Characterization of block copolymer self-assembly: from solution to nanoporous membranes, Macromol. 45 (2012) 9631-9642.

16. D.S. Marques, R.M. Dorin, U. Wiesner, D.M. Smilgies, A.R. Behzad, U. Vainio, K.V. Peinemann, S.P. Nunes, Time-resolved GISAXS and cryo-microscopy characterization of block copolymer membrane formation, Polymer 55 (2014) 1327-1332.

17. Y. Gu, R.M. Dorin, K.W. Tan, D.M. Smilgies, U. Wiesner, In Situ Study of Evaporation-Induced Surface Structure Evolution in Asymmetric Triblock Terpolymer Membranes, Macromol. 46 (2016) 4195-4201.

18. B. Sutisna, G. Polymeropoulos, V. Musteata, K.V. Peinemann, A. Avgeropoulos, D.M. Smilgies, N. Hadjichristidis, S.P. Nunes, Design of block copolymer membranes using segregation strength trend lines, Mol. Syst. Des. Eng. 1 (2016) 278-289.

19. S.Y. Yang, J.A. Yang, E.S. Kim, G. Jeon, E.J. Oh, K.Y. Choi, S.K. Hahn, J.K. Kim, Single-file diffusion of protein drugs through cylindrical nanochannels. ACS Nano, 4 (2010) 3817-3822.

20. J. Crank, The Mathematics of Diffusion, Oxford University Press, Oxford, 1975.

21. R.A. Siegel, E.L. Cussler, Reactive barrier membranes: some theoretical observations regarding the time lag and breakthrough curves. J. Membr. Sci. 229 (2004) 33-41.

22. E.M. Renkin, Filtration, diffusion, and molecular sieving through porous cellulose membranes. J. Gen. Physiol, 38 (1954), 225-243.

23. W.R. Bowen, A.W. Mohammad, Characterization and prediction of nanofiltration membrane performance—a general assessment. Chem. Eng. Res. Des., 76 (1998), 885-893.

24. M. Mitsuishi, A. Datyner, Diffusion of methyl orange and its homologs in water and in micellar solution of dodecyltrimethylammonium bromide. Sen'i Gakkaishi, 36 (1980), T175-T178.

25. R.M. Dorin, W.A. Phillip, H. Sai, J. Werner, M. Elimelech, U. Wiesner, Designing block copolymer architectures for targeted membrane performance. Polymer, 55 (2014) 347-353.

26. K.H. Youm, S.W. Kim, Prediction of intrinsic pore properties of ultrafiltration membrane by solute rejection curves: effects of operating conditions on pore properties. Journal of chemical engineering of Japan, 24 (1991), 1-7.

27. R.W. Baker, Membrane technology and applications, England, 2004.

APPENDIX C

Table S4.1 Pore size and porosity of ISV119 membranes casted at 40% and 75% RH.

Polymer	$r_p=\mu$	ε	σ
ISV119 40% RH	7.9	15.76%	2.5
ISV119 75% RH	10.7	18.34%	4.7

*Average pore size (r_p or μ) and porosity (ε) determined from ImageJ analysis and σ calculated from log normal fits.

Table S4.2 Pore size and porosity of ISV43, ISV99, and ISV119 membranes casted at 40% RH.

Polymer	$r_p=\mu$	ε	σ
ISV43	5.2	3.86%	1.4
ISV99	9.0	18.33%	2.0
ISV119	7.9	15.76%	2.5

*Average pore size (r_p or μ) and porosity (ε) determined from ImageJ analysis and σ calculated from log normal fits.

CHAPTER 5

DYNAMICALLY RESPONSIVE MULTIFUNCTIONAL ASYMMETRIC TRIBLOCK TERPOLYMER MEMBRANES WITH INTRINSIC BINDING SITES FOR COVALENT MOLECULE ATTACHMENT[*]

Abstract

Asymmetric ultrafiltration membranes derived from block copolymer self-assembly have seen growing attention as a result of their ordered pore structures and scalable fabrication process. One route to extend their utility is to provide, through the molecular architecture of the block copolymer, covalent binding sites for facile attachment of foreign functional molecules. Here, we report the synthesis of triblock terpolymer poly(styrene-*b*-4-vinylpyridine-*b*-propylene sulfide) (SVPS) and its fabrication into isoporous ultrafiltration membranes. Final SVPS membrane top surfaces exhibit narrowly dispersed mesopores with six-fold symmetry. Membranes show a switchable response to pH changes demonstrating the potential as a chemical gate. Membrane pore surfaces are decorated with thiol groups providing active covalent binding sites via versatile thiol-ene click chemistry. The work may open pathways to produce high-performance multifunctional membranes for chem- and bio- sensing, separation and as membrane reactors.

[*]Reprinted (adapted) with permission from Q. Zhang, Y. Gu, Y. M. Li, P. A. Beaucage, T. Kao, U. Wiesner, Dynamically Responsive Multifunctional Asymmetric Triblock Terpolymer Membranes with Intrinsic Binding Sites for Covalent Molecule Attachment, *Chem. Mater.* **28**, 3870-3876 (2016). Copyright American Chemical Society.

Introduction

Synthetic ultrafiltration membranes benefit from narrowly dispersed pores and high porosity to ensure high selectivity, permeability and process control. One route to such materials utilizes block copolymer (BCP) self-assembly together with the industrially scalable nonsolvent induced phase separation process (NIPS), now referred to as the SNIPS method.[1,2] Membranes fabricated via SNIPS have a mesoscale isoporous separation layer and a graded substructure with macroporosity. The integral asymmetric structure ensures good selectivity while maintaining high permeability. The SNIPS process has been applied to a variety of diblock copolymers and triblock terpolymers, a number of which contained a responsive end block enabling the membrane to respond to certain stimuli. [1-5] For example, the most widely studied systems are poly(styrene)-block-poly(4-vinylpyridine) (SV) and poly(isoprene)-block-poly(styrene)-block-poly (4-vinylpyridine) (ISV), both containing the poly(4-vinylpyridine) (P4VP) end block. Protonation induced P4VP chain charging leads to pH responsive pore closing via chain stretching. SNIPS membranes have been used in biological and environmental applications such as protein separation, controlled release and water purification.[6-8]

In order to design smarter, more dynamic membrane systems, it is desirable to use block copolymer architectures enabling attachment of foreign functional components, e.g. in a facile post-membrane-fabrication step. A critical challenge is the lack of effective incorporation methods. Several attempts have been made to achieve double-functionality through a binding layer, such as polydopamine,[9-11] which enables other functional materials to adhere to membranes. This extrinsic binding layer, however, suffers from easy exfoliation during membrane usage. Also, the formation of a binding layer and its functionalization requires multiple post-processing steps. Gu *et al*[12] employed a co-assembly method to incorporate an inorganic component into the

polymeric membranes, but this method only works when additives are compatible with organic solvents used for casting. Philip *et al*. produced membranes with pores lined by acrylic acid moieties for which they anticipated further functionalization capabilities, again suggesting multiple post-membrane-fabrication steps.[8,13] The study did not demonstrate the use of acrylic acid as coupling sites, however. Another challenge in this field is to expand on the diversity of chemistries leading to responsive behavior. To date most SNIPS studies are restricted to a single stimulus response, for example to pH changes, originating from P4VP[14] and poly(acrylic acid) (PAA)[13] blocks in the BCP. Thermo-responsive behavior was achieved through poly(N-isopropylacrylamide) (PNIPAm) blocks.[9] Poly(N,N-dimethylaminoethyl methacrylate)[15] responds to both, pH and thermal stimuli. To the best of our knowledge there are no reports to date on SNIPS membranes from block copolymers enabling direct covalent attachment to the membrane via coupling to copolymer functional groups.

In this paper, we propose a solution to these challenges by designing a block copolymer with both responsive and covalent binding capabilities. To that end a new triblock terpolymer, poly(styrene)-block-poly (4-vinylpyridine)-block-poly(propylene sulfide) (SVPS) was successfully synthesized with a very small poly(propylene sulfide) (PPS) fraction. Terminal sulfhydryl groups were introduced when the PPS block was terminated by a proton donor during anionic polymerization.[16] Via SNIPS the terpolymer was successfully processed into an asymmetric ultrafiltration membrane. In addition to the pH responsiveness from the P4VP component, the end PPS block provides thiol functional groups for covalent bonding via thiol-ene click chemistry. This reaction is versatile towards numerous biomolecules and results in strong covalent bonds, offering a versatile platform for foreign molecule attachment. Although

not studied in depth here, the oxidation-responsive behavior of the PPS block is another interesting feature that could potentially add to the membrane's multi-functionality.[17]

Based on previous results,[14,17] the fact that the short functional PPS end block is linked to the P4VP middle block should ensure that the sulfhydryl groups line the pore walls and membrane surfaces. The macromolecular design of SVPS thereby should not only enable stimuli responsive behavior but at the same time should allow chemical modifications of the pore walls. This concept may be generalized to future designs of block copolymer architectures providing extended responsiveness and multi-functionality of SNIPS derived membranes.

Methods

Synthesis

Poly(styrene)-block-poly(4-vinylpyridine)-block-poly(propylene sulfide) (SVPS) was synthesized via sequential anionic polymerization. The polymerization of styrene was initiated with sec-butyllithium in tetrahydrofuran (THF) and was conducted for four hours in a dry ice/isopropanol bath at -78 °C, before the addition of 4-vinylpyridine (4VP). The polymerization of 4VP was conducted at -78 °C for three hours. Upon the complete polymerization of 4VP, propylene sulfide monomer was added at -78 °C. The reaction was allowed to warm up to room temperature and stirred for another two hours. The polymer was then terminated with acidic methanol, precipitated into a water/methanol mixture, and vacuum dried at 50 °C for two days. The SVPS triblock terpolymer used in this study has a molar mass of 63 kg/mol, a polydispersity index of 1.06 and weight fractions of 0.74, 0.22, and 0.04 for polystyrene, poly(4-vinylpyridine) and poly(propylene sulfide) blocks, respectively.

Poly(styrene)-block-poly(4-vinylpyridine) (SV) was synthesized in a similar way as a control polymer. Polymerization was conducted for both monomers in THF at -78 °C and terminated with methanol. The SV block copolymer described in this study has a molar mass of 103 kg/mol, a polydispersity index of 1.19 and weight fractions of 0.74 and 0.26 for polystyrene and poly(4-vinylpyridine) blocks, respectively.

Material Characterization

Polymer molar mass characterization was performed via a combination of gel permeation chromatography (GPC) and NMR. The GPC instrument was equipped with a Waters 515 pump, PSS GRAM 100-1000-3000 columns and an Agilent 1200 refractive index detector, using N,N-dimethylformamide (DMF) as eluent. ^{1}H NMR measurements were performed on an INOVA 600 NMR spectrometer at 600 MHz using chloroform-d as the solvent. Scanning electron microscopy (SEM) images of membranes were acquired on a Tescan LM Mira3 FE-SEM with an in-lens detector. Fast Fourier transform (FFT) analysis of the membrane top surface in Figure 3a was obtained via ImageJ with the Radial Profile Extended plugin (Philippe Carl). Image processing is detailed in the Supporting Information. Solutions for small-angle X-ray scattering (SAXS) were prepared by dissolving different amounts (see main text) of SVPS terpolymer into a solvent mixture of THF and dioxane (DOX) (1:1 by weight), with solutions centrifuged into 0.9 mm glass capillaries (Charles-Supper Co.) and capillaries flame sealed. SAXS patterns of the solutions were obtained at station G1 of the Cornell High Energy Synchrotron Source (CHESS) using a point-collimated beam with a typical sample-to-detector distance of 2.3 m and incident photon energy of 9.83 keV. 2D scattering patterns were collected using a Pilatus3-300k pixel array detector (Dectris, Inc.) and radially integrated to give the spectra shown in Figure 2. The scattering vector,

q, is defined as $q = (4\pi)sin\theta/\lambda$, where θ is half of scattering angle and λ is the X-ray wavelength, λ = 0.1247 nm.

Membrane preparation

SVPS membranes were fabricated from a 9 wt % solution in THF/DOX (1:1 by weight) and SV membranes from a 15 wt % solution in THF/DMF/DOX (1:1:1 by weight) via the SNIPS process.[2,14] All membranes were casted by doctor-blading at a gate height of 220 μm. The evaporation time was 45 s for SVPS membranes and 20 s for SV membranes before immersion into a deionized water bath.

Ellman's reagent experiments

A 0.01 M Ellman's reagent (5,5'-dithiobis-(2-nitrobenzoic acid) or DTNB) stock solution in methanol and a 0.2 M tris-buffer containing 0.02 M (EDTA Na_2) were prepared separately. Then 1.5 mL tris-buffer, 0.1 mL DTNB stock solution, and 8.4 mL methanol were mixed together as Ellman's reagent solution (final solution was in a buffer/methanol mixture, 15:85 by volume). Two membranes with area, A, of 5 cm^2 each were soaked in 2 mL Ellman's reagent solution. The solutions were tested for absorbance after 12 h reaction.

The amount of total and accessible thiol groups was calculated as follows:

$$Total\ thiol\ groups\ per\ area = \frac{membrane\ weight}{SVPS\ molecular\ weight\ \times\ A}$$

$$Accessible\ thiol\ groups\ per\ area\ = \frac{Absorbance\ at\ 412\ nm\ \times\ V}{Extinction\ coefficient\ \times\ L\ \times\ n\ \times\ \mathrm{A}}$$

where V is the volume of Ellmans's solution, n is the number of membranes soaked in the solution, A is the area of the membrane, and L is the cuvette path length.

Redox reactions with SVPS

SVPS polymer, stored at 4 °C, was thawed and dissolved in DMF. An aliquot was taken for GPC analysis representing “as-made polymer” as a control. The solution was stirred in air at 60 °C for 29 hours to oxidize thiols into disulfides and an aliquot was taken for GPC analysis representing “oxidized polymer”. An excessive amount of reducing agent dithiothreitol (DTT) was added to the oxidized polymer solution. The solution was stirred at 60 °C for four days and an aliquot was taken for GPC analysis representing “reduced polymer”.

Hydraulic permeability tests

A 10 mL stirred dead-end ultrafiltration test cell (Amicon 8010, Millipore, effective area 4.1 cm^2) was used in the permeability tests. The feed buffer solutions of different pH were all stirred at 400 rpm and pressurized between 0.1–0.5 bar. The hydraulic permeability of the membrane was determined by the ratio of the volumetric filtrate flux (L m^{-2} h^{-1}) to the trans-membrane pressure.

Results and Discussion

The –SH thiol group is one of the most common functional groups in biomolecules and is highly versatile in biochemical reactions. Click chemistry with maleimide groups efficiently forms covalent bonds. Two molecules with thiol groups may attach/detach reversibly in an oxidizing/reducing environment (e.g. cysteine). Sulfur also interacts strongly with gold. Therefore we intended to generate SNIPS membranes with binding sites by making a BCP that contains sulfhydryl groups. Previous studies have shown that such sulfhydryl end-functionalization can be achieved when terminating anionic polymerization of cyclic sulfides with alcohols[16].

Block copolymer with sulfhydryl groups

In our work, a new type of triblock terpolymer, poly(styrene)-block-poly(4-vinylpyridine)-block-poly(propylene sulfide) (SVPS) was synthesized and a terminal sulfhydryl group introduced at the end of each polymer chain. Figure 5.1a illustrates the synthesis procedure with details described in the experimental section. When polymerization of the third PPS block was completed, the thiolate living centers were saturated with proton donors (methanol) to give one sulfhydryl group per chain. Peak d and e in the ^{1}H NMR spectrum of the polymer (Figure 5.1b) are characteristic peaks for poly(propylene sulfide).[18] The relative amount of PPS block is 4 % by weight. Such a short end block is desired as we are focusing on the terminal thiol groups. When SNIPS membranes are fabricated from PS-*b*-P4VP, the pore walls and surfaces are lined with P4VP.[1] The short length of the PPS block should minimize its influence on the SNIPS process, and thiol groups are expected on the membrane surface rather than being buried inside the membrane.

To demonstrate the presence of active thiol groups, a redox reaction was conducted. Two molecules with free thiol groups can be oxidized and linked together by forming a disulfide bond. If the molecules are identical the product has twice the molar mass of the original molecules, therefore referred to as “dimer" here. In turn, the dimer can be reduced to its parent molecules by reducing agents that specifically target disulfide bonds (e.g. dithiothreitol, DTT).[19] We therefore first oxidized SVPS in solution by air and then reduced the product with DTT. Molar masses for each step were monitored by GPC. The small shoulder at the dimer position of the GPC trace for the as-made polymer most likely stems from a small amount of oxidized polymer already present after preparation and storage. As GPC traces (Figure 5.1c) demonstrate, after oxidation a pronounced dimer peak appeared to the left of the parent polymer peak (red trace). After adding DTT, the dimer peak completely disappeared (blue trace). The fact that only a fraction of the

polymer peak shifted to the dimer peak during oxidation is expected and likely due to the macromolecular nature of the molecules; It is kinetically difficult for two terminal thiols on two polymers of over 60 kg/mol molar mass to find each other in dilute solutions. The lack of an oxidizing agent in solution and reliance on O_2 from air likely is another factor. These experimental results together support the successful incorporation of active sulfhydryl groups in the SVPS polymer chain.

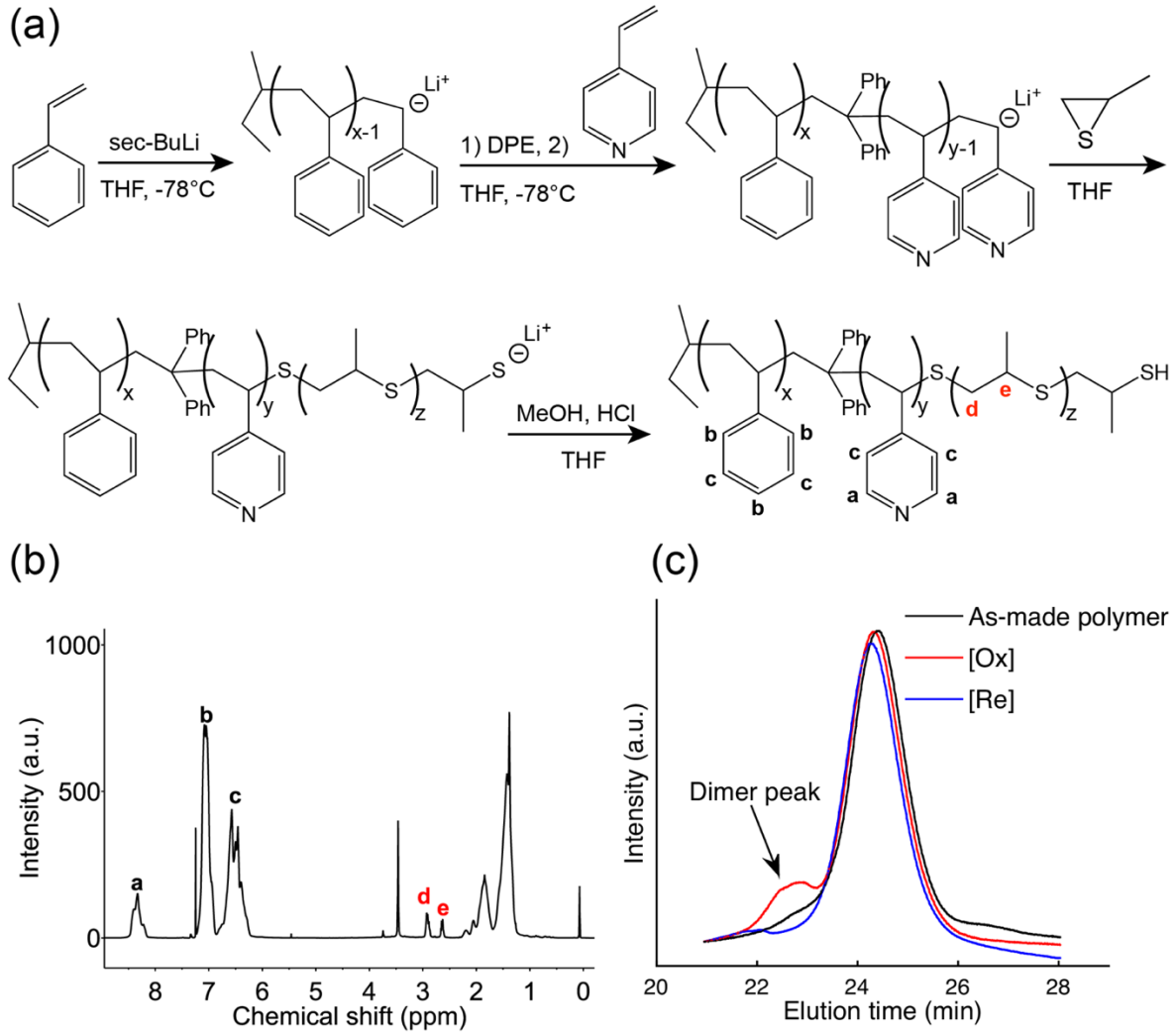

Figure 5.1 (a) Synthesis scheme and (b) ^{1}H NMR spectrum of triblock terpolymer poly(styrene-b-(4-vinyl)pyridine-b-propylene sulfide). (c) GPC trace in DMF of as-made polymer (black), polymer oxidized by air at 60 °C (red), and polymer reduced by DTT after oxidization (blue)

Membrane fabrication and characterization

The SNIPS process, as aforementioned, is a convenient and scalable method to fabricate asymmetric polymeric membranes with an isoporous ultrafiltration layer. However, for a new polymer the preparatory work typically requires screening over a large parameter space including appropriate solvent or solvent mixtures, solution concentration, evaporation time, etc. The conventional trial and error approach to optimize casting conditions can be accelerated using solution screening by small-angle X-ray scattering (SAXS).[2] To that end SVPS polymer solutions with different solvent systems and concentrations were tested. For an appropriate solvent system, solution SAXS shows a highly ordered micelle structure when concentrations are above a certain threshold value. Typically, concentrations of the membrane casting solution right below this threshold results in well-organized surface separation layers.[2] Two representative solution SAXS curves are shown for SVPS in Figure 5.2. The solvent system chosen was DOX/THF (1:1 by weight) and concentrations were 10 wt % and 13 wt % for the lower and upper curve, respectively. While for the 10 wt % solution assignment of a lattice was impossible as a result of the few and very broad peaks, for the 13 wt % solution the curve showed multiple peaks consistent with a body centered cubic (BCC) lattice of SVPS micelles.

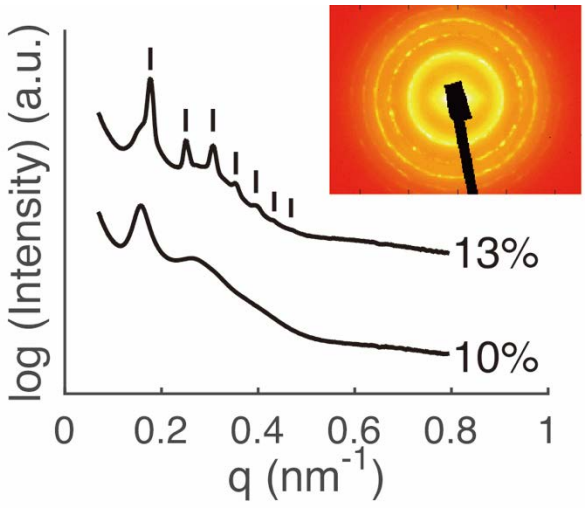

Figure 5.2 SAXS patterns of concentrated SVPS solutions. Peaks are indexed according to $(q/q^*)^2 = 1, 2, 3, 4, 5, 6,$ and 7, consistent with an ordered BCC lattice of BCP micelles.

Following the rational described above for the SNIPS process the solution concentration was reduced to 9%.

Indeed, for 45 s evaporation time SNIPS membranes with regularly patterned surfaces were obtained. SEM characterization of the top surface shows mesopores with narrowly dispersed pore sizes (~17 nm) well-organized into a 2D hexagonal lattice (Figure 5.3a). This was corroborated by FFT analysis (Figure 5.3d) of the image. The cross section of the membrane (Figure 5.3b) shows a sponge-like structure with a thickness around 20 μm. A zoomed-in image of the cross section (Figure 5.3e) and bottom surface images (Figure 5.3c,f) show a spaghetti-type substructure with macropores below the separation layer. Such an asymmetric isoporous structure not only favors high selectivity but also allows for high permeability. Both features are crucial factors in membrane performance.

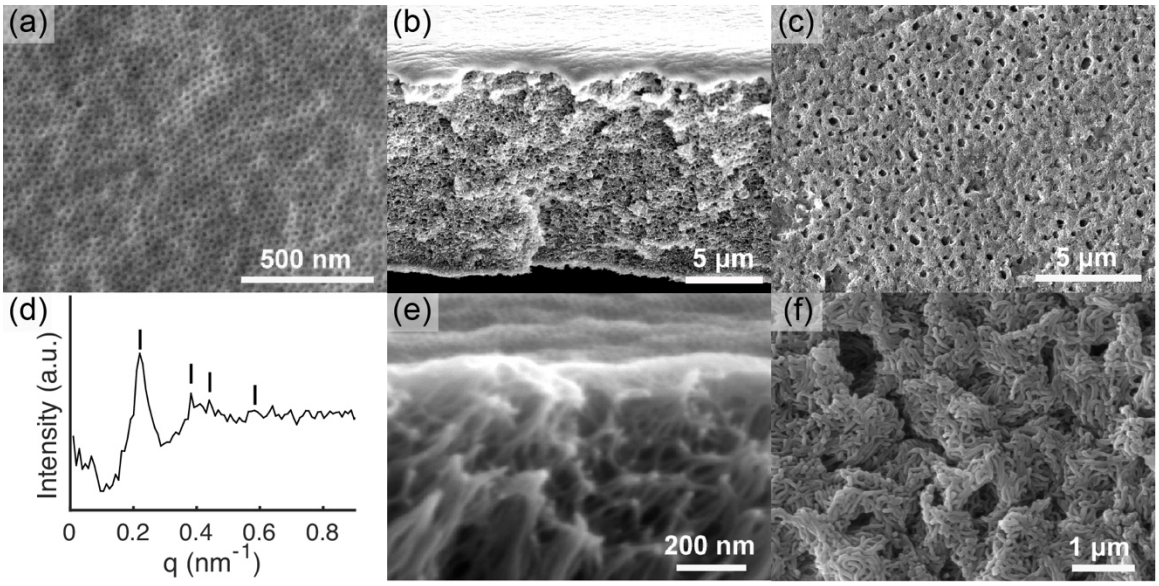

Figure 5.3 SEM characterization of (a) top surface, (b,e) cross section, and (c,f) bottom surface of a SVPS membrane. (d) FFT analysis of top surface SEM image. Peaks correspond to $(q/q^*)^2 = 1, 3, 4$, and 7, indicating expected peak positions for a 2D hexagonal lattice.

Stimuli responsive membrane behavior

pH response is a characteristic property of SNIPS membranes containing P4VP blocks in the pore walls. Such pH-responsive behavior is due to P4VP protonation/ deprotonation. Hydraulic permeability tests of SVPS membranes were conducted with buffer solutions of various pH. In Figure 5.4 the SVPS membrane maintains a relatively high permeability in the high pH regime, which decreases significantly as pH drops from 6 to 4. These results are consistent with mesopores of the ultrafiltration layer coated with P4VP brushes. From these results it is evident that the short PPS block does not undermine the desirable membrane structure formation and stimulus responsive behavior.

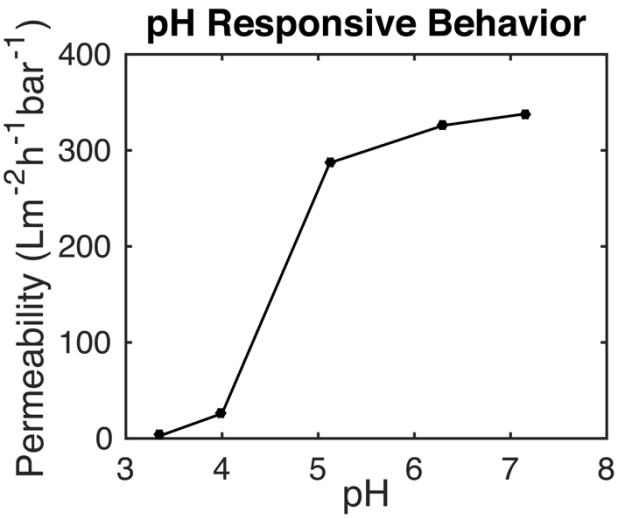

Figure 5.4 pH-responsive behavior of a SVPS membrane.

Quantification of accessible thiol groups

After membrane fabrication via the SNIPS process, an obvious question was if the functional groups are still accessible. Although sitting right on the P4VP block likely exposing the PPS block and thiol groups to the surface of mesopores, functional groups could still be more or less buried. To assess the accessibility of thiol groups, we designed an experiment performed on asymmetric SVPS membranes with Ellman's reagent, a commonly used chemical for detecting thiols in bio-systems. When free sulfhydryl groups react with Ellman's reagent, the solution turns yellow as a result of the reaction product absorbing light at a wavelength of 412 nm. Unlike the normal Ellman's reagent used in bio-systems, we employed a recipe adopted from literature[20] using a methanol/buffer

mixture rather than buffer solution only as the solvent. This modification helps restrain the self-decomposition of Ellman's reagent. We soaked the membranes in Ellman's reagent solution while gently stirring with a spinbar. The Ellman's reagent solution was colorless prior to membrane immersion. After soaking the thiol functionalized membranes, the solution gradually turned yellow with the color deepening over time. Aliquots were taken for optical absorbance measurements after 12 h. Clear absorption peaks were observed around 412 nm (Figure 5, red line). An experiment with a blank sample (no membrane) was conducted in the same way as a control and no peak at 412 nm was observed after 12h (Figure 5.5, black line). The result of the Ellman's reagent experiment is consistent with accessible thiol groups after membrane formation via SNIPS. We further quantified the amount of accessible thiol groups using the absorbance at 12h and an extinction coefficient of 13100 $M^{-1}cm^{-1}$ adopted from literature.[20] The total amount of thiol groups was estimated according to each membrane's weight and dimension. Results listed in Table 5.1 indicate that about 21 % of the total functional groups in the membrane are accessible. While this analysis suggests that accessibility is not 100%, likely due to effects like chain end folding back into the membrane surface layer, results reveal abundant covalent binding sites in the SVPS membranes highlighting the potential for covalent membrane modification post-fabrication.

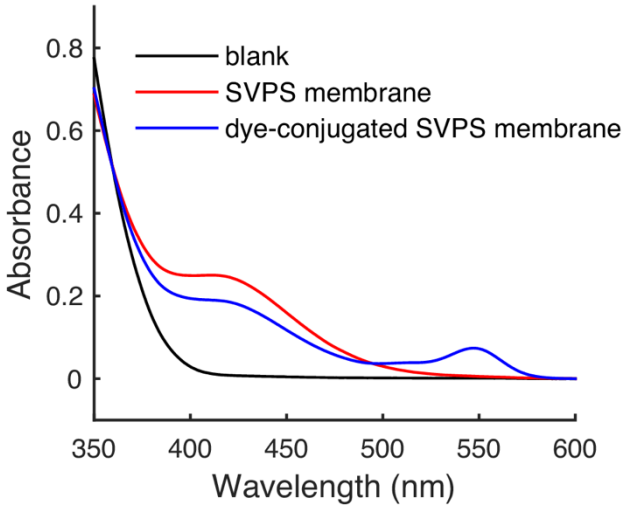

Figure 5.5 Ellman's reagent test results. SVPS membranes (red line) and dye-conjugated SVPS membranes (blue line) were soaked in Ellman's reagent solution and aliquots were taken for absorbance spectra at 12 h. An aliquot of blank sample (without membrane) was taken at 12 h as a reference. The peaks around 412 nm indicate the existence of active sulfhydryl groups in the membranes.

Table 5.1 Quantification of thiol groups in membrane

Total thiol groups / area (mol/cm^2) [a,c]	Accessible thiol groups / area (mol/cm^2) [b,c]	Accessible thiol groups percentage	Covalent bonds / area (mol/cm^2) [d]	Percentage of accessible thiol groups formed covalent bonds [d]
1.7×10^{-8}	3.6×10^{-9}	21 %	9.2×10^{-10}	26 %

[a] Total thiol groups amount are calculated according to membrane weight, polymer molar mass, and assumption that each polymer chain contains one thiol group

[b] Accessible thiol groups amount are calculated according to the 12 hours Ellman's reagent experiment and the extinction coefficient 13100 $M^{-1}cm^{-1}$

[c] Each membrane has an area of 5 cm^2 and an average weight of 0.0054 g

[d] Covalent bonds between membrane and TMR dye are calculated according to the 12 hours Ellman's reagent experiment of SVPS membrane and dye-conjugated SVPS membrane with the extinction coefficient 13100 $M^{-1}cm^{-1}$

Foreign molecule attachment

To acquire additional functionality, one of the commonly used methods is to mix foreign molecules with the membrane casting dough. However, such a route is not realistic for bio-receptors since BCP solutions are usually made from organic solvents that would easily denature proteins and enzymes. Alternative routes include a binding layer, which requires an extra formation step and may not be permanent. The simplest approach is to immerse the membrane in a solution containing the foreign molecule. In conventional membranes such methods rely on nonspecific and noncovalent binding of foreign molecules. In contrast, based on the experimental results reported so far SVPS membranes should have the ability to form specific covalent bonds with targeted molecules based on the accessible sulfhydryl groups on the membrane pore surface.

To prove this assumption, we employed a maleimide-functionalized dye as a targeted model molecule for attachment. To that end thiol-functionalized SVPS membranes and unfunctionalized SV membranes as a control were fabricated via the SNIPS process and compared. Both membranes were soaked in a PBS buffered maleimide-functionalized tetramethyl rhodamine-5 (TMR) dye containing solution for 1 day. After removal from the dye solution, both membranes showed a strong pink color (Figure 5.6). Although both membranes showed dye retention after soaking, the mechanism and strength of binding between membrane and target molecule was very different. To demonstrate this difference

we soaked both pink membranes in dimethyl sulfoxide (DMSO). DMSO is a good solvent for TMR dye. After the DMSO wash, thiol-functionalized SVPS membrane still retained its pink color while the pink shade of the control SV membrane disappeared almost completely (Figure 5.6). SEM characterizations in Figure S5.4 confirmed that both membranes remained intact after DMSO wash. Although SV has higher molar mass than SVPS, the two polymers have very similar block fractions and formed identical membrane structures with mesoporous skin layer, sponge-like cross-section and spaghetti-type bottom surface (Figure S5.3). SV has a longer hydrophilic P4VP block, which should favor TMR association, and SV membranes were almost twice as thick as SVPS membranes, It is therefore unlikely that the ability of SVPS membranes to retain more dye than SV membranes is due to noncovalent interactions or trapping of dye molecules in the membrane structure. Based on these considerations, SV membranes served as a strong control group to confirm that dye retention in SVPS membranes is due to covalent binding. All results suggest that the sulfhydryl groups of the SVPS membrane and the maleimide groups of the dye formed irreversible covalent bonds via click chemistry while the SV membrane only nonspecifically adsorbed dye molecules, which subsequently could be washed out again.

Figure 5.6 Functionalized-dye conjugation assessment. SVPS and SV (control group) membranes were soaked in a maleimide-functionalized TMR dye solution. Both groups had a pink appearance after soaking. With a rinse in DMSO, the pink shade remained in the SVPS membrane while it faded in the SV membrane, consistent with covalent bonding between SVPS membrane and maleimide-functionalized dye.

The C-S bonds formed between the membrane terminal –SH groups and dye molecules were hard to quantify by spectroscopic techniques such as e.g. Fourier transform infrared spectroscopy (FTIR) or NMR due to the already existing C-S bonds in the PPS block (e.g. see peaks d and e in the NMR spectrum in Figure 5.1c). The SVPS studied here has an average of 34 propylene sulfide units per macromolecule with each monomer carrying C-S bonds making quantification of the terminal C-S bond formation impossible. Alternatively, in order to further demonstrate and quantify the formation of covalent bonds, Ellman's reagent experiments were conducted on the dye-conjugated SVPS membranes (after DMSO wash) using the same procedure described before. The absorption peak height at 412 nm (Figure 5.5, blue line), resulting from unconjugated sulfhydryl groups reacting

with Ellman's reagents, decreased compared to the peak height of neat SVPS membranes (Figure 5.5, red line), indicating less free sulfhydryl groups in the dye-conjugated SVPS membranes due to covalent binding with TMR dye (The additional peak at 542 nm resulted from a small quantity of non-specifically adsorbed dye molecules that were not removed by the DMSO rinse and dissolved in the Ellman's reagent solution during membranes soaking). An estimate of the amount of covalent bonds formed between SVPS membrane and TMR dye from these experiments is listed in Table 5.1. According to this estimate 26 % of the accessible thiol groups in the membranes formed covalent bonds via sulfhydryl-maleimide click chemistry. Results are again consistent with covalent binding in the functionalized SVPS membrane. SVPS membrane thiol groups are active in buffer solution, which is a mild and compatible environment for proteins and enzymes. This opens pathways for future experiments in which such biomolecules can be covalently linked to SNIPS membranes via simple immersion in solutions containing such target molecule(s), a process that like the SNIPS process is easily scalable e.g. for industrial use.

Conclusions

We present a new triblock terpolymer, SVPS, which forms pH responsive asymmetric ultrafiltration membranes via SNIPS containing covalent binding sites. These covalent binding sites, sulfhydryl functional groups, are introduced via a short third PPS block as confirmed by ^{1}H NMR as well as analytic redox reactions. After membrane formation, at least a fraction of the thiol groups remain accessible and active.

Quantification experiments prove that functional groups are exposed and accessible on the pore walls and membrane surfaces. By conducting a reaction with maleimide-functionalized dye, we show that the binding sites are able to attach target molecules via thiol-ene click chemistry. Sulfhydryl groups are active in various environments such as buffer solutions and organic solvents. This opens a pathway to numerous post-modification reactions with target molecules like proteins and enzymes covalently attached to SNIPS membranes via simple immersion in solutions containing the targets. Like the SNIPS process itself these post-modification reactions are therefore scalable for industrial use. The concepts described here are not limited to sulfhydryl groups. Other functional groups including amines or carboxylic groups could be covalently attached to the end group/block of BCPs via anionic polymerization that are subsequently used in the SNIPS process such that the functional groups end up on the pore surface of the top separation layer as well as the substructure. As more types of pore-block end-functionalized membranes emerge, the choice of incorporated receptors/target molecules is expected to expand rapidly. This study therefore lays the foundation for the rapid and simple production of bio-responsive membranes and numerous applications for such multi-functional asymmetric block copolymer membranes.

Acknowledgment

Q.Z. acknowledges the FLIR Systems, Inc. and the Defense Threat Reduction Agency (DTRA) for the financial support (through Grant No. HDTRA1-13-C-0003.). P.A.B. was

supported by the NSF Graduate Research Fellowship Program (DGE-1144153). This work made use of the Cornell Center for Materials Research Shared Facilities which are supported through the NSF MRSEC program (DMR-1120296), and the Cornell High Energy Synchrotron Source (CHESS) which is supported by the National Science Foundation and the National Institutes of Health/National Institute of General Medical Sciences under NSF award DMR-1332208. Q.Z acknowledges S. W. Robbins and R. M. Dorin (both at TeraPore Technologies, Inc.) for GPC measurements, and J. Poole (FLIR Systems, Inc.), K. Barteau (Wiesner group, Cornell University) for helpful discussions.

REFERENCES

1. Peinemann, K. V.; Abetz, V.; Simon, P. F. Asymmetric superstructure formed in a block copolymer via phase separation. *Nat. Mater.* **2007**, 6, 992-996.

2. Dorin, R.M.; Marques, D.S.; Sai, H.; Vainio, U.; Phillip, W.A.; Peinemann, K.V.; Nunes, S.P.; Wiesner, U. Solution small-angle X-ray scattering as a screening and predictive tool in the fabrication of asymmetric block copolymer membranes. *ACS Macro Lett.* **2012,** 1, 614-617.

3. Jung, A.; Rangou, S.; Abetz, C.; Filiz, V.; Abetz, V. Structure Formation of Integral Asymmetric Composite Membranes of Polystyrene-block-Poly (2-vinylpyridine) on a Nonwoven. *Macromol. Mater. Eng.* **2012,** *297*, 790-798.

4. Hahn, J.; Filiz, V.; Rangou, S.; Clodt, J.; Jung, A.; Buhr, K.; Abetz, C.; Abetz, V. Structure formation of integral-asymmetric membranes of polystyrene-block-Poly (ethylene oxide). *J. Polym. Sci., Part B: Polym. Phys.* **2013,** 51, 281-290.

5. Jung, A.; Filiz, V.; Rangou, S.; Buhr, K.; Merten, P.; Hahn, J.; Clodt, J.; Abetz, C.; Abetz, V. Formation of integral asymmetric membranes of AB diblock and ABC triblock copolymers by phase inversion. *Macromol. Rapid Commun.* **2013,** 34, 610-615.

6. Hahn, J.; Clodt, J.I.; Filiz, V.; Abetz, V. Protein separation performance of self-assembled block copolymer membranes. *RSC Adv.* **2014,** 4, 10252-10260.

7. Qiu, X.; Yu, H.; Karunakaran, M.; Pradeep, N.; Nunes, S. P.; Peinemann, K. V. Selective separation of similarly sized proteins with tunable nanoporous block copolymer membranes. *ACS Nano* **2012,** 7, 768-776.

8. Zhang, Y.; Sargent, J. L.; Boudouris, B. W.; Phillip, W. A. Nanoporous membranes generated from self-assembled block polymer precursors: Quo Vadis?. *J. Appl. Polym. Sci.* **2015**, *132*, 41683 (1-17).

9. Clodt, J.I.; Filiz, V.; Rangou, S.; Buhr, K.; Abetz, C.; Höche, D.; Hahn, J.; Jung, A.; Abetz, V. Double Stimuli-Responsive Isoporous Membranes via Post-Modification of pH-Sensitive Self-Assembled Diblock Copolymer Membranes. *Adv. Funct. Mater.* **2013,** 23, 731-738.

10. Hu, L.; Gao, S.; Ding, X.; Wang, D.; Jiang, J.; Jin, J.; Jiang, L. Photothermo-Responsive Single-Walled Carbon Nanotube-Based Ultrathin Membranes for On/Off Switchable Separation of Oil-in-Water Nanoemulsions. *ACS Nano* **2015,** 9, 4835–4842.

11. Keskin, D.; Clodt, J. I.; Hahn, J.; Abetz, V.; Filiz, V. Postmodification of PS-b-P4VP Diblock Copolymer Membranes by ARGET ATRP. *Langmuir* **2014,** 30, 8907-8914.

12. Gu, Y.; Dorin, R. M.; Wiesner, U. Asymmetric Organic–Inorganic Hybrid Membrane Formation via Block Copolymer–Nanoparticle Co-Assembly. *Nano Lett.* ***2013,*** 13, 5323-5328.

13. Mulvenna, R. A.; Weidman, J. L.; Jing, B.; Pople, J. A.; Zhu, Y.; Boudouris, B. W.; Phillip, W. A. Tunable nanoporous membranes with chemically-tailored pore walls from triblock polymer templates. *J. Membr. Sci.* **2014,** 470, 246-256.

14. Phillip, W. A.; Mika Dorin, R.; Werner, J.; Hoek, E. M.; Wiesner, U.; Elimelech, M. Tuning structure and properties of graded triblock terpolymer-based mesoporous and hybrid films. *Nano Lett.* **2011,** 11, 2892-2900

15. Schacher, F.; Ulbricht, M.; Müller, A. H. Self-Supporting, Double Stimuli-Responsive Porous Membranes From Polystyrene-block-poly (N, N-dimethylaminoethyl methacrylate) Diblock Copolymers. *Adv. Funct. Mater.* **2009,** 19, 1040-1045.

16. Stouffer, J. M.; McCarthy, T. J. Polymer monolayers prepared by the spontaneous adsorption of sulfur-functionalized polystyrene on gold surfaces. *Macromolecules* **1988,** 21, 1204-1208.

17. Napoli, A.; Valentini, M.; Tirelli, N.; Müller, M.; Hubbell, J. A. Oxidation-responsive polymeric vesicles. *Nat. Mater.* **2004,** 3, 183-189.

18. Napoli, A.; Tirelli, N.; Kilcher, G.; Hubbell, A. New synthetic methodologies for amphiphilic multiblock copolymers of ethylene glycol and propylene sulfide. *Macromolecules* **2001,** 34, 8913-8917.

19. Tsarevsky, N. V.; Matyjaszewski, K. Reversible redox cleavage/coupling of polystyrene with disulfide or thiol groups prepared by atom transfer radical polymerization. *Macromolecules* **2002,** 35, 9009-9014.

20. Sedlak, J.; Lindsay, R. H. Estimation of total, protein-bound, and nonprotein sulfhydryl groups in tissue with Ellman's reagent. *Anal. Biochem.* **1968,** 25, 192-205.

APPENDIX D

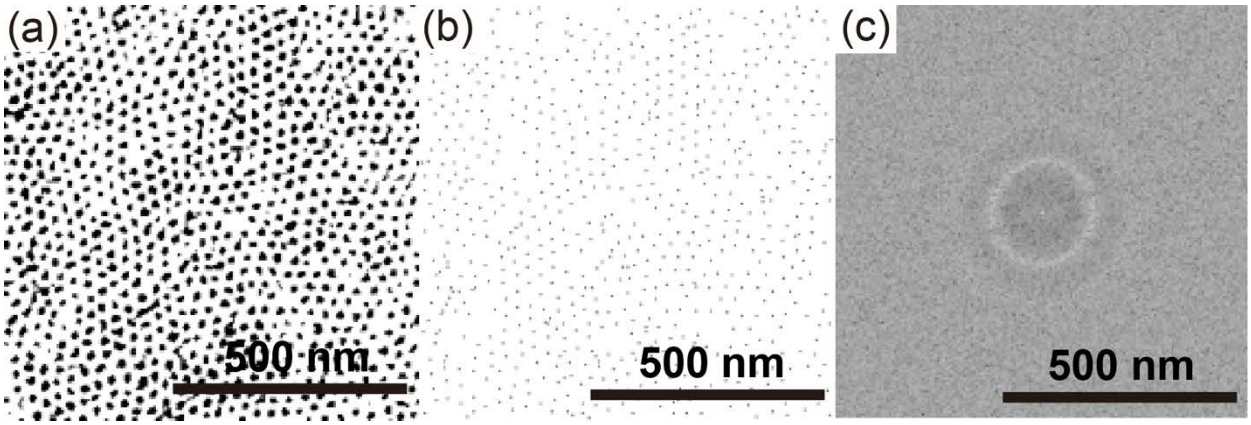

Figure S5.1 Image processing details for FFT radical profile with ImageJ. (a) Set threshold between 0 – 22.08 % for Figure 3a. (b) Find edges and find maxima of Figure S1(a). (c) Fast Fourier Transform of Figure S1(b). Radical profile of FFT image is in Figure 3(d).

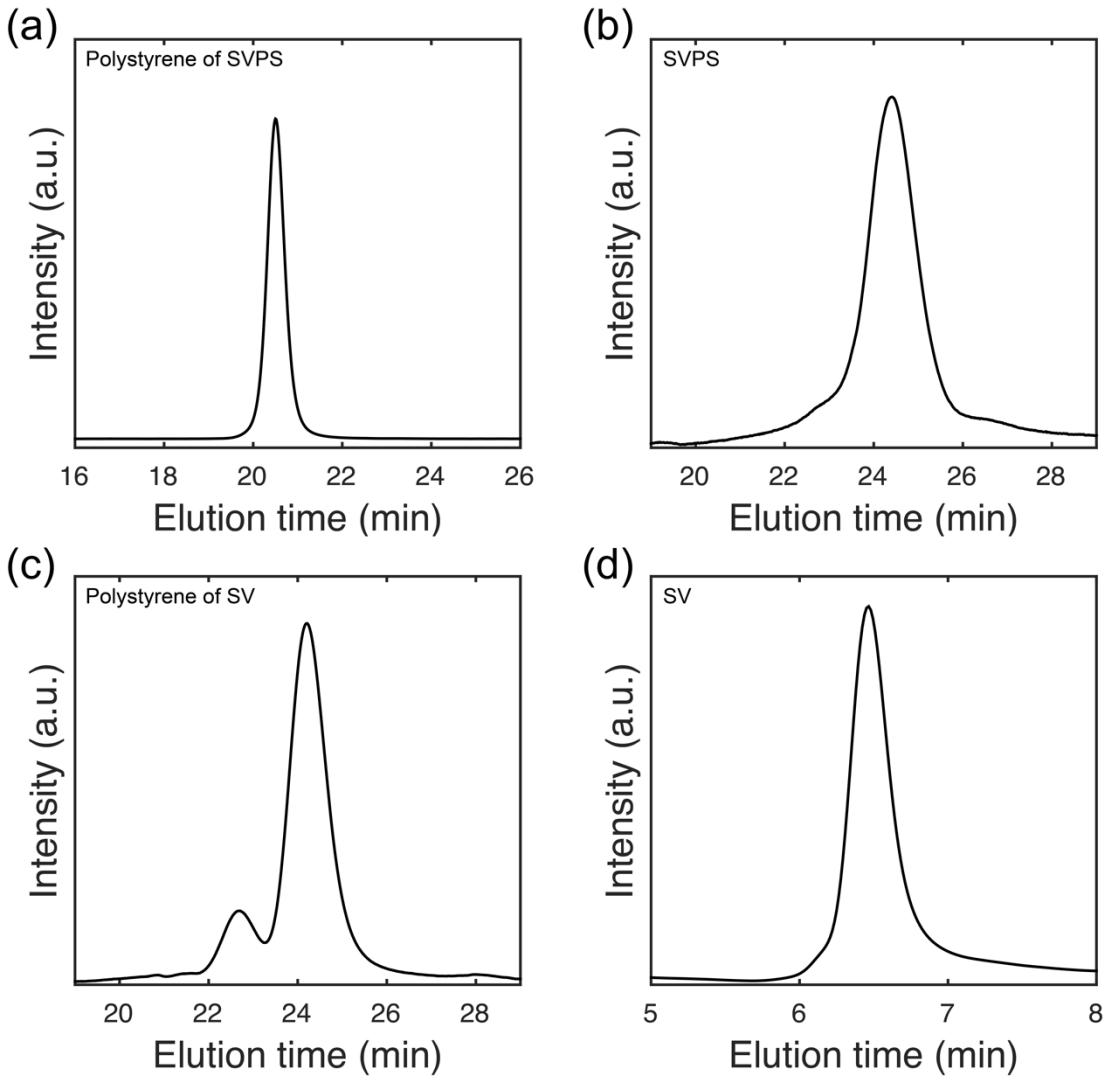

Figure S5.2 GPC elution curves of SVPS and SV and their polymer intermediates. (a) Polystyrene of SVPS; The GPC measurement was performed in THF on a Waters ambient-temperature GPC system equipped with a Waters 2410 differential refractive index (RI) detector. (b) SVPS; The GPC measurement was performed in DMF as described in the experimental section. (c) Polystyrene of SV; The GPC measurement was performed in DMF as described in the experimental section. The smaller peak on the left at twice the molar mass of the main peak resulted from dimerization of polystyrene. As the GPC curve

of the final SV in (d) showed a monomodal distribution, the dimer peak probably resulted from aliquot sampling for GPC via introduction of oxygen and did not represent the mass distribution of the living polystyrene used for further polymerization with poly(4-vinylpyridine). (d) SV. The GPC measurement was performed in THF on an Agilent 1050 instrument equipped with an Agilent PLgel 5 μm Mixed-C column and an Agilent 1100 differential refractive index (RI) detector.

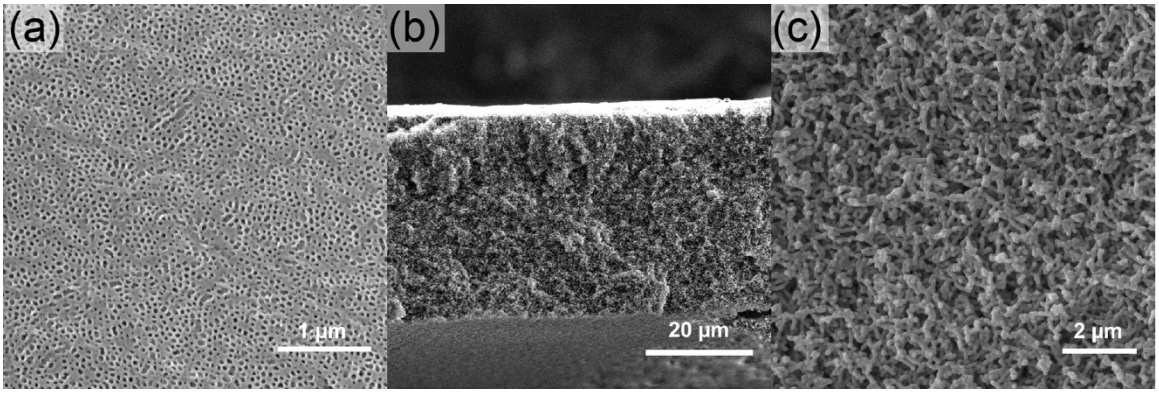

Figure S5.3 SEM characterization of (a) top surface, (b) cross section, and (c) bottom surface of a SV membrane

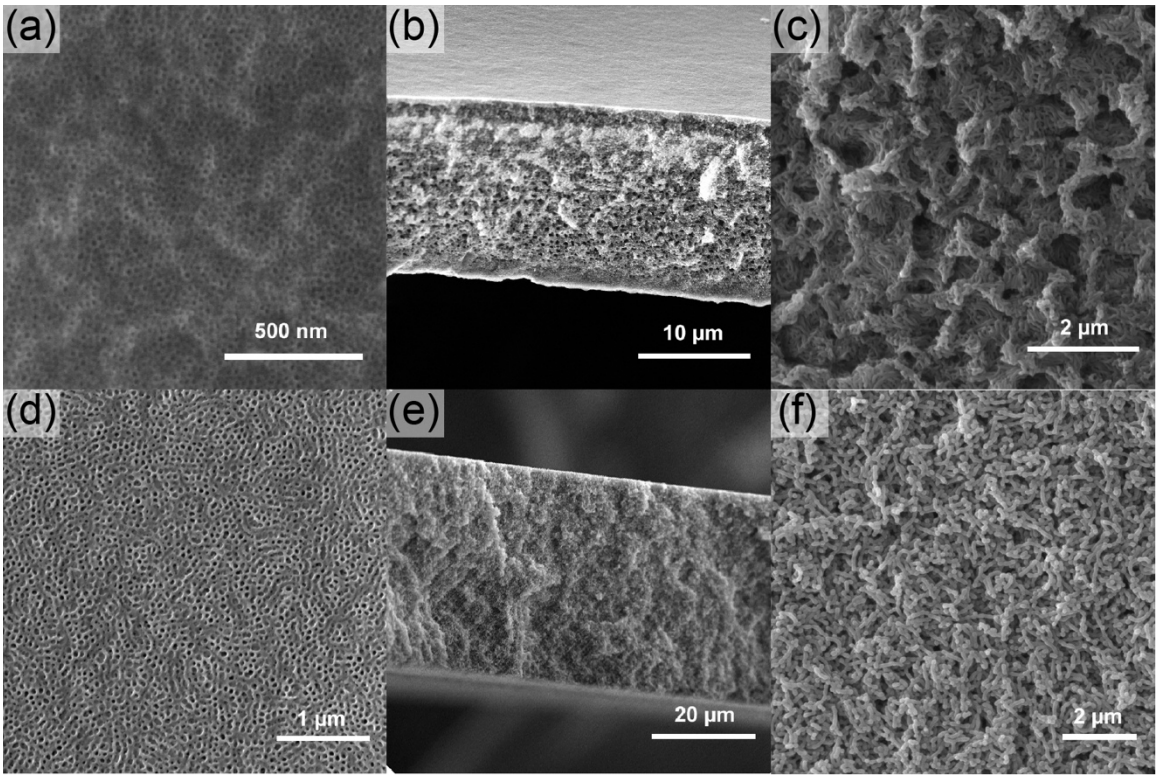

Figure S5.4 SEM characterization of (a,d) top surfaces, (b,e) cross sections, and (c,f) bottom surfaces of SVPS (a-c) and SV (d-f) membranes washed with DMSO.

CHAPTER 6

CONCLUSION

In this dissertation, functional nanomaterials were explored with three dimensional (3D) continuous structures derived from block copolymer (BCP) self-assembly and leading to gyroidal mesoporous resin/carbon thin films (Chapter 2), graded isoporous ultrafiltration (UF) membranes with controlled substructure and top separation layers (Chapter 3, 4), as well as UF membranes with functional groups along the pore surface as covalent binding sites for the generation of smart materials systems (Chapter 5).

In Chapter 2, synthetic pathways towards gyroidal mesoporous resin/carbon thin films employing solvent vapor annealing were investigated with the help of *in situ* grazing incidence small angle x-ray scattering (GISAXS). Films exhibited structural uniformity on the centimeter scale, while their formation approaches were compatible with larger scale synthesis. Characterization in terms of thermal stability and surface wetting properties in conjunction with a transfer technique to alternative substrates suggested these thin films for use as versatile and robust 3D templates.

In Chapter 3 and 4, triblock terpolymer self-assembly and non-solvent induced phase separation (SNIPS) derived asymmetric ultrafiltration membranes were studied. Several key parameters were systematically explored to tune membrane top separation layer structure as well as substructure. The mechanisms responsible for sublayer structure evolution were also described. Membranes with different structures were characterized by their permeability and challenged by small molar mass solutes in order to obtain structure-

property correlations. Model solute diffusivity results as a function of surface structural changes were rationalized by theoretical calculations. These studies provided guidelines to achieve optimum performance by influencing BCP SNIPS membrane structure using different sets of casting conditions.

In Chapter 5, a new type of triblock terpolymer with end sulfhydryl functional groups was synthesized and fabricated into membranes using SNIPS process. After membrane fabrication the thiol groups remained accessible and active. The membranes exhibited pH responsiveness due to a P4VP block, which can potentially function as a chemical gate. The thiol groups worked as covalent binding sites and were easily accessible by simply soaking the membrane in a target molecules solution. This membrane may have a number of applications in bio-sensing and as a multifunctional responsive smart system.

With the framework laid out by this dissertation, several future directions are worth pursuing. With respect to the gyroidal mesoporous carbon structures, an obvious next step is to use these thin films as templates to explore a wider range of materials with gyroidal mesoscale structure. Another direction to move into is perfecting the gyroid structure in terms of its degree of uni-axial shrinkage and crystallinity. The gyroidal carbon network thin films reported here exhibit a shrinkage of 70-80% along the film normal, which disrupts their symmetry and influences their properties. Solvent vapor annealing and pyrolysis processes ought to be further studied to decrease this level of shrinkage. In addition, while the gyroidal templates were textured relative to the substrate, the thin films still have polycrystalline structures. Since one of the interesting applications for these

structures are photonic crystal/metamaterial devices, large grain sizes, and ideally single crystal gyroidal structures are desired to gain precise control of their optoelectronic properties.[1] Some approaches such as chemo- or grapho-epitaxy, *i.e.* directed self-assembly, are worth looking into. In addition to the single crystallinity at the mesoscale, atomic scale single crystals within such templating films are also highly desirable. A laser annealing approach to achieve such atomic single crystal structures within BCP thin films has been reported,[2] but these films lacked long-range mesoscale order. Achieving materials with single crystal structures at both atomic and mesoscopic length scales would open up exciting new fundamental research directions as well as promising technological applications.

As to the SNIPS derived asymmetric UF membranes, different types of block copolymer derived systems have now been studied in detail, leading to respectable understanding of the processing-membrane structure correlations. But in order to effectively use knowledge of membrane structure to predict macroscopic performance, more precise models need to be developed that capture details of the complex asymmetric and hierarchical structure of SNIPS membranes, instead of e.g. commonly used and over-simplified cylindrical pore models. Only when such models are available, that fully take into account the hierarchical structure formation at all length scales, will the field be able to tale full advantage of the molecular engineering approach that for the first time these BCP based membranes provide access to.

Finally, regarding multi-functionality of SNIPS membranes, Chapter 5 has provided a promising platform – with reactive groups localized on the membrane pore surface directly accessible via the membrane formation process, i.e. without necessary post-fabrication steps. A facile dipping step of such membranes into a bath with desired functional molecules will accomplish membrane post-modifications that will help to further diversify membrane functionality. To that end a separate study by Li *et al.*[3] recently described a facile "mix and match" method in which via mixing of two chemically distinct block copolymers into the dope used for SNIPS membrane formation distinct chemistries can be introduced onto the membrane pore surface, further opening doors for scalable fabrication of multi-functional SNIPS membranes. With such a convenient toolbox, the design guidelines for the generation of a large variety of well-defined multifunctional smart membrane materials with hitherto unknown property profiles are now available promising substantial technological advances in this field. For instance, the work of this thesis provides clear design guidelines for membrane systems with chemical gating and active linkers for entirely novel applications.[4] Furthermore, the vision for applications should not be limited to the membrane field, but should include areas as diverse as catalysis and drug delivery which all may benefit from multi-functional porous materials that are amenable to large scale fabrication and facile surface modifications based on specific needs.

REFERENCES

1. Braun, P. V. Materials Chemistry in 3D Templates for Functional Photonics. Chem. Mater. 26, 277–286 (2014).

2. Arora, H. et al. Block Copolymer Self-Assembly–Directed Single-Crystal Homo- and Heteroepitaxial Nanostructures. Science 330, 214–219 (2010).

3. Li, Y. M., Srinivasan, D., Vaidya, P., Gu, Y. & Wiesner, U. Asymmetric Membranes from Two Chemically Distinct Triblock Terpolymers Blended during Standard Membrane Fabrication. Macromol. Rapid Commun. 37, 1689–1693 (2016).

4. Poole, J. L. et al. Biocatalytic Stimuli-Responsive Asymmetric Triblock Terpolymer Membranes for Localized Permeability Gating. Macromol. Rapid Commun. 38 (2017).